Mechanisms of Supersonic Drag Reduction using Repetitive Energy Depositions

A dissertation submitted in partial fulfillment for the requirement for the degree of doctor of engineering

Akira Iwakawa

Department of Aerospace Engineering

Nagoya University

December 2015

Dissertation Committee

Akihiro Sasoh
Professor

Katsuya Ishii
Professor

Koji Nagata
Professor

Takeharu Sakai
Associate Professor

Koichi Mori
Associate Professor

Acknowledgments

First, I would like to express my heartfelt gratitude to my supervisor, Professor Akihiro Sasoh for guidance and encouragement through my PhD work over the years. His encouragement helped me to broaden my scope of interest and to complete the present study. I would also like to show my appreciation to Associate Professor Takeharu Sakai for drawing on his insights into and experience with the numerical approach to offer his technical advice and suggestions. I would also thank Professor Hiromitsu Kawazoe for assisting to complete theoretical analysis of newly developed balance system. I also sincerely thank the committee members of this manuscript, Professor Katsuya Ishii, Professor Koji Nagata, and Associate Professor Koichi Mori for taking valuable time out of their busy schedules to provide advice and suggestions for this study.

I greatly thank all members of Shock Wave and Space Propulsion Laboratory and alumni of Ionized Gas Dynamics Laboratory for general laboratory assistance. In addition, special thanks to Mr. N. Hasegawa, Mr. T. Osuka, Mr. R. Majima, Mr. T. Tamba, Mr. T. Shoda and Mr. H. S. Pham for their cooperation and assistance.

I also thank my friends, my classmates in the laboratory I was attached to, and Dr. R. Tuskizaki, Dr. A. Matsuda and Dr. T. Tsuda for their encouragement.

Finally, I would like to express my gratitude to my family for their understanding, support and encouragement.

Akira IWAKAWA

Contents

Figure Contents

Table Contents

Nomenclature

(r, z)	two-dimensional axisymmetric coordinate
$[K]$	matrix of the calibration coefficients of ring force balance
A	cross-sectional area of ring part of balance
C	constant
d_0	diameter of the model of cylinder part
d_c	bottom diameter of the conical spike
D	drag force
D_0	drag force of flat-head cylinder model without energy deposition
e	effect of the strain gauge length
E	deposited energy per pulse (except section 2.2)
E	Young's modulus (in section 2.2)
f	laser pulse repetition frequency
F_s	gauge factor of the strain gauge
h	distance between the center and outside surfaces of the ring portion
I	moment of inertia of the area
l	length of the conical spike
L	lift force
l_g, l_s	length of the strain gauge, support arm
M	moment
N	statically indeterminate axial force
N_{vortex}	number of vortex rings in Eq. (3.1)
p	pressure
p_0	pressure at stagnation point without energy deposition
p_{st}	pressure at stagnation point
P	statically indeterminate shear force
P_a	input power
Q	spatial distribution of deposited energy source
q_0	total input power per unit mass
R	outer surface radius of the ring force balance

r_0 radius of deposited energy source

s distance of energy deposition area from model head

s_{model} depth of the model head of calculation

t elapsed time

t_r thickness of the ring force balance

u_z z-direction component of flow speed

$\boldsymbol{u}$ flow vector

U strain energy

u_∞ upstream flow speed

u_r r-direction component of flow speed

V_0 volume of deposited energy source

w width

z_0 center position of deposited energy source

α temperature coefficient of resistance

β_m linear thermal expansion coefficient of the balance

β_s linear thermal expansion coefficient of the strain gauge

δ shock stand-off distance

δ_0 shock stand-off distance of flat-head cylinder model

ΔD drag reduction

ΔT temperature increment on the force balance

ε_r apparent strain caused by the resistance change of the strain gauge

ε_t apparent strain caused by the thermal expansion difference

ε_T apparent strain caused by the temperature change, including thermal expansion

η efficiency of energy deposition

η_a effectively deposited energy ratio

θ angle

θ_c half apex angle of conical spike

θ_g position of the strain gauge

λ step function

σ standard deviation

τ deposited energy pulse duration

τ_{vortex} residence time of vortex ring in shock layer

Chapter

1

Introduction

1.1 Improvement of Supersonic Aerodynamics Performance

There are two major issues to realize a commercial supersonic airplane: sonic boom and relative lower lift-to-drag ratio (L/D) compared with subsonic airplane. The sonic boom noise level during supersonic cruise of the Concorde, which is the commercial supersonic airplane, was 105 PLdB.[1] This noise level exceeds the target noise level of 70 - 76 PLdB for next generation supersonic airplane in 2030.[2] The L/D of the Concorde during supersonic cruise was 7.14[1] whereas the subsonic Boeing 747 has an L/D of 17.[3] These issues are related to shock waves occurring when the airplane flies at supersonic speeds. For solving these issues, evaluations of sonic boom noise level and aerodynamics performance are conducted using CFD techniques. Conceptual design of recent supersonic airplane for low-boom achieves sonic boom level of 70 PLdB, however, the lift-to-drag ratio of 7 - 8 is not improved.[4–6]

The cause of low L/D as compared with subsonic airplanes is drag increment due to shock waves during supersonic flight. In general, the drag of the airplane is classified into friction

drag and pressure drag force. Friction drag is determined by the state of the boundary layer, it does not vary greatly between subsonic and supersonic flight. On the other hand, pressure drag rapidly increases around a Mach number of 1.0, which shock waves begin to form. This drag increment is called as wave drag. In addition, wave drag can be classified into two component. One is wave drag due to volume, and another one is wave drag due to lift. Friction drag force is dominant during subsonic flight, but the ratio of the wave drag due to volume increases during supersonic flight, and this ratio is about 30 to 40% at Mach-2.0 flight of the Concorde.[7]

High wave drag caused by shock waves is the cause of the low L/D of supersonic airplane, and to overcome low L/D is the issue to realize a next generation commercial supersonic airplane. Some methods for reducing shock wave are summarized in Ref. 8. These methods are defined by the structural methods, such as modification of the body shape or attaching some devices, and non-structural methods, such as controlling flow. Attaching a physical spike[9] which is one of the structural methods may lead to wave drag reduction, yet the undesirable effect such as the system complexity, the heat transfer increasing and/or the shock wave and boundary layer interaction.[10,11] Non-structural methods such as upstream inert gas jet injection or upstream focused energy deposition are also effective for drag reduction. Actually, Shang et al. achieved 40% drag reduction on a hemisphere head model by experiment using counter jet flow injection approach in hypersonic flow[12,13]. Jet injection to nose region approach can provide the similar effect of the physical spike without system complexity, but this approach involves the production of injection thrust in the drag direction.

Energy deposition scheme of localized energy addition upstream of a supersonic-flying-body has promising potential to improve aerodynamic performance without any mechanical actions. The localized energy addition upstream can be achieved using electrodes,

microwaves or lasers. These approaches are described in Section 1.2, and the active and localized flow control can be achieved using energy deposition approaches.

1.2 Energy Deposition Method

Investigations of energy deposition approaches have been a focus of many experimental[14–22] and computational studies[23–34]. In these experimental studies, electrode[14–17], microwave[18], single pulse lasers[19] and repetitive pulses lasers[20–22] are used as energy sources. The wave drag reduction mechanisms with energy deposition were investigated by Knight[35] and Adelgre.[19] Then, the efficiency of steady energy deposition[14–18] was characterized in Ref. 35. There are two functions of the performance evaluation for the energy deposition approach. One is the reduced drag $\Delta D = D\text{-}D_0$ and another one is the efficiency of energy deposition η as shown in following Eq. (1.1) defined by Knight.[35]

$$\eta = \frac{u_\infty \times (-\Delta D)}{P_a} \tag{1.1}$$

For engineering useful of energy deposition, a condition needs to be satisfied, in which $\Delta D < 0$ and high $\eta > 1$ simultaneously.

One of the investigations of steady energy deposition, Exton et al.[18] supplied energy via microwave in supersonic flow at Mach number of 6.0 and demonstrated interaction of the bow-shock and thin plasmas. Steady energy deposition needs large input power, then it leads to small η value. Therefore, steady energy deposition cannot achieve effectively aerodynamics improvement.

Pulsed energy deposition[26–34] which is one of the unsteady energy deposition approaches can reduce input power as compared to steady energy deposition. Drag reduction mechanism of energy deposition is described in Section 1.3 in detail, and dominant effect of its approach

is upstream heating. Hence, input power of steady energy deposition directly affects to the drag reduction performance. On the other hand, pulsed energy deposition does not only have upstream heating, but also has the effect of vortex generation by interacting with shock waves. This vortex generation enhances the drag reduction performance. Then this approach has a potential to achieve with both of large drag decrement and high η value. For understanding mechanisms of pulsed energy deposition, single pulsed energy deposition[29,30] have been studied but repetitive pulsed energy deposition is neccesary for practical use. Tret'yakov et al.[20] and Kim et al.[21] investigated repetitive energy deposition via experiments. Tret'yakov et al.[20] achieved $-\Delta D/D_0 = 45\%$ drag reduction using CO_2 laser pulses with repetition frequency of 100 kHz in supersonic argon flow with a Mach of 2.0. However, the efficient energy deposition was not achieved due to $\eta < 1$. Kim et al.[21] obtained $-\Delta D/D_0 = 21\%$ supersonic drag decrement and $\eta = 10$ over a flat-head body using repetitive Nd: YVO_4 laser pulses. From these experimental results, the drag reduction performance of repetitive pulsed energy depositions is improved as repetition frequency increases. For understanding mechanism of repetitive pulsed energy deposition, simulations of this approach were performed by Georgievskii and Levin[31], Zudov et al.[32] and Sakai.[33] The frequency dependence of the drag reduction performance of these simulations agrees with experimental one. However, these simulations are mainly focused on quasi-steady state, which are drag reduction performance or flow structure, and the drag reduction mechanisms using repetitive pulsed energy deposition are not well understood.

1.3 Model of Drag Reduction using Energy Deposition

The drag reduction using energy deposition can be described by thermodynamics phenomena: the upstream flow is heated with isochoric process by energy deposition; the

temperature of the heated region decreases to the initial pressure by adiabatic expansion. As results of these heating and expansion, the momentum of the upstream flow is decreased. This model of steady energy deposition was presented by Sasoh.[36] Repetitive energy deposition is also described in the same way. However, pulsed energy deposition can achieve a larger drag reduction than the value predicted by this steady momentum decrement model. A reasonable explanation for this larger effect of the unsteady energy deposition is related to the vortex ring behavior[34,37] by the baroclinic effect.[38,39] Figure 1.1 shows the mechanism of baroclinic vortex ring generation: (a) pulsed energy is suppled in a certain area upstream of a shock wave; (b) the area with added energy is expanded and a high-temperature-low-density bubble is generated; (c) the pressure gradient of the shock wave and the density gradient of the bubble interact and shock wave is deformed; and (d) the vortex ring is generated by the baroclinic effect, the cross-term in Eq. (1.2).

$$\frac{D\boldsymbol{\omega}}{Dt} = (\boldsymbol{\omega}\cdot\nabla)\boldsymbol{u} - \boldsymbol{\omega}(\nabla\cdot\boldsymbol{u}) + \frac{1}{\rho^2}\nabla\rho\times\nabla p \tag{1.2}$$

Under repetitive pulse energy depositions, these vortex rings enhance the drag reduction performance when the rings are moving along the bodies because the pressure of the rings is lower than static pressure. The schematic illustration is shown in Fig. 1.2. The pressure distribution of the body surface is mitigated owing to this shock wave deformation and the presence of the vortex ring. As a result, the drag is reduced. The pressure distribution mitigation and the drag reduction with shock wave deformation have already been provided[29,34] and the vortex ring behavior of this model agrees with the past results qualitatively, but a quantitative comparison has not been given.

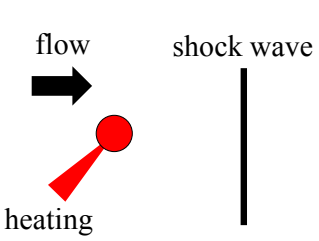

(a) energy adding

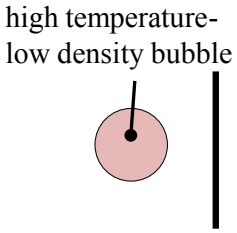

(b) expansion of heated area

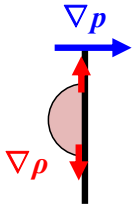

(c) interaction with shock wave

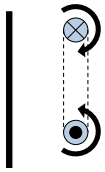

(d) vortex generation

Figure 1.1 Mechanism of baroclinic vortex ring generation.

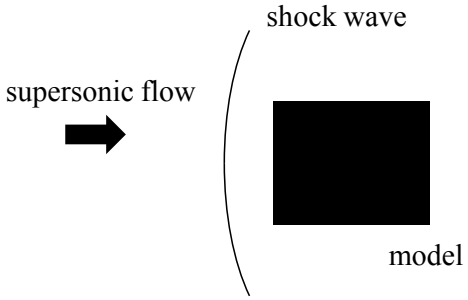

(a) without energy deposition

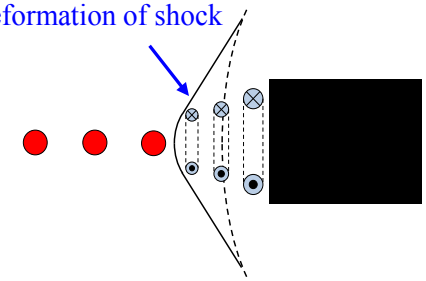

(b) with repetitive pulse energy deposition

Figure 1.2 Mechanism of supersonic drag reduction using repetitive pulse energy deposition.

1.4 Performances Evaluation of Drag Reduction

Force measurement systems have important roles to evaluate the performance of the drag reduction by wind tunnel experiment; the properly attitude, zero angle of attack, is confirmed by measuring zero lift for symmetric model; the aerodynamics performance L/D can be evaluated by measuring both lift and drag force. In this thesis, the drag reduction mechanisms are mainly discussed by qualitative comparison of experiment and simulation, but quantitatively comparison is also conducted. There is an in-draft wind tunnel with laser energy supplying system in Nagoya University. The test section of this wind tunnel is a square cross section of 80×80 mm^2. The requirement to accurately measure aerodynamic performance without causing unstart is a problem. The drag force measurement system was developed using a load cell balance system, as described in Ref 40. This method is able to measure the axial force, however it cannot measure the shear forces, such as the lift force or pitch moment. We could not find an affordable multi-component force balance in commercial products; therefore, a simple and small force balance system must be developed. We introduced a ring force balance system developed by Kawazoe et al.[41] Additionally, as shown in Section 1.2, the drag reduction performance is evaluated by ΔD and η, but L/D is the important aerodynamics performance for practical use. To obtain both the drag reduction and the aerodynamics performance using repetitive pulse laser energy deposition by wind tunnel experiment, lift and drag forces must be measured.

1.5 Objective and Structure of This Thesis

The objective of this thesis is to numerically investigate the relation between the drag reduction mechanisms of repetitive energy deposition and the baroclinic vortex ring behavior by a quantitative comparison with experimental results.

In Chapter 2, the method used in this investigation is described in detail. In this investigation, both experimental and numerical approaches are adopted. In this chapter, both the experimental apparatus and the numerical method are described. In particular, the ring force balance system[42] which is employed the experimental force measurement method is newly developed.

In Chapter 3, the drag reduction mechanism of repetitive energy depositions over a blunt body is analyzed in detail.[43] The parameters of energy deposition used in numerical calculation are determined by fitting to the experimental data. The baroclinic vortex ring behavior and time history of the drag are related by single pulse energy deposition. Then, the effect of the repetitive pulse energy deposition is discussed. From these results, it is clear that the baroclinic vortex ring behavior has an important role to play in drag reduction and it can be characterized by the vortex ring residence time in the shock layer.

Chapter 4 describes the combined effect of energy deposition and the conical spike.[44] A successful demonstration of the combined effect was provided.[14,45] The drag reduction performance of the blunt body with a conical spike model is investigated in detail. The length and the half apex angle of the conical spike are used as parameters and the resulting performance shows that the combined effect is seen under a lower repetition frequency. At a higher repetition frequency, the effect of the energy deposition exceeds that of the conical spike.

Chapter

2

Experimental Apparatus and Numerical Method

2.1 Experimental Apparatus

All experiments are conducted in an in-draft wind tunnel.[21,40,45] The schematic illustration is shown in Fig. 2.1. The intake of the wind tunnel has a 440 mm × 440 mm square cross-section and is connected to a rectangular, convergent-divergent nozzle where design Mach number is 2.0. The test section has a cross-section of an 80 mm × 80 mm square. The volume of the dump tank equals 11.5 m^3. The effective run time is 5 seconds. From measurement using a Pitot lake, the test flow has a 30 mm × 30 mm square core in which a measured Mach number equals 1.92 ± 0.04. The error of the measured Mach number means spatial variation in the test flow core. The pressure of 13.8 kPa measured at the test section on the wall is assumed to equal to a static pressure of the test flow, the static temperature evaluated from isentropic expansion process is 163 K.

Highly-repetitive pulse lasers (Nd:YVO_4 and Nd:YLF, which specs are shown in Table 2.1) were used as the source of the energy deposition. The output laser beam was expanded to 15 mm × 15mm square after reflecting by three dielectric multilayer plane mirrors of its

reflection angle of 45 degrees, and the expanded beam was focused in front of the model through BK-7 windows by using LightPath® GRADIUM® convex lens of its focal length of 60 mm.

The flow structure around the model was visualized by Z-shaped Schlieren method and that was framed using high speed cameras (HPV-1 and Ultra Cam HS-106E, which specs are shown in Table 2.2).

Table 2.1 Spec of repetitive pulse lasers.

	$Nd:YVO_4$	Nd:YLF
company	Edgewave	Edgewave
wavelength	1064 nm	1064 nm
pulse duration	10 ± 0.6 ns	7 ns
beam cross section	6 mm × 6 mm	
repetition frequency	up to 100 kHz	up to 10 kHz
average power	up to 400 W	up to 85 W

Table 2.2 Spec of high speed cameras.

	HPV-1	Ultra Cam HS-106E
company	Shimadzu Corporation	nac image Technology Inc.
resolution	312×260 pixels	360×410 pixels
framing rate	2.0×10^5 frames/s (1.0×10^6 frames/s maximum)	2.0×10^5 frames/s (1.25×10^6 frames/s maximum)
frame numbers	100 frames	120 frames

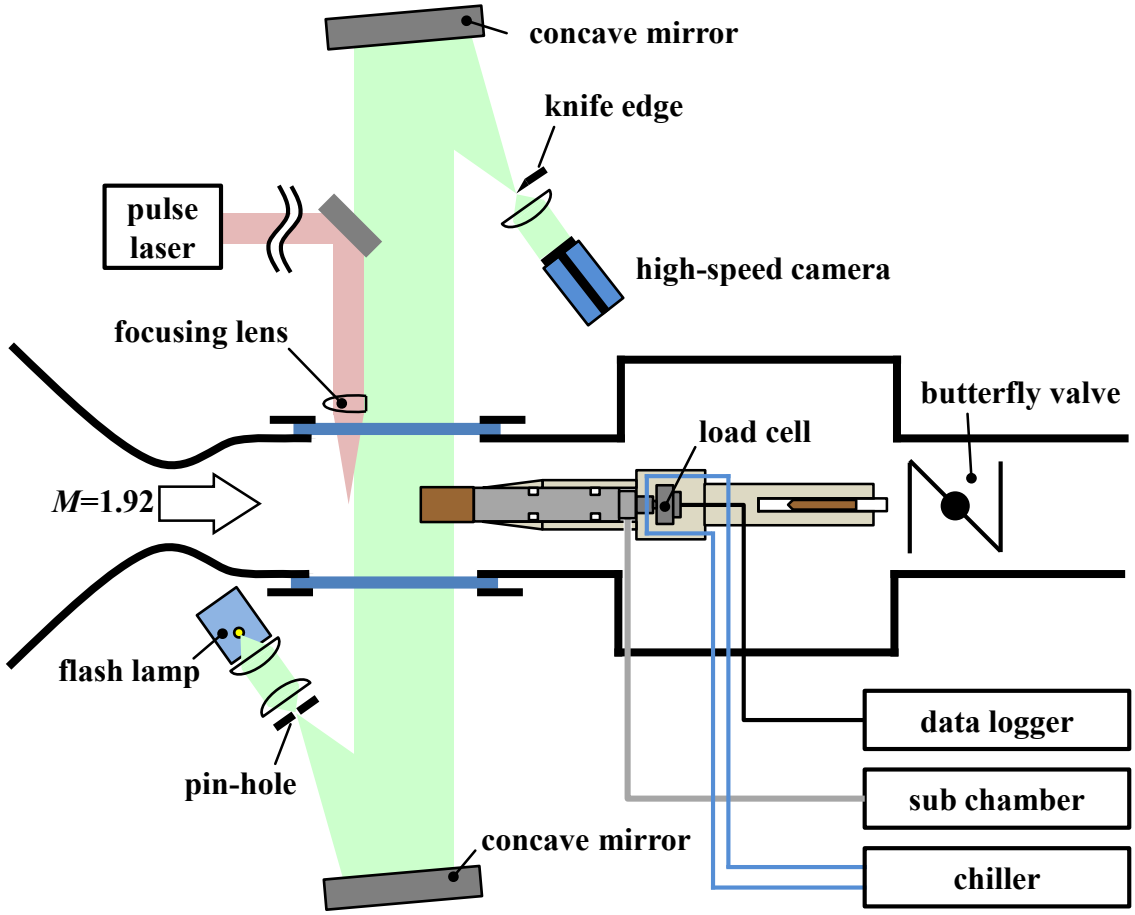

Figure 2.1 Experimental apparatus.

2.2 Ring Force Balance System

In this investigation, a ring force balance system for a supersonic wind tunnel with a small test section is designed, developed, and calibrated. The theoretical analysis of infinitesimally thin ring force balance is provided by Kawazoe et al.[41], and is described in Appendix A. The effect of the thickness, the support arm and the size of the strain gauge are described following.

2.2.1 Theory of the Ring Force Balance with a Finite Thickness

For an ideal ring force balance, the thickness of the ring portion was assumed to be zero. However, the ring force balance in practical use has a finite thickness. In this section, to estimate the effects of the thickness, the finite thickness t_r is considered.

2.2.1.1. Strain Due to the Drag Force

The application of force D is the same as infinitesimally thin case, where N_{D1} and M_{D1} occur at point B, as shown in Fig. 2.2. $M_{D\theta}$, $P_{D\theta}$, and $N_{D\theta}$ at position θ are written as follows.

$$M_{D\theta} = M_{D1} - N_{D1}R(1-\cos\theta) + \frac{1}{2}DR\sin\theta \tag{2.1}$$

$$P_{D\theta} = \frac{1}{2}D\cos\theta - N_{D1}\sin\theta \tag{2.2}$$

$$N_{D\theta} = \frac{1}{2}D\sin\theta + N_{D1}\cos\theta \tag{2.3}$$

Here, $P_{D\theta}$ can be ignored because its direction is perpendicular to the strain of interest. dU is written as follows.

$$\begin{aligned} dU &= \left(\frac{M_{D\theta}^2}{2EI} + \frac{N_{D\theta}^2}{2EA} \right) ds \\ &= \frac{1}{2EI} \left(M_{D1} - N_{D1} R(1-\cos\theta) + \frac{1}{2} DR\sin\theta \right)^2 ds \\ &\quad + \frac{1}{2EA} \left(\frac{1}{2} D\sin\theta + N_{D1}\cos\theta \right)^2 ds \end{aligned} \tag{2.4}$$

Using the relation $ds = Rd\theta$, U is written as follows.

$$\begin{aligned} U = \int_0^{\pi} \Bigg\{ & \frac{1}{2EI} \left(M_{D1} - N_{D1} R(1-\cos\theta) + \frac{1}{2} DR\sin\theta \right)^2 \\ & + \frac{1}{2EA} \left(\frac{1}{2} D\sin\theta + N_{D1}\cos\theta \right)^2 \Bigg\} Rd\theta \end{aligned} \tag{2.5}$$

Here, U, N_{D1}, and M_{D1} must satisfy the theorem of least work; therefore, $\partial U/\partial M_{D1} = 0$ and $\partial U/\partial N_{D1} = 0$.

$$\frac{\partial U}{\partial M_{D1}} = \frac{2R}{2EI} \left\{ M_{D1}\pi - N_{D1} R\pi + DR \right\} \tag{2.6}$$

$$\frac{\partial U}{\partial N_{D1}} = \frac{2R^2}{2EI} \left\{ -M_{D1}\pi + \frac{3}{2} N_{D1} R\pi - DR \right\} + \frac{R}{2EA} N_{D1}\pi \tag{2.7}$$

From Eqs. (2.6) and (2.7), $N_{D1} = 0$ and $M_{D1} = -DR/\pi$ are obtained. These results are applied to Eqs. (2.1), (2.2), and (2.3), and then $M_{D\theta}$, $P_{D\theta}$, and $N_{D\theta}$ are obtained as follows.

$$M_{D\theta} = \frac{1}{2} DR \left(\sin\theta - \frac{2}{\pi} \right) \tag{2.8}$$

$$P_{D\theta} = \frac{1}{2} D\cos\theta \tag{2.9}$$

$$N_{D\theta} = \frac{1}{2} D\sin\theta \tag{2.10}$$

Therefore, ε_{D1} caused by $M_{D\theta}$ and $N_{D\theta}$ is obtained as follows.

$$\varepsilon_{\mathrm{D1}} = -\frac{1}{EA}N_{\mathrm{D}\theta} + \frac{h}{EI}M_{\mathrm{D}\theta} = \frac{D}{E}\left\{-\frac{1}{2A}\sin\theta + \frac{h}{2I}R\left(\sin\theta - \frac{2}{\pi}\right)\right\} \tag{2.11}$$

If the ring part has a rectangular cross section with respect to the thickness t and a width w, $h = \frac{1}{2}t_{\mathrm{r}}$, $I = \frac{1}{12}wt_{\mathrm{r}}^3$, and $A = wt_{\mathrm{r}}$ are obtained. These are applied to Eq. (2.11), and $\varepsilon_{\mathrm{D1}}$ is obtained as follows.

$$\varepsilon_{\mathrm{D1}} = \frac{D}{2wt_{\mathrm{r}}E}\left\{\sin\theta\left(\frac{6R}{t_{\mathrm{r}}} - 1\right) - \frac{6R}{t_{\mathrm{r}}}\frac{2}{\pi}\right\} \tag{2.12}$$

From Eq. (2.12), the azimuthal location θ_{D1} where $\varepsilon_{\mathrm{D1}} = 0$ is always satisfied is given as follows.

$$\theta_{\mathrm{D1}}\left(\frac{t_{\mathrm{r}}}{R}\right) = \sin^{-1}\left(\frac{2}{\pi} \times \frac{1}{1 - t_{\mathrm{r}}/6R}\right) \tag{2.13}$$

θ_{D1} is a function of t_{r}/R. The relation between θ_{D1} and t_{r}/R is shown in Fig. 2.3. No strain point is corrected using the finite thickness t_{r}.

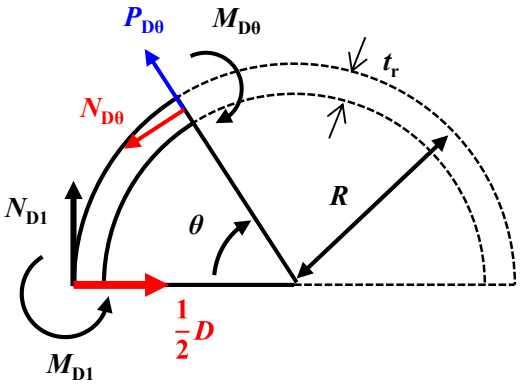

Figure 2.2 Exerted force on the upper ring half with a ring thickness t_{r} when D is applied.

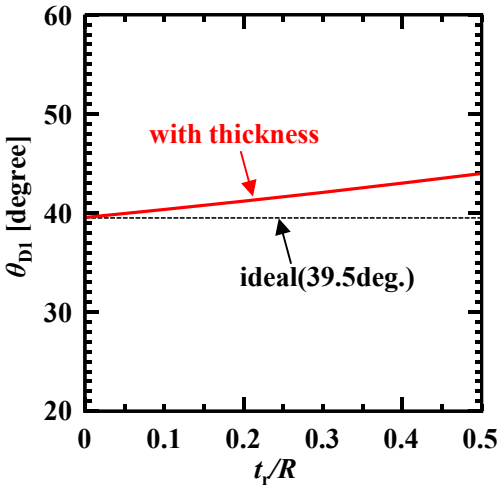

Figure 2.3 Effects of the thickness of the ring portion.

2.2.1.2. Strain Due to the Lift Force

The application of force L is the same as infinitesimally thin case, where P_{L1} and M_{L1} occur at point B, as shown in Fig. 2.4. $M_{L\theta}$, $P_{L\theta}$, and $N_{L\theta}$ at position θ are written as follows.

$$M_{L\theta} = M_{L1} - \frac{1}{2}LR(1-\cos\theta) + P_{L1}R\sin\theta \tag{2.14}$$

$$P_{L\theta} = P_{L1}\cos\theta - \frac{1}{2}L\sin\theta \tag{2.15}$$

$$N_{L\theta} = P_{L1}\sin\theta + \frac{1}{2}L\cos\theta \tag{2.16}$$

$P_{L\theta}$ can be ignored because the direction is perpendicular to the strain of interest. dU is written as follows.

$$\begin{aligned} dU &= \left(\frac{M_{L\theta}^2}{2EI} + \frac{N_{L\theta}^2}{2EA}\right)ds \\ &= \frac{1}{2EI}\left(M_{L1} - \frac{1}{2}LR(1-\cos\theta) + P_{L1}R\sin\theta\right)^2 ds \\ &\quad + \frac{1}{2EA}\left(P_{L1}\sin\theta + \frac{1}{2}L\cos\theta\right)^2 ds \end{aligned} \tag{2.17}$$

Using the relation $ds = Rd\theta$, U is written as follows.

$$\begin{aligned} U = \int_0^{\pi} \Bigg\{ &\frac{1}{2EI}\left(M_{L1} - \frac{1}{2}LR(1-\cos\theta) + P_{L1}R\sin\theta\right)^2 \\ &+ \frac{1}{2EA}\left(P_{L1}\sin\theta + \frac{1}{2}L\cos\theta\right)^2 \Bigg\} Rd\theta \end{aligned} \tag{2.18}$$

Here, U, P_{L1}, and M_{L1} must satisfy the theorem of least work; therefore, $\partial U/\partial M_{L1} = 0$ and $\partial U/\partial P_{L1} = 0$.

$$\frac{\partial U}{\partial M_{L1}} = \frac{2R}{2EI}\left\{M_{L1}\pi - \frac{1}{2}LR\pi + 2P_{L1}R\right\} \tag{2.19}$$

$$\frac{\partial U}{\partial P_{L1}} = \frac{2R^2}{2EI}\left\{2M_{L1} - LR + \frac{1}{2}P_{L1}R\pi\right\} + \frac{\pi R}{2EA}P_{L1} \tag{2.20}$$

From Eqs. (2.19) and (2.20), $P_{L1} = 0$ and $M_{L1} = \frac{1}{2}LR$ are obtained. These are applied

to Eqs. (2.14), (2.15) and (2.16), and then $M_{L\theta}$, $P_{L\theta}$, and $N_{L\theta}$ are obtained as follows.

$$M_{L\theta} = \frac{1}{2}LR - \frac{1}{2}LR(1-\cos\theta) = \frac{1}{2}LR\cos\theta \tag{2.21}$$

$$P_{L\theta} = \frac{1}{2}L\sin\theta \tag{2.22}$$

$$N_{L\theta} = \frac{1}{2}L\cos\theta \tag{2.23}$$

Therefore, ε_{L1} caused by $M_{L\theta}$ and $N_{L\theta}$ is obtained as follows.

$$\varepsilon_{L1} = -\frac{1}{EA}N_{L\theta} + \frac{h}{EI}M_{L\theta} = \frac{1}{2E}\left(-\frac{1}{A} + \frac{hR}{I}\right)L\cos\theta \tag{2.24}$$

From Eq. (2.24), the azimuthal location where $\varepsilon_{L1} = 0$ is always satisfied remains at $\theta_{L1} = \pi/2 = 90°$ as the azimuthal distribution of the strain caused by the lift is not affected by the thickness.

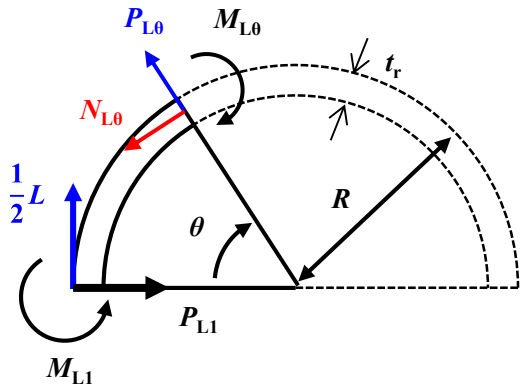

Figure 2.4 Exerted force on the upper ring half with a ring thickness t_r when L is applied.

2.2.1.3. Strain Due to the Pitching Moment

The application of moment M_P is the same as infinitesimally thin case, where P_{M1} and N_{M1} occur at point B, as shown in Fig. 2.5. $M_{M\theta}$, $P_{M\theta}$, and $N_{M\theta}$ at position θ are written as M_P, P_{M1}, and N_{M1}, respectively, and described as follows.

$$M_{M\theta} = M_P - N_{M1} R(1-\cos\theta) + P_{M1} R\sin\theta \tag{2.25}$$

$$P_{M\theta} = P_{M1}\cos\theta - L_{M1}\sin\theta \tag{2.26}$$

$$N_{M\theta} = P_{M1}\sin\theta + N_{M1}\cos\theta \tag{2.27}$$

$P_{M\theta}$ can be ignored because the direction is perpendicular to the strain of interest. The strain ε_{M1} caused by $N_{M\theta}$ and $M_{M\theta}$ is written as follows.

$$\varepsilon_{M1} = -\frac{1}{EA} N_{M\theta} + \frac{\eta}{EI} M_{M\theta} \tag{2.28}$$

Eqs. (2.25) and (2.27) are applied to Eq. (2.28), and ε_{M1} is written as follows.

$$\begin{aligned}\varepsilon_{M1} &= -\frac{1}{EA}(P_{M1}\sin\theta + N_{M1}\cos\theta) + \frac{h}{EI}(M_P - N_{M1}R(1-\cos\theta) + P_{M1}R\sin\theta) \\ &= \left(-\frac{1}{EA} + \frac{h}{EA}\right)P_{M1}\sin\theta + \left(-\frac{1}{EA} + \frac{h}{EA}\right)N_{M1}\cos\theta + \frac{h}{EI}\left(M_P - N_{M1}R\right)\end{aligned} \tag{2.29}$$

From Eq. (2.29), the azimuthal location θ where $\varepsilon_{M1} = 0$ is always satisfied does not exist.

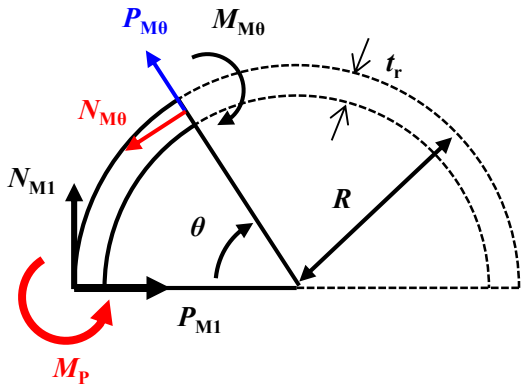

Figure 2.5 Exerted force on the upper ring half with a ring thickness t_r when M_p is applied.

2.2.2 Theory of the Ring Force Balance with a Support Arm

For practical use, we must account for the effects of support arms. Here, the lengths of both the fore- and aft-support arms are assumed to be l_s, as shown in Fig. 2.6. Forces and moments are applied at point C, and the moments, due to the effects of the support arm, are applied to points A and B. The drag force is not affected because the force direction is parallel to the arm. The pitching moment is also not affected by the arm because the moment exerted by the pitching component at point B is the same as the pitching moment applied at point C. In this section, the strain caused by L and the moment Ll_s are calculated independently, as shown in Fig. 2.7. Then, the total strain can be calculated by the summation of the strains caused by L and Ll_s.

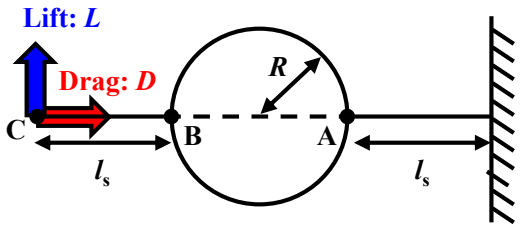

Figure 2.6 Schematic of the ring force balance with a support arm.

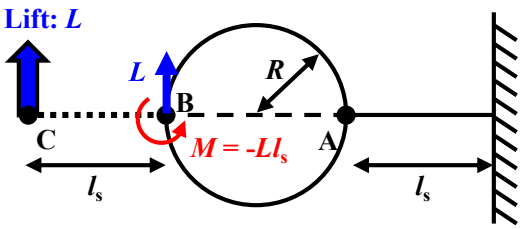

Figure 2.7 Equivalent model of the ring force balance with a support arm when L is applied at point C.

2.2.2.1. Strain Due to Lift *L*

When L is applied at point B, M_a and P_a occur, as shown in Fig. 2.8. $M_{L\theta}$ at position θ is written as follows.

$$M_{L\theta} = M_a - \frac{1}{2}LR(1-\cos\theta) + P_a R\sin\theta \tag{2.30}$$

When connection point A is used as the origin, M_{L2} acting on the support arm from the fixed end is written as follows.

$$M_{L2} = M_{L\theta}\big|_{\theta=\pi} - \frac{1}{2}Lx = M_a - LR - \frac{1}{2}Lx \tag{2.31}$$

Using the same method as the previous sections, U is defined in terms of L, P_a, and M_a.

$$\begin{aligned} U &= \int_0^{\pi} \frac{(M_{L\theta})^2}{2EI} ds + \int_0^{l_s} \frac{(M_{L2})^2}{2EI} dx \\ &= \frac{1}{2EI}\int_0^{\pi} \left(M_a - \frac{1}{2}LR(1-\cos\theta) + P_a R\sin\theta \right)^2 Rd\theta \\ &\quad + \frac{1}{2EI}\int_0^{l_s} \left(M_a - LR - \frac{1}{2}Lx \right)^2 dx \end{aligned} \tag{2.32}$$

Here U, M_a, and P_a must satisfy the theorem of least work; therefore, $\partial U/\partial M_a = 0$ and $\partial U/\partial P_a = 0$.

$$\frac{\partial U}{\partial M_a} = \frac{2}{2EI}\left\{ M_a(R\pi + l_s) + 2P_a R^2 + \left(-\frac{1}{2}R^2\pi - Rl_s - \frac{1}{4}l_s^2 \right) L \right\} \tag{2.33}$$

$$\frac{\partial U}{\partial P_a} = \frac{2R^2}{2EI}\left\{ 2M_a - LR + \frac{1}{2}P_a R\pi \right\} \tag{2.34}$$

From Eqs. (2.33) and (2.34), M_a and P_a are obtained as follows.

$$M_a = \frac{LR}{4} \times \frac{2(\pi^2 - 8) + {}^{l_s}\!/_{R}\,\pi(4 + {}^{l_s}\!/_{R})}{(\pi^2 - 8) + {}^{l_s}\!/_{R}\,\pi} \tag{2.35}$$

$$P_a = -\frac{Ll_s}{R} \times \frac{2 + {}^{l_s}\!/_{R}}{(\pi^2 - 8) + {}^{l_s}\!/_{R}\,\pi} \tag{2.36}$$

Then, Eqs. (2.35) and (2.36) are applied to Eq. (2.30).

$$
\begin{aligned}
M_{\mathrm{L}\theta} &= \frac{1}{2} L \left\{ \frac{l_{\mathrm{s}}}{2} \frac{2R + l_{\mathrm{s}}}{R(\pi^2 - 8) + l_{\mathrm{s}}\pi} (\pi - 4\sin\theta) + R\cos\theta \right\} \\
&= \frac{1}{2} L l_{\mathrm{s}} \left\{ \frac{1}{2} \frac{2 + {}^{l_{\mathrm{s}}}\!/_{R}}{(\pi^2 - 8) + {}^{l_{\mathrm{s}}}\!/_{R}\,\pi} (\pi - 4\sin\theta) + \frac{1}{{}^{l_{\mathrm{s}}}\!/_{R}} \cos\theta \right\} \\
&= \frac{1}{2} L l_{\mathrm{s}} \times f\left({}^{l_{\mathrm{s}}}\!/_{\mathrm{R}}, \theta \right)
\end{aligned}
\tag{2.37}
$$

These $M_{\mathrm{L}\theta}$, M_{a}, and P_{a} equations are consistent with the ideal ring force balance when substituting $l_{\mathrm{s}} = 0$.

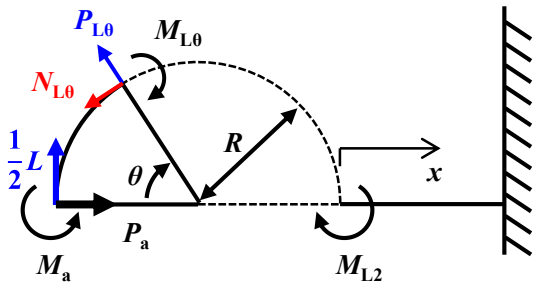

Figure 2.8 Exerted force on the upper ring half with a support arm when L is applied.

2.2.2.2. Strain Due to Moment Ll_s

When Ll_s is applied at point B, P_b and N_b occur, as shown in Fig. 2.9. $M_{M\theta}$ at position θ is written as follows.

$$M_{M\theta} = -\frac{1}{2}Ll_s - N_b R(1-\cos\theta) + P_b R\sin\theta \tag{2.38}$$

When point A is used as the origin, M_{M2} acting on the support arm from the fixed end is written as follows.

$$M_{M2} = M_{M\theta}\big|_{\theta=\pi} + N_b x = -\frac{1}{2}Ll_s + 2N_b R + N_b x \tag{2.39}$$

U is defined in terms of L, P_b and N_b.

$$\begin{aligned} U &= \int_0^{\pi}\frac{(M_{M\theta})^2}{2EI}ds + \int_0^{l_s}\frac{(M_{M2})^2}{2EI}dx \\ &= \frac{1}{2EI}\int_0^{\pi}\left(-\frac{1}{2}Ll_s - N_b R(1-\cos\theta) + P_b R\sin\theta\right)^2 Rd\theta \\ &\quad + \frac{1}{2EI}\int_0^{l_s}\left(-\frac{1}{2}Ll_s + 2N_b R + N_b x\right)^2 dx \end{aligned} \tag{2.40}$$

Here, U, P_b, and N_b must satisfy the theorem of least work; therefore, $\partial U/\partial P_b = 0$ and $\partial U/\partial N_b = 0$.

$$\frac{\partial U}{\partial P_b} = \frac{2R^2}{2EI}\left\{-Ll_s - 2N_b R + \frac{1}{2}P_b R\pi\right\} \tag{2.41}$$

$$\frac{\partial U}{\partial N_b} = \frac{2R}{2EI}\left\{N_b\left(\frac{3}{2}R^2\pi + 2Rl + \frac{1}{2}l_s^2\right) - 2P_b R^2 + \frac{1}{2}Ll_s\left(R\pi - l_s\right)\right\} \tag{2.42}$$

From Eqs. (2.41) and (2.42), P_b and N_b are obtained as follows.

$$P_b = \frac{2Ll_s}{R}\frac{\pi + {}^{l_s}\!/_{R}\,(6 + {}^{l_s}\!/_{R})}{(3\pi^2 - 16) + \pi\,{}^{l_s}\!/_{R}\,(4 + {}^{l_s}\!/_{R})} \tag{2.43}$$

$$N_b = -\frac{Ll_s}{R}\frac{(\pi^2 - 8) - \pi\,{}^{l_s}\!/_{R}}{(3\pi^2 - 16) + \pi\,{}^{l_s}\!/_{R}\,(4 + {}^{l_s}\!/_{R})} \tag{2.44}$$

Then, Eqs. (2.43) and (2.44) are applied to Eq. (2.38), and $M_{M\theta}$ is written as follows.

$$\begin{aligned} M_{M\theta} &= \frac{1}{2} L l_s \frac{1}{(3\pi^2 - 16) + \pi\, {}^{l_s}\!/_{R} \left(4 + {}^{l_s}\!/_{R}\right)} \Big[-\pi^2 - 6\, {}^{l_s}\!/_{R}\, \pi + \pi \left({}^{l_s}\!/_{R}\right)^2 \\ &\quad - \left\{2(\pi^2 - 8) - 2\pi\, {}^{l_s}\!/_{R}\right\} \cos\theta + \left\{4\pi + 4\, {}^{l_s}\!/_{R} \left(6 + {}^{l_s}\!/_{R}\right)\right\} \sin\theta \Big] \\ &= \frac{1}{2} L l_s \times g\left({}^{l_s}\!/_{R}, \theta\right) \end{aligned} \tag{2.45}$$

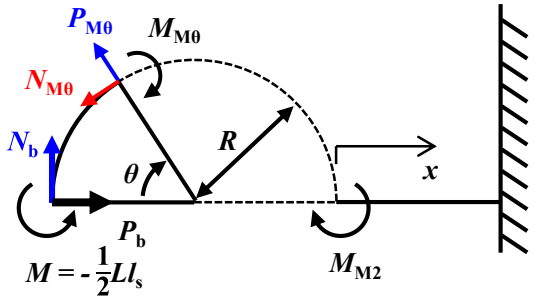

Figure 2.9 Exerted force on the upper ring half with a support arm when Ll_s is applied.

2.2.2.3. Total Strain Due to *L* with a Support Arm

$M_{\theta 2}$ due to L and Ll_s at position θ is:

$$M_{\theta 2} = M_{L\theta} + M_{M\theta} \tag{2.46}$$

where $M_{L\theta}$ and $M_{M\theta}$ are described in Eqs. (2.37) and (2.45), respectively. Therefore, $\varepsilon_{\theta 2}$ at position θ is written as follows.

$$\begin{aligned} \varepsilon_{\theta 2} &= \frac{M_{\theta 2}}{EI}\eta = \frac{M_{L\theta} + M_{M\theta}}{EI}\eta \\ &= \frac{\eta L l_s}{2EI}\left(f(l_s/R, \theta) + g(l_s/R, \theta)\right) \end{aligned} \tag{2.47}$$

The strain of position θ obtained from Eq. (2.47) is shown in Fig. 2.10. In this figure, $C = \eta L/2EI$. The azimuthal location where $\varepsilon_{\theta 2} = 0$ is always satisfied is changed by l_s/R.

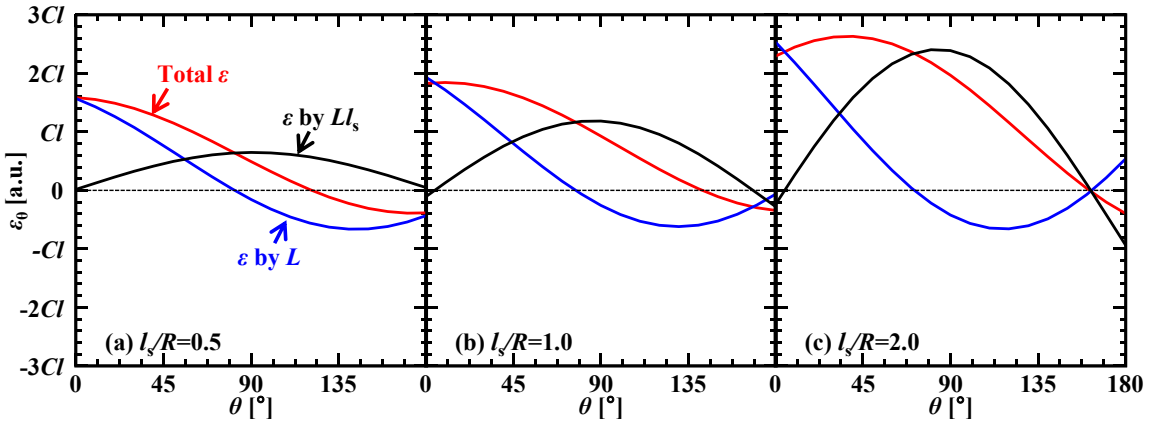

Figure 2.10 Strain depends on the angle when the support arm is considered.

2.2.3 Effects of the Length of the Strain Gauge

The force components can be obtained by measuring the strain at the position of no strain when D is applied and the position of no strain when L is applied. If the length of the strain gauge l_g is infinitesimally small, the force components can be measured separately. However, the strain gauge has a finite length. For the design and practical use of the ring force balance using the strain gauge, evaluating the effects of l_g is important.

2.2.3.1. Effects on the Drag Measurements

l_g is written by using R and $d\theta$, and these relations are shown in Fig. 2.11.

$$l_g = Rd\theta \tag{2.48}$$

The strain at θ_g when D is applied can be obtained from Eq. (A.9), and the measured strain can be obtained by integrating $\varepsilon(\theta) = R\mathrm{d}\theta$ from θ_g-$d\theta/2$ to θ_g+$d\theta/2$ when using the length of the strain gauge l_g.

$$\begin{aligned}\varepsilon(\theta) &= \int_{\theta_g - d\theta/2}^{\theta_g + d\theta/2} \frac{\eta D R^2}{2EI}\left(\sin\theta - \frac{2}{\pi}\right)d\theta \\ &= \frac{\eta D R^2}{2EI}\left[2\sin\theta_g \sin(d\theta/2) - \frac{2}{\pi}d\theta\right]\end{aligned} \tag{2.49}$$

As described in Section 1.4, the lift-to-drag ratio is the important for evaluating the performances. Hence, the measurement error of the lift-to-drag ratio, e is introduced. The e of l_g is defined as the strain ratio at the position θ_D and θ_L.

$$\begin{aligned}e &= \frac{\varepsilon(\theta_D)}{\varepsilon(\theta_L)} \\ &= \frac{2/\pi\, d\theta - 2\sin\theta_D \sin(d\theta/2)}{2/\pi\, d\theta - 2\sin\theta_L \sin(d\theta/2)} \\ &= \frac{d\theta - 2\sin(d\theta/2)}{d\theta - \pi\sin(d\theta/2)}\end{aligned} \tag{2.50}$$

Here, $\sin\theta_D = 2/\pi$ and $\theta_L = \pi/2$. If l_g is infinitesimally small, $\varepsilon(\theta_D)$ becomes zero. This

indicates $e = 0$. Figure 2.12 shows the relation between e and $d\theta = l_g/R$. e diverges at $d\theta = \pi$. When the same strain gauge length is used for drag and lift force measurement, the interference between these gauges must be eliminated. If the positions of these gauges are θ_{D0} and θ_{L0}, respectively, the allowable length for practical use is determined by geometric relation; $d\theta \leq \theta_{L0} - \theta_{D0}$. e is 6.1% at this case. To suppress the effect of the gauge length, the length of the strain gauge should be small enough or the radius of the ring part should be large enough.

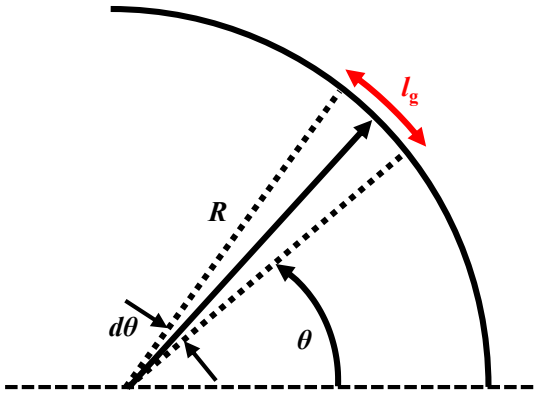

Figure 2.11 Strain gauge length and considered model.

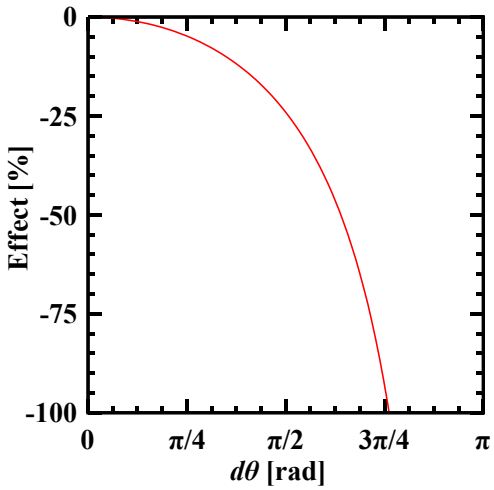

Figure 2.12 Effects of the strain gauge length.

2.2.4 Ring Force Balance Design and Calibration

2.2.4.1. Design of the Ring Force Balance

A ring force balance for force measurements in a supersonic wind tunnel with a small test section was designed and fabricated by the above theory. The designed balance consists of a fore arm, a ring part, and an aft arm. The fore arm is connected to the test model, and the aft arm is connected to a strut. The ring part can measure the force components. The force components are obtained by measuring the strain on the ring part using a small semiconductor strain gauge. The strain gauge is attached to the surface of the ring part using CN adhesives (General purpose, Tokyo Sokki Kenkyuujo Co., Ltd.). A schematic of the designed balance is shown in Fig. 2.13. The diameter and thickness of the ring part are 9.0 mm and 4.3 mm, respectively. In this configuration, the azimuthal location of no strain is 43.7° when drag is applied. In order to eliminate the influence of vibrations and starting load on the balance, the balance was constructed of SUS630. The strain of the ring part is measured by small semiconductor strain gauges (KSN-2-120-E4-11, resistance; 120 Ω, gauge factor; -100, length; 2 mm ($d\theta$ = 12.7°), KYOWA) that have higher sensitivities than metal strain gauges. A set of strain gauges was installed at θ = 40, 90°, and in line with the support arms. The effect of the fabricated strain gauge size, evaluated by Eq. (2.50), is at most 3.6×10^{-1}%.

The sets of strain gauges G1 and G3, shown in Fig. 2.14, were connected to the half-bridge circuit such as the one shown in Fig. 2.14 (a). The set of the strain gauges G2 was connected to the half-bridge circuit of two opposite side such as the one shown in Fig. 2.14 (b). Strain is translated to an electric signal using these circuits. The amount of strain caused by an applied force is measured by translating the rate of change of the electrical resistance.

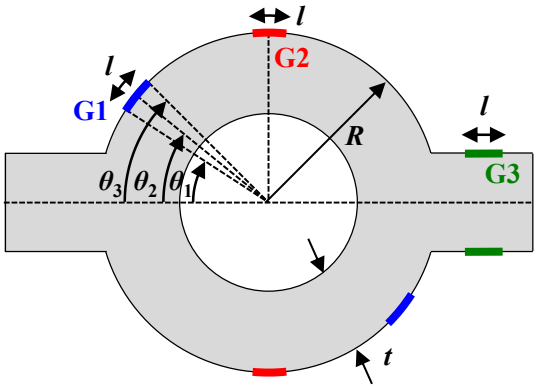

Figure 2.13 Schematic of the designed ring force balance.

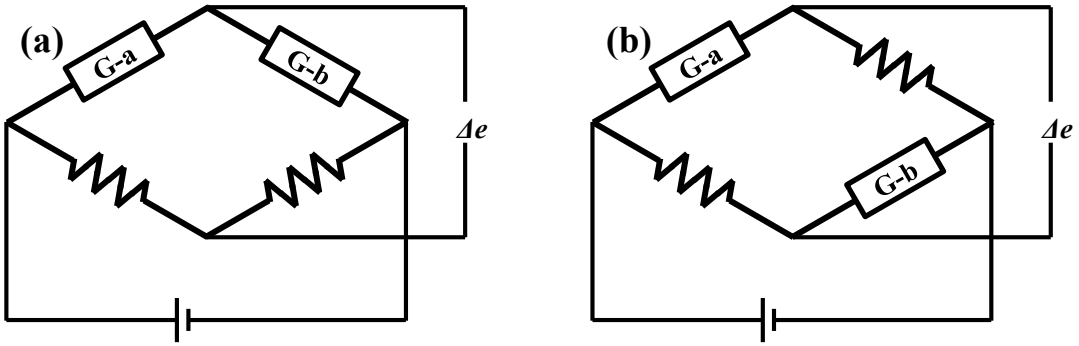

Figure 2.14 Circuit of the strain gauge: (a) half bridge with two active gauges and (b) opposite side half bridge with two active gauges.

2.2.4.2. Temperature Compensation

Two kinds of apparent strain occur from a temperature change. One is the resistance change of the strain gauge, and the other is the difference in the linear thermal expansion coefficient between the strain gauge and the material of the force balance. The apparent strain caused by the resistance change of the strain gauge ε_r is written as follows.

$$\varepsilon_r = \alpha \times \frac{\Delta T}{F_s} \tag{2.51}$$

The apparent strain caused by the difference of the linear thermal expansion coefficient ε_t is written as follows.

$$\varepsilon_t = \varepsilon_m - \varepsilon_s = (\beta_m - \beta_s)\Delta T \tag{2.52}$$

Hence, the apparent strain caused by a temperature change ε_T is obtained by the summation of Eqs. (2.51) and (2.52).

$$\begin{aligned} \varepsilon_T &= \varepsilon_r + \varepsilon_t \\ &= \alpha \times \frac{\Delta T}{F_s} + (\beta_m - \beta_s)\Delta T \\ &= \left(\frac{\alpha}{F_s} + (\beta_m - \beta_s) \right) \Delta T \end{aligned} \tag{2.53}$$

The parameters of the designed ring force balance are shown in Table 2.3. From Eq. (2.53) and Table 2.3, the apparent strain of the balance is $\varepsilon_T = -1.0 \times 10^{-6} \Delta T$. This compensation is used for the G2 gauge because the apparent strain is canceled at the half-bridge circuit for gauges G1 and G3.

Table 2.3 Parameters for apparent strain.

Parameter	Value
α/F_s	-0.80×10^{-6} [1/T]
β_m	10.8×10^{-6} [1/T]
β_s	11.0×10^{-6} [1/T]

2.2.4.3. Calibration of the Ring Force Balance

The calibration apparatus is shown in Figs. 2.15 and 2.16. The fore arm is connected to a cross-part rig, and the aft arm is connected to the sting. The lift and drag forces are separately loaded to the rig using weights attached to a wire and pulley system, as shown in Fig. 2.16.

The relationship among the loaded forces of each separate component and the measured strain is shown in Fig. 2.17. From Fig. 2.17, the results show a good linearity in these measurement ranges. Additionally, a strain at G2 can be suppressed when a lift force is loaded, and a strain at G1 can also be suppressed when a drag force is loaded. The calibration matrix [K] is estimated by the relationship between the measured strain and the acting load.

$$\begin{pmatrix} L \\ D \\ M_{\mathrm{p}} \end{pmatrix} = [K] \times \begin{pmatrix} \varepsilon_{\mathrm{G1}} \times 10^{-6} \\ \varepsilon_{\mathrm{G2}} \times 10^{-6} \\ \varepsilon_{\mathrm{G3}} \times 10^{-6} \end{pmatrix} \tag{2.54}$$

$$[K] = \begin{pmatrix} 1.84 \times 10^{0} & -2.92 \times 10^{-1} & -3.78 \times 10^{-2} \\ -1.00 \times 10^{-1} & 5.05 \times 10^{0} & 4.98 \times 10^{-4} \\ -3.20 \times 10^{-1} & -4.65 \times 10^{-2} & 4.39 \times 10^{-3} \end{pmatrix} \tag{2.55}$$

The measured force components using matrix [K] include the apparent strain, which occurs by a temperature change. Then the measured force components are modified by temperature compensations as follows.

$$\begin{pmatrix} L \\ D \\ M_{\mathrm{p}} \end{pmatrix} = [K] \times \begin{pmatrix} \varepsilon_{\mathrm{G1}} \times 10^{-6} \\ \varepsilon_{\mathrm{G2}} \times 10^{-6} - \varepsilon_{\mathrm{T}} \\ \varepsilon_{\mathrm{G3}} \times 10^{-6} \end{pmatrix} = \begin{pmatrix} L - 3.0 \times 10^{-1} \times \Delta T \\ D + 5.0 \times 10^{0} \times \Delta T \\ M_{\mathrm{p}} + 4.7 \times 10^{-2} \times \Delta T \end{pmatrix} \tag{2.56}$$

The lift and drag were loaded simultaneously, and the force components were evaluated from the measured strain, calibration matrix [K], and temperature compensation. The time history of the loaded lift and drag in comparison with the measured ones are shown in Fig. 2.18. From Fig. 2.18, the measured forces agree well with the loaded forces. Therefore, the

ring force balance can measure the acting force accurately even when the lift and drag act simultaneously. The measurement errors estimated from the loaded forces and measured forces are shown in Table 2.4. The maximum error is, at most, 5%. The error of measured drag is larger than that of measured lift. This error might be caused by the apparent strain because the drag has a larger compensation than the lift.

Table 2.4 Loaded forces, measured forces, and errors.

Load		Measured		Error	
L [N]	*D* [N]	*L* [N]	*D* [N]	*L* [%]	*D* [%]
0.00	0.00	0.00	0.00	-	-
0.00	1.96	0.02	2.00	-	-2.1
1.96	1.96	1.98	1.87	-1.1	4.5
3.92	1.96	3.91	1.94	0.1	1.2
5.88	1.96	5.83	1.85	0.8	5.6
5.88	3.92	5.78	3.92	1.7	-0.1
5.88	13.72	5.82	13.51	1.0	1.5

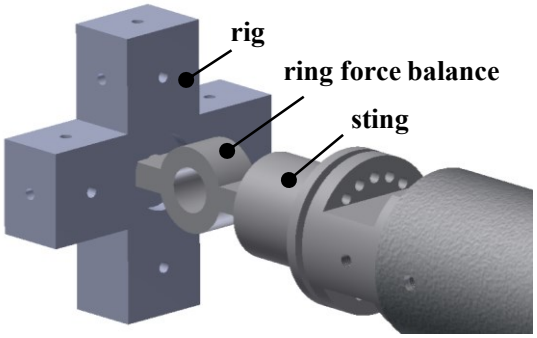

Figure 2.15 Calibration system of the ring force balance.

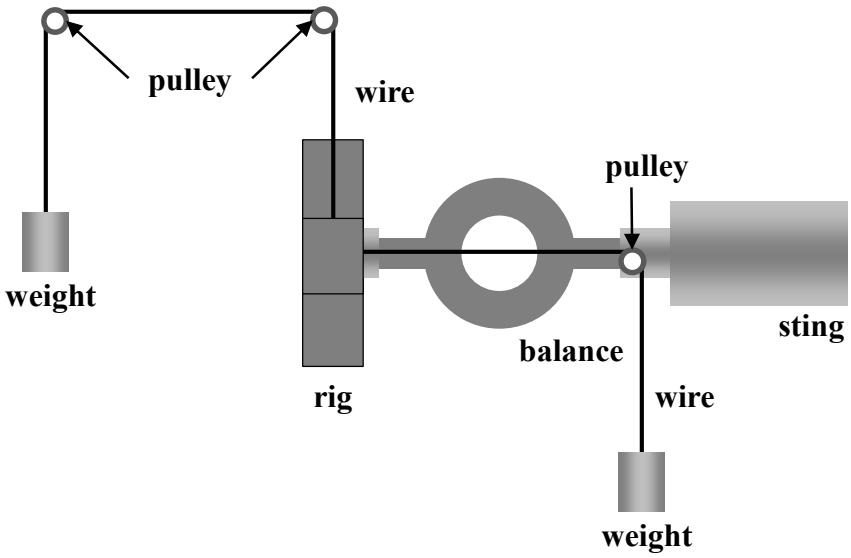

Figure 2.16 Lift and drag calibration method.

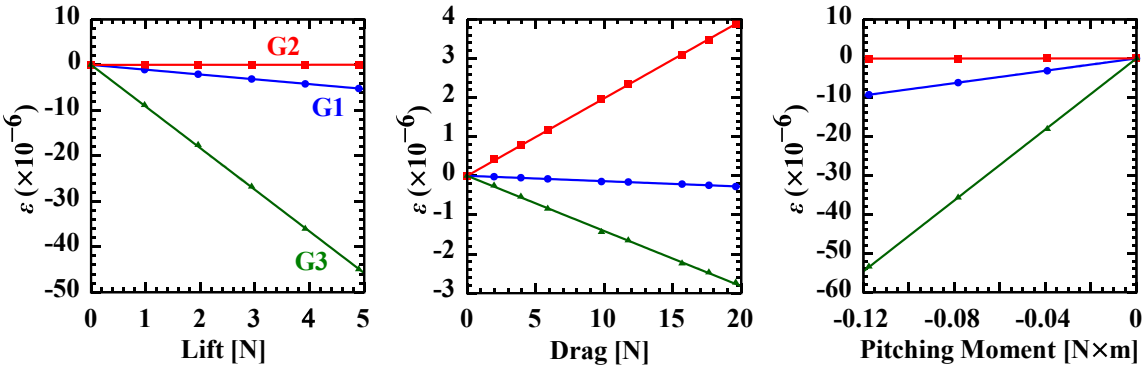

Figure 2.17 Results of the calibration force applied independently.

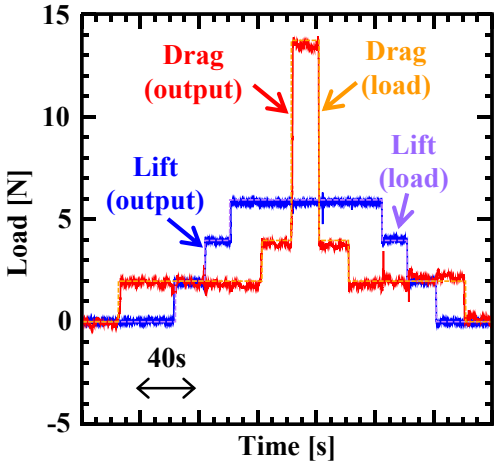

Figure 2.18 Time history of the loaded lift, drag, and measured force. Solid lines are the measured force, and dashed lines are the loaded force.

2.2.4.4. Wind Tunnel Testing

The measurement accuracy of the ring force balance was examined in a supersonic wind tunnel. A blunt body is used for the measurement validation. The schematic illustration is shown in Fig. 2.19. The clearance between the model and housing is set the order to 0.5 mm. The ring force balance is installed in the housing behind the model. The pressure in housing and the temperature of the balance are measured and the pressure compensation of the model aft-surface and the temperature compensation described in Section 2.2.4.2 are considered.

An experimental result of the force measurement is shown in Fig. 2.20. The dashed line in this figure shows the drag measured by piston balance system using a load cell[40]. From this figure, the drag measured by the ring force balance agrees with the drag measured by the piston balance system. Additionally, the lift force is suppressed during wind tunnel running. Hence, the fabricated ring force balance system is satisfied the requirement for the wind tunnel with small test section.

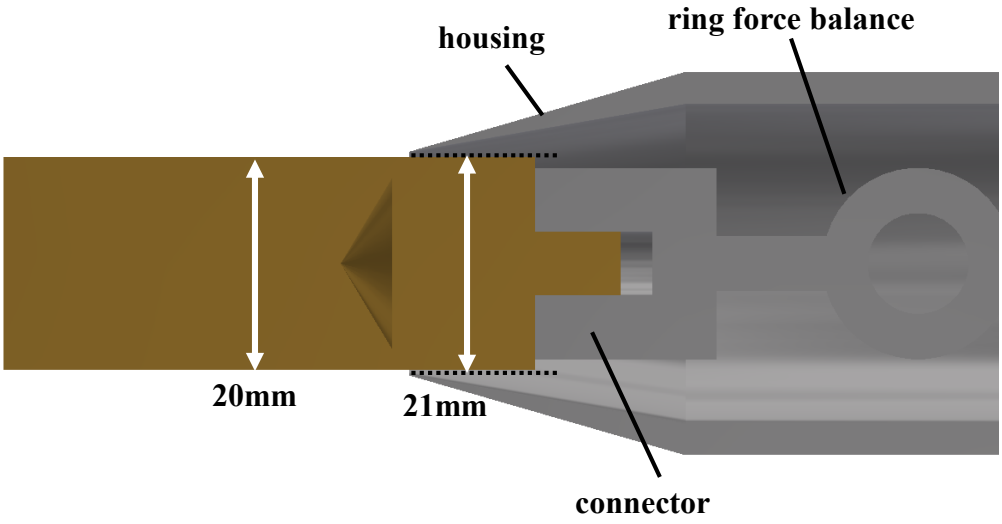

Figure 2.19 Schematic illustration of the drag measurement using ring force balance.

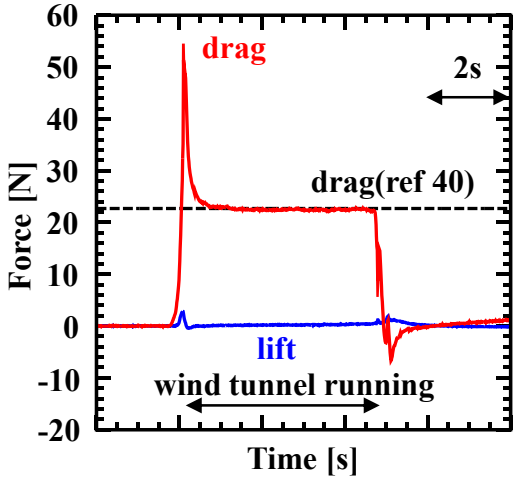

Figure 2.20 Time history of the force measurement during wind tunnel testing.

2.3 Numerical Method

The flow field is computed two-dimensional axisymmetric Navier-Stokes Equations written as

$$\frac{\partial \boldsymbol{Q}}{\partial t}+\frac{\partial \boldsymbol{E}}{\partial z}+\frac{\partial \boldsymbol{F}}{\partial r}+\frac{\boldsymbol{H}}{r}=\boldsymbol{W}\ . \tag{2.57}$$

Here, z and r are the axial direction and the radial direction coordinates, respectively. $\boldsymbol{Q}$ is the vector of conservative variables. $\boldsymbol{E}$ and $\boldsymbol{F}$ are the flux vectors and $\boldsymbol{H}$ is the vector that comes from the axisymmetric formulation given as following Eq. (2.58).

$$\boldsymbol{Q}=\begin{pmatrix}\rho\\ \rho u_z\\ \rho u_r\\ e\end{pmatrix},\quad \boldsymbol{E}=\begin{pmatrix}\rho u_z\\ p+\rho u_z^2-\tau_{xx}\\ \rho u_z u_r-\tau_{xy}\\ (e+p)u_z-(\tau_{xx}u_z+\tau_{xy}u_r+kT_x)\end{pmatrix},$$

$$\boldsymbol{F}=\begin{pmatrix}\rho u_r\\ \rho u_z u_r-\tau_{yx}\\ p+\rho u_r^2-\tau_{yy}\\ (e+p)u_r-(\tau_{yx}u_z+\tau_{yy}u_r+kT_y)\end{pmatrix}, \tag{2.58}$$

$$\boldsymbol{H}=\begin{pmatrix}\rho u_r\\ \rho u_z u_r-\tau_{xy}\\ \rho u_r^2-2\mu\left(\dfrac{\partial u_r}{\partial r}-\dfrac{u_r}{r}\right)\\ (e+p)u_r-(\tau_{yx}u_z+\tau_{yy}u_r+kT_y)\end{pmatrix}.$$

Where

$$\begin{cases}\tau_{xx}=\dfrac{1}{3}\mu\left(4\dfrac{\partial u_z}{\partial z}-2\dfrac{\partial u_r}{\partial r}\right)\\ \tau_{xy}=\tau_{yx}=\mu\left(\dfrac{\partial u_z}{\partial z}+\dfrac{\partial u_r}{\partial r}\right)\\ \tau_{yy}=\dfrac{1}{3}\mu\left(-2\dfrac{\partial u_z}{\partial z}+4\dfrac{\partial u_r}{\partial r}\right)\end{cases} \tag{2.59}$$

and

$$c_p T = \frac{(e+p)}{\rho} - \frac{(u_z^2 - u_r^2)}{2}, \quad p = (\gamma - 1)\left(e - p \times \frac{u_z^2 - u_r^2}{2} \right). \tag{2.60}$$

$\boldsymbol{W}$ in Eq. (2.57) is the energy source term written as

$$\boldsymbol{W} = \begin{pmatrix} 0 \\ 0 \\ 0 \\ P_a \end{pmatrix}. \tag{2.61}$$

In this study, the conservation equations for a two-dimensional axisymmetric flow over a flat-head, circular cylinder are solved. The flow-field is assumed to be calorically-perfect and viscous. The mass, momentum and energy conservation equations are discretized using a finite volume method. The numerical flux function is evaluated using the AUSM-DV scheme.[46,47] The MUSCL approach[48,49] is employed with a minmod limiter and computed flow properties are second-order accurate in space. The viscosity and the thermal conductivity are estimated using Sutherland's law. The discretized equations are numerically integrated in time using a second-order Runge-Kutta method. Before calculating an unsteady flow simulation with energy deposition, a corresponding steady-state solution without energy deposition is numerically integrated in time using the LU-SGS implicit method.[50] This steady-state solution is employed as the initial condition of the unsteady simulation.

The Mach number, the static pressure and the temperature of the free stream is set to 1.94, 13.7 kPa and 162.6 K, respectively. These values refer to the condition of the experiment. An adiabatic wall condition is imposed at the surface of the flat-head body. For the calculated cases in this study, the effect of the heat transfer to the wall on the computed drag over the frontal surface of the body should be small because the low-density bubble does not attach to the surface of the flat-head body.[35] Moreover, the experimental shape of the bow shock wave over the model is numerically reproduced without accounting for viscous effects.[40,51]

A laser heating source for an energy deposition is assumed to have a Gaussian spatial distribution.[30,52]

$$P_{\mathrm{a}}(z,r,t) = \lambda(t) q_0 \exp\left[-\frac{(z-z_0)^2 + r^2}{r_0^2}\right] \tag{2.62}$$

$$\lambda(t) = \begin{cases} 1, 0 \le \mathrm{mod}(t, \dfrac{1}{f}) \le \tau \\ 0, \tau < \mathrm{mod}(t, \dfrac{1}{f}) < \dfrac{1}{f} \end{cases} \tag{2.63}$$

The value of q_0 is given by the following relationship.

$$q_0 = \frac{\eta_a E}{\tau \displaystyle\int_{V_0} \exp\left[-\frac{(z-z_0)^2 + r^2}{r_0^2}\right] dV} \tag{2.64}$$

where z_0 is

$$z_0 = s - s_{\mathrm{model}} \tag{2.65}$$

In this simulation, $s = 2 \times d_{\mathrm{model}}$. Absorption efficiency η_{a} and laser heating area radius r_0 are used as the control parameters for energy deposition. These values are determined by fitting experimental results of the temporal pressure history at the centerline of the model, as will be explained in the following.

Chapter

3

Drag Reduction Mechanisms over Blunt Body

3.1 Flow Condition without Energy Deposition

The computed domain is shown in Fig. 3.1. A steady-state solution is calculated using the LU-SGS implicit method and the solution was calculated by both viscous and inviscid flows for comparison of the effect of the viscosity to the vortex ring behavior. Calculated results are mainly presented using 201×201 computational grid points. Calculations are additionally made with 301×201 and 401×201 grid points, respectively, to examine the sensitivity of the grid size and the time step to the calculated results. The difference of the computed drag value without energy deposition among the three grid systems is within 0.05% and the one with energy deposition is within 0.18%. Thus, the impact of the grid size on the computed solutions is believed to be negligibly small.

Figure 3.2 shows a snapshot of Schlieren image obtained by experiment. From the experimental results, the drag, stagnation point pressure and shock stand-off distance are 20.94 ± 1.06 N, 73.7 kPa and 9.02 ± 0.29 mm, respectively. The errors of the drag is evaluated by the repeatability, and the error of the shock stand-off distance is evaluated by

the finite thickness of the Schlieren image. Figures 3.3 - 3.5 show numerical Schlieren images, and pressure contours and density contours obtained by calculations. Although the result of the inviscid calculation exhibits a difference at the downstream flow structure, the overall flow structure obtained by calculations agrees well with the experimental results: the bow shock wave profile, the shock stand-off distance, the expansion wave and the separated flow at downstream. The drag, stagnation point pressure and shock stand-off distance are also calculated; the values obtained by viscous calculation are 20.82 N, 73.05 kPa and 9.01 ± 0.31 mm; the values obtained by inviscid calculation are 20.84 N, 73.03 kPa and 8.98 ± 0.22 mm, respectively. Comparison of the experimental and calculated results are shown in Table 3.1. These values also agree well with the experimental results. In the following calculation, these flow fields are used as initial conditions.

Table 3.1 Comparison of the experimental and calculated results.

	Experiment	Calculation	
		Viscous	Inviscid
Drag [N]	20.94 ± 1.06	20.84	20.82
Stagnation point pressure [kPa]	73.7	73.03	73.05
Shock stand-off distance [mm]	9.02 ± 0.29	9.01 ± 0.31	8.98 ± 0.22

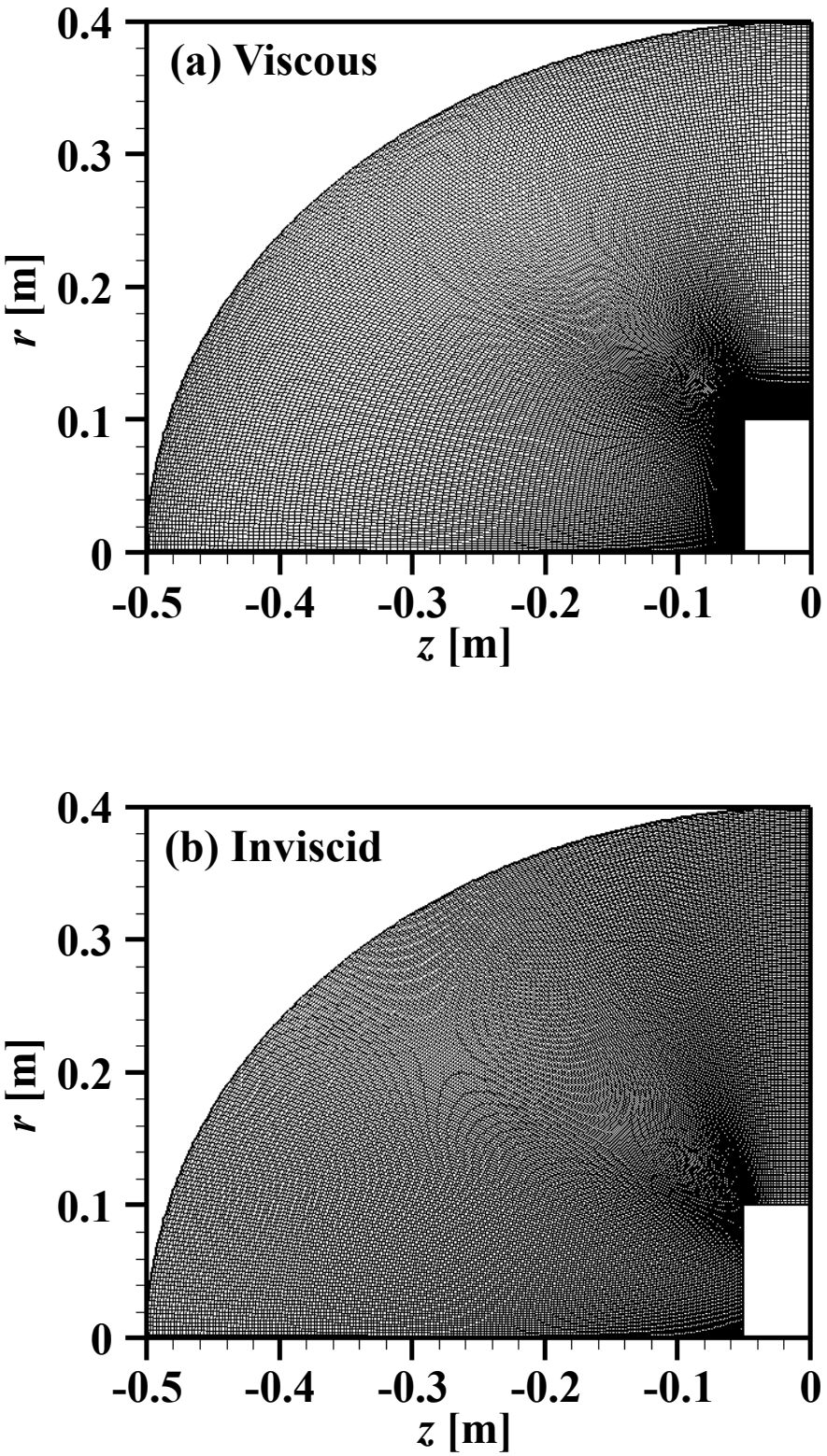

Figure 3.1 The calculated grid of 201 × 201: (a) viscous calculation domain, (b) inviscid calculation domain.

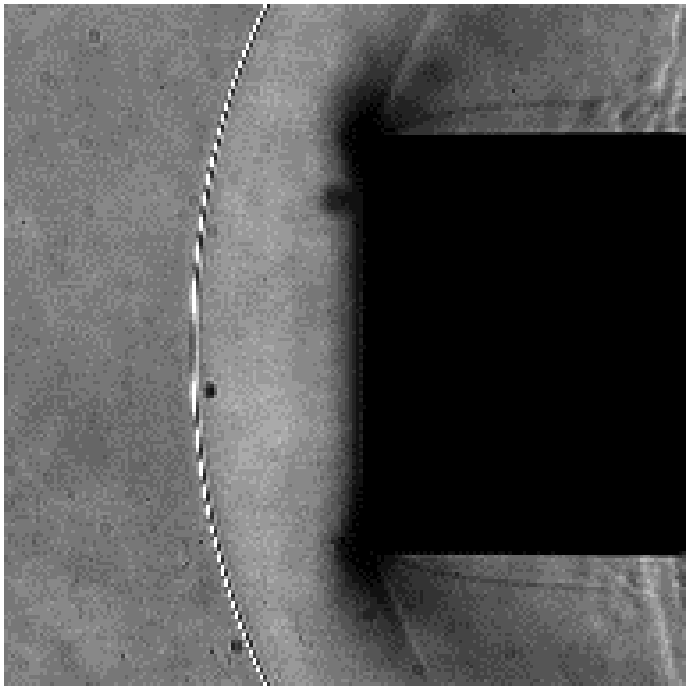

Figure 3.2 Instant Schlieren image without energy deposition obtained by experiment.

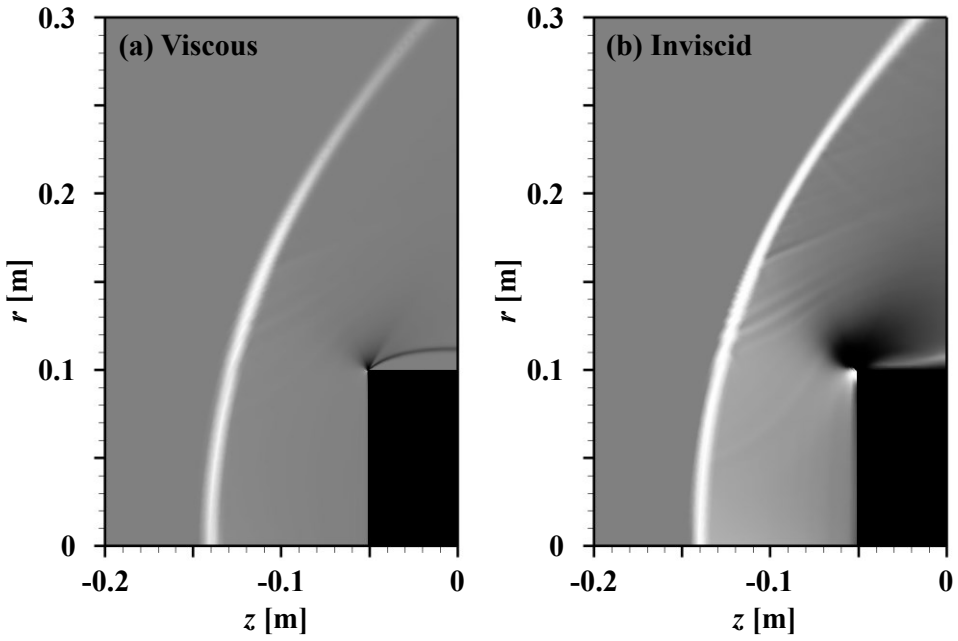

Figure 3.3 Numerical Schlieren image obtained by calculation: (a) viscous case, (b) inviscid case.

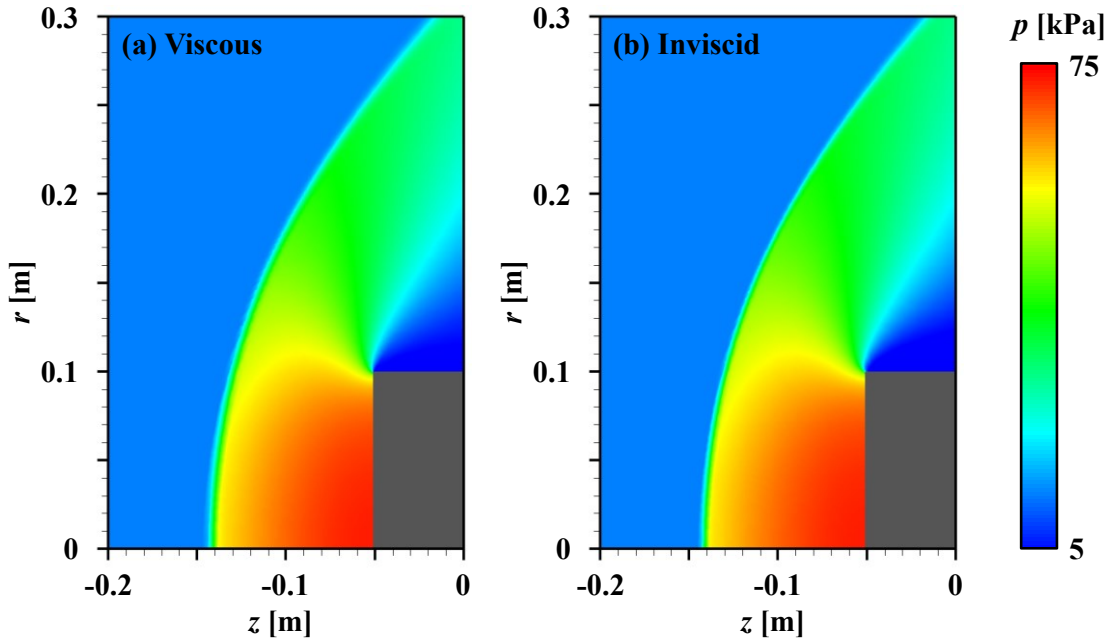

Figure 3.4 Pressure distribution obtained by calculation: (a) viscous case, (b) inviscid case.

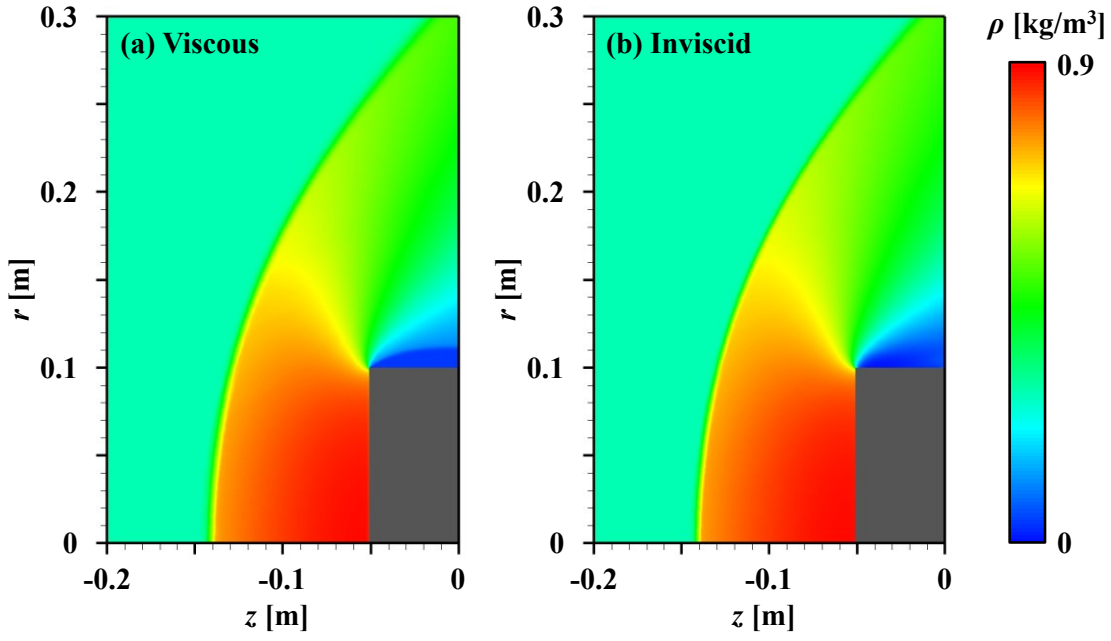

Figure 3.5 Density distribution obtained by calculation: (a) viscous case, (b) inviscid case.

3.2 Estimation of Effective Values in Energy Deposition

In order to simulate an energy deposition into the free stream flow, there are two parameters, r_0 and η_a in Eq. (2.64) which cannot be determined a prioi. A set of the values are determined by fitting the calculated pressure history at the centerline on the model to the measured one. The experimental conditions of the reference experiment are E = 6.6 mJ/pulse and f = 2 kHz. As will be shown later, based on the measured pressure time history for this relatively lower repetition frequency, the interaction between the successive energy depositions is weak. Thus, the measured pressure time history in-between two successive energy depositions is used to calibrate the amount of the energy effectively deposited into the flow in a single energy deposition.

Calculations are carried out using several sets of r_0 and η_a. The calculated values are shown in Table 3.2. A time step is set to a constant value of 1 ns, which is approximately one-tenth the nominal laser pulse duration (corresponding to the CFL number of 0.035) in the unsteady simulation. This time step is sufficiently small to simulate the measured vortex ring behavior; calculation shows reasonable agreement with the experiment for the conditions analyzed in the present study. The stagnation point pressure histories obtained by experiments are shown in Fig. 3.6. The dependences of the centerline pressure history with E = 13.2 mJ/pulse on η_a and r_0 are shown in Figs. 3.7 and 3.8, respectively. The dependences of the centerline pressure history with E = 6.6 mJ/pulse on η_a and r_0 are shown in Figs. 3.9 and 3.10, respectively. The minimum peak value and the duration of the negative overpressure period are used as criteria. The peak value decreases with η_a increasing and as r_0 is reduced and the duration becomes longer with η_a decreasing. In the case of viscous flow, the combination of η_a = 0.4 and r_0 = 1.0 mm yields a reasonable agreement with the measurement. These values do not depend on the pulse energy. In contrast, a reasonable

combination for inviscid flow calculation depends on the pulse energy. Additionally, the duration of the negative overpressure period, which can be related to the vortex ring behavior, is affected by the pulse energy. Therefore, viscous flow calculation and the combination of $\eta_a = 0.4$ and $r_0 = 1.0$ mm were employed. In this case, the densities of the low-density bubble are 0.10 kg/m^3 and 0.07 kg/m^3 for $E = 6.6$ mJ/pulse and 13.2 mJ/pulse respectively. If the pressure of the bubbles is the same as the initial pressure, the densities can be evaluated using the thermodynamics phenomena as described in Section 1.3. From the results of the evaluation, the densities of the bubbles are 0.096 kg/m^3 and 0.063 kg/m^3 for $E = 6.6$ mJ/pulse and 13.2 mJ/pulse respectively. Additionally, the size of the bubble detected by Schlieren image is about 4.0 mm and its size obtained by the simulations is in range of 4.0 to 5.0 mm. Hence, the determined parameters, $\eta_a = 0.4$ and $r_0 = 1.0$ mm, agree with the experiment.

In the following simulations, thermochemical non-equilibrium effects for air are not accounted for. Such effects will be less sensitive to the calculated drag performance because the temperature of the low-density bubble created by energy deposition is decreased to be approximately 400 K at most near the shock wave.

Table 3.2 Parameter condition.

	E [mJ]		$\eta_a E$ [mJ]	r_0 [mm]				
	13.2	6.6		0.1	0.5	1.0	1.5	2.0
η_a	0.2	0.4	2.64		✔	✔	✔	
	0.3	0.6	3.96		✔	✔	✔	
	0.4	0.8	5.28	✔	✔	✔	✔	✔
	0.6		7.92		✔	✔	✔	
	0.8		10.6		✔	✔	✔	
	1.0		13.2		✔	✔	✔	

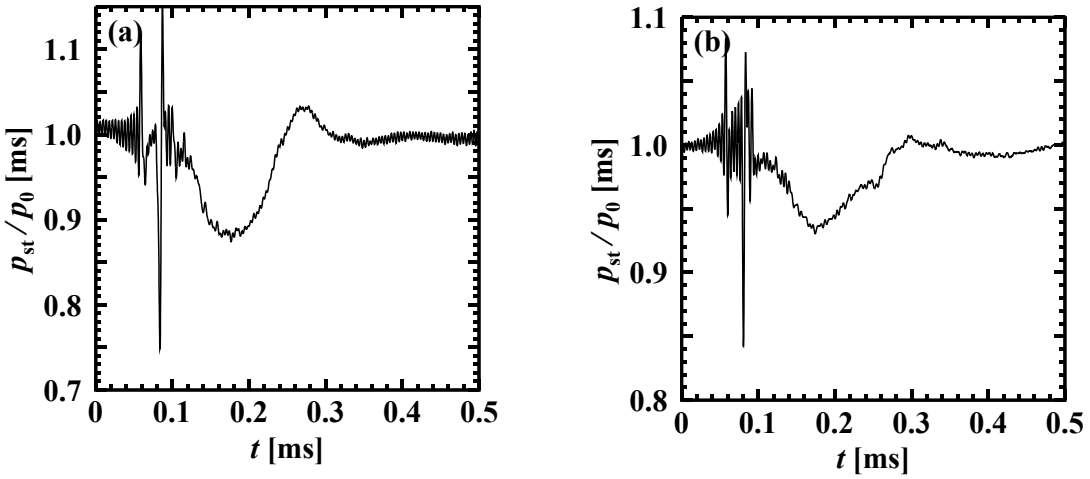

Figure 3.6 Stagnation point pressure obtained by experiment; (a) E = 13.2mJ/pulse, (b) E = 6.6 mJ/pulse.

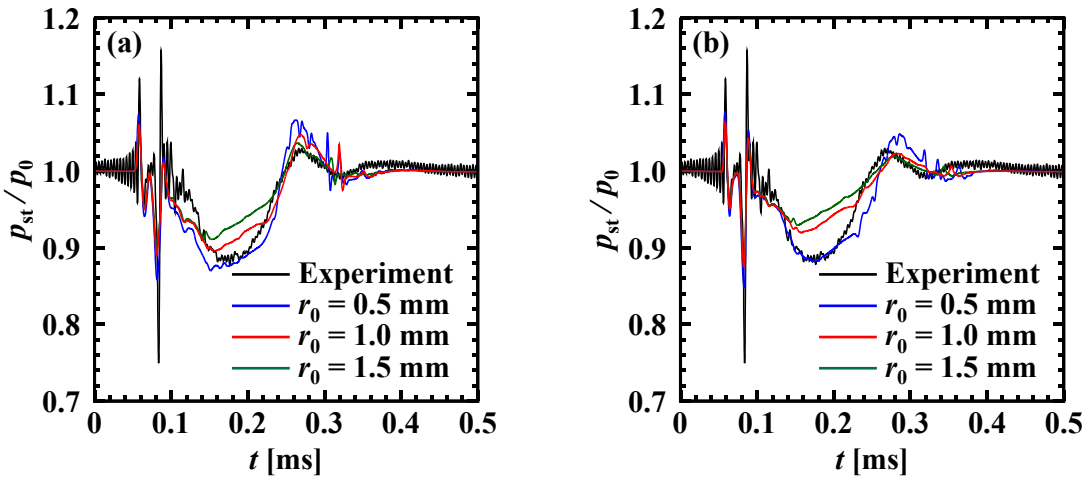

Figure 3.7 Energy input volume dependence of stagnation point pressure; E = 13.2 mJ/pulse; (a) viscous case, (b) inviscid case.

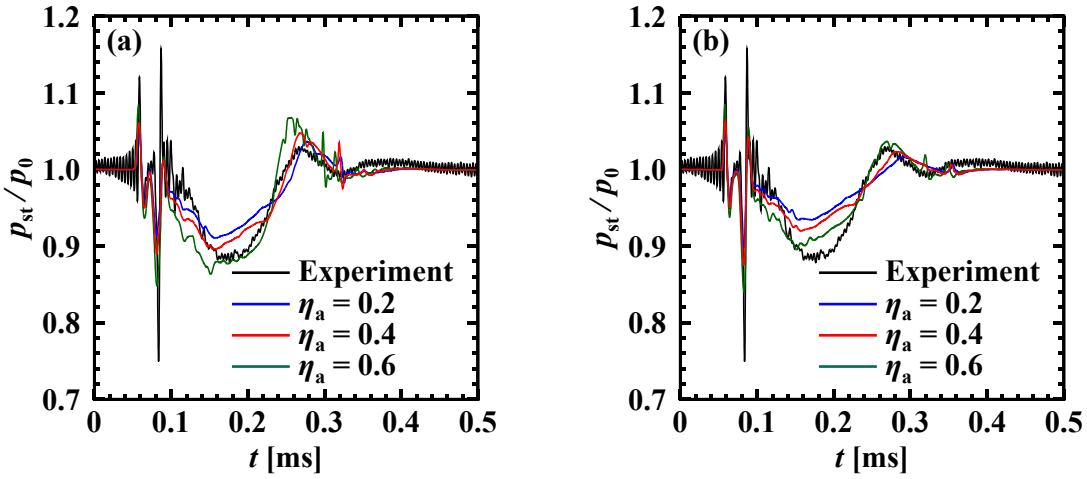

Figure 3.8 Effective input energy dependence of stagnation point pressure; E = 13.2 mJ/pulse; (a) viscous case, (b) inviscid case.

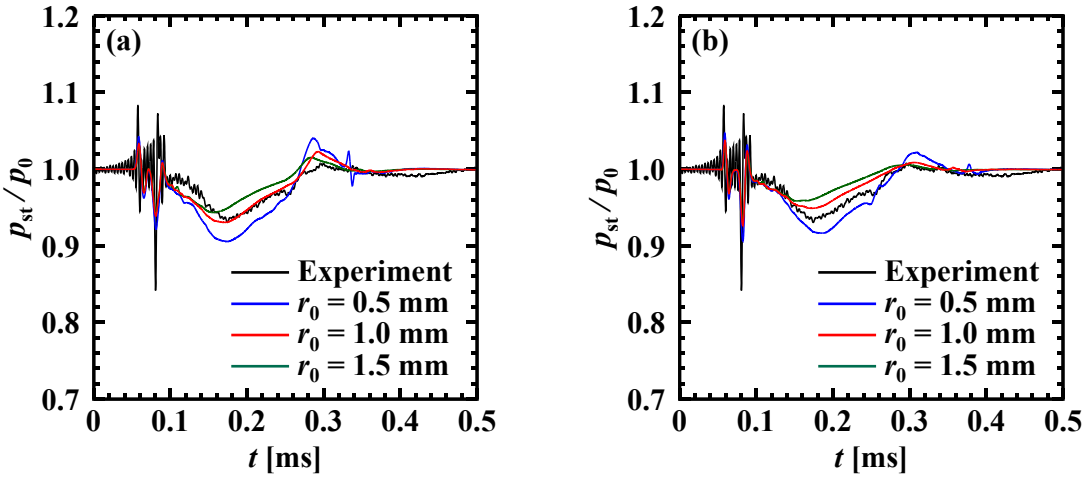

Figure 3.9 Energy input volume dependence of stagnation point pressure; E = 6.6 mJ/pulse; (a) viscous case, (b) inviscid case.

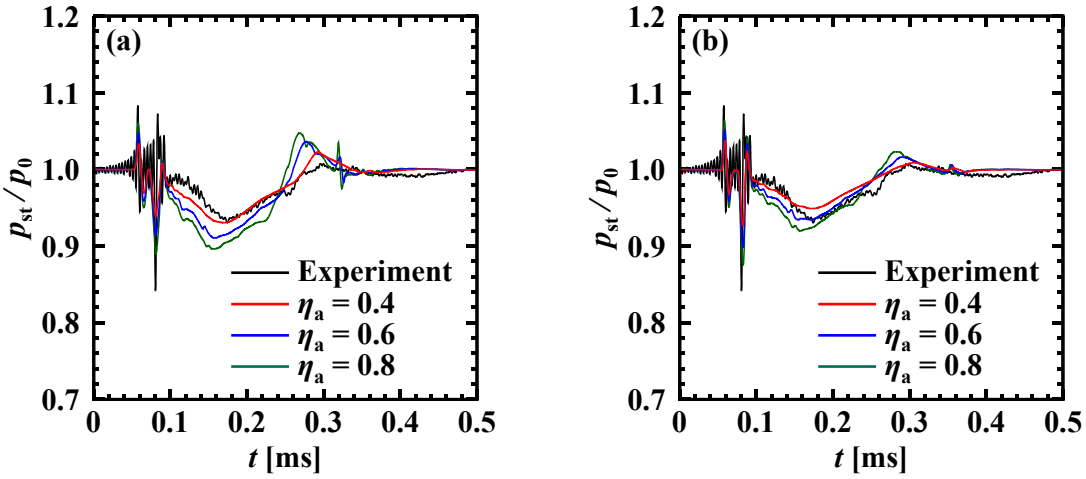

Figure 3.10 Effective input energy dependence of stagnation point pressure; E = 6.6 mJ/pulse; (a) viscous case, (b) inviscid case.

3.3 Flow Induced by Single Energy Deposition

Schlieren photographs taken in the experiment,[21] numerical Schlieren pictures, density contours, differential density contours, pressure contours and calculated differential pressure contours are shown in Fig. 3.11. The temporal profile of the stagnation pressure is shown in Fig. 3.12. The labels in Fig. 3.11 correspond to those in Fig. 3.12. In the following, the time shown in Figs. 3.11 and 3.12 denotes the time elapsed after a given laser pulse irradiation. Figure 3.11 (a) displays the moment when the blast wave arrives at the flat-head of the model and the low density bubble is entering the shock layer. One can recognize from Fig. 3.12 (a) that the pressure value becomes a sharp peak which is caused by the blast wave arriving. The extrusion of the shock wave near the centerline of the model, which is referred to as the lens effect,[31,52] which is the bow shock distortion due to decrease in local Mach number, is observed in Fig. 3.11 (b). This phenomenon leads to the decrease of the pressure in the shock layer; the undershoot in the pressure history shown as in Fig. 3.12 (b) represents the instantaneous flow-field in which the low pressure region behind the original blast wave reaches the model surface. When the bubble is passing through the shock wave, the vortex ring is induced by the baroclinic effect,[31] as seen from Fig. 3.11 (c). At nearly the same time, the centerline pressure value returns to the initial pressure as the region between the blast wave and low-density bubble reaches the wall. The peak pressure observed in Fig. 3.12 (d) and (e) are caused by the lens effect. Figure 3.12 (d) displays the instant when the expansion wave generated by the extrusion of the shock wave arrives at the model. Figure 3.12 (e) denotes the moment when the compression waves are generated and the end of lens effect arrives.

The unsteady behavior of the vortex ring in the shock layer is shown in Fig. 3.11 (d) to (g). The corresponding centerline pressure values are given in (d) to (g) in Fig. 3.12. When

the thickness of the shock layer near the centerline is increased as a result of the lens effects, a second undershoot is observed in the pressure history; after the second undershoot in the pressure history, the pressure returns almost to its initial value without energy deposition (e), when the baroclinic vortex moves toward the surface of the flat-head model, the pressure decreases gradually leading to the primary reduction of the drag impulse of the model because the pressure in the vortex ring is lower than the static pressure in the shock layer ((e) to (g)). Especially, a large drag reduction was obtained between (f) to (g).

In Fig. 3.11 (g), the vortex ring has passed through downstream, and the shock layer is compressed in this state. At this moment, the centerline pressure returns the initial one, as seen in Fig. 3.12 (g). Finally, after the shock layer thickness is slightly overshot, the shock layer recovers to its initial state without energy deposition, as shown in Fig. 3.11 (h).

It should be noted that the drag over the frontal surface of the body reduces when the baroclinic vortex ring is moving in the shock layer. In this way, the temporal profile of centerline pressure can be related to the vortex ring behavior.

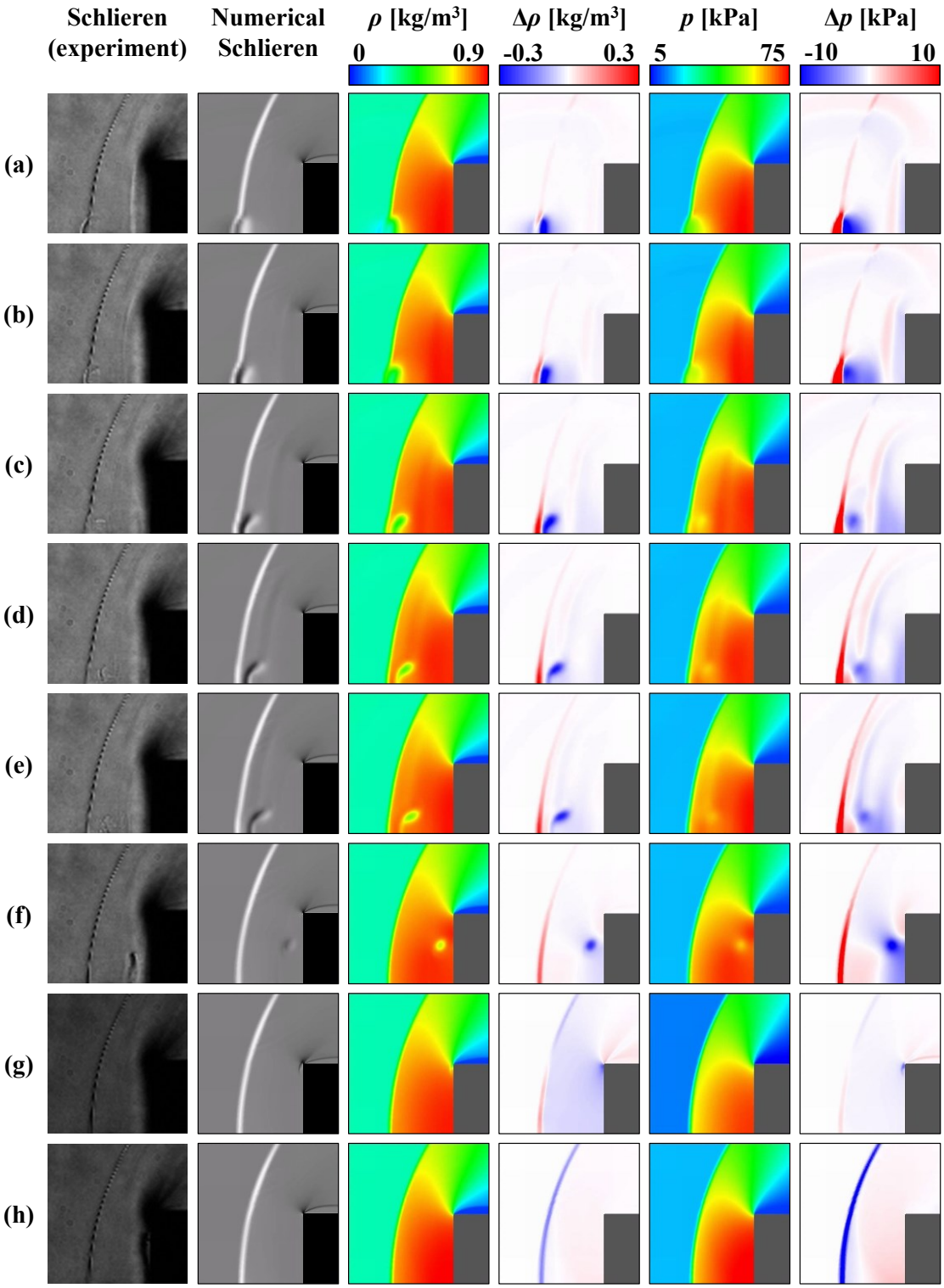

Figure 3.11 Development of flow-field after a single laser pulse energy deposition. Experimental Schlieren (f = 2 kHz); Numerical Schlieren picture; Density distribution; Differential density distribution; Pressure distribution; Differential pressure distribution.

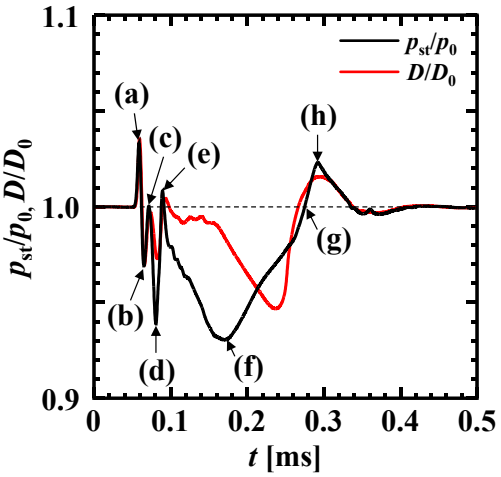

Figure 3.12 Temporal variation of stagnation point pressure and drag obtained for the case with $\eta_a = 0.4$ and $r_0 = 1.0$ mm.

3.4 Repetitive Pulse Energy Depositions over Flat Head

3.4.1 Vortex Ring Behavior

Calculations are carried out for the case of repetitive energy depositions with the value of r_0 and η_a unchanged: η_a = 0.4 and r_0 = 1.0 mm. The repetition frequency and laser energy per pulse are varied: f = 2 to 100 kHz and E = 5.0, 6.2 mJ/pulse. Under these conditions, the successive energy depositions do not interact each other because the repetition interval is 8μs (125 kHz) under the condition with the flow speed of 500 m/s and the low-density bubble radius of 4.0 mm. The time-averaged pressure distributions over the model are shown in Figs. 3.13 and 3.14. Time-averaged Schlieren and the calculated density and pressure contours are given in Fig. 3.15.The time-averaged shock stand-off distance is shown in Fig. 3.16. In this figure, the error-bar of the experiment includes time variation and measurement error due to the image resolution, and the one of the CFD indicates time variation. The cause of the discrepancy between experiment and calculation is the miss shot, laser irradiation without breakdown. For higher frequency of experiment, the shock stand-off distance sometimes decreases because the breakdown does not occur. The residence time of the vortex ring τ_{vortex} and the number of vortex rings in the shock layer N_{vortex} are shown in Figs. 3.17 and 3.18, respectively. The value of τ_{vortex} is defined as the time interval from the extrusion of the shock wave shown in Fig. 3.11 (a) to the time the vortex ring passes through downstream shown in Fig. 3.11 (g). The residence time obtained by calculation and experiment has discrepancy. The cause of this difference is the difficulty to define the accurate time by Schlieren images. The value of N_{vortex} is calculated as follows.

$$N_{vortex} = f \times t_{vortex} \tag{3.1}$$

It should be noted that all calculated results shown in Figs. 3.13 to 3.18 are shown as a time-averaged value over 0.5 ms and the measured results shown in Figs. 3.17 and 3.18 are deduced from the Schlieren images. As shown in Figs.3.17 and 3.18, the frequency dependence of the residence time and the number of vortex rings has a similar tendency for each data for the conditions shown.

Based on the calculated results given from Figs. 3.13 to 3.19, the obtained flow-field over the body can be classified into three regimes. We focus on the flow-field state and vortex ring motions for this classification.

At the lower frequencies below approximately 5 kHz, the residence time is a roughly constant value of 190 μs, which is nearly the same for the case of a single pulse. This result indicates that the number of vortex rings in the shock layer is less than one because the repetitive frequency of 5 kHz means that the interval of energy added equals 200 μs. Therefore, the interaction between given two successive vortex rings is weak for these lower frequency conditions.

At the middle frequencies from 5 to 15 kHz, the residence time monotonically decreases as the frequency increases, as shown in Fig. 3.17. For this condition, two successive vortex rings are included in the shock layer at most. From Figs. 3.13 and 3.14, the pressure value is still highest at the center of the model. From Fig. 3.18, one or two vortex rings exist in the shock layer. Under these frequencies, the interaction among the successive vortex rings starts, although it may be still weak.

At the higher frequency conditions above 15 kHz, the number of vortex rings within the shock layer is more than two as is shown in Fig. 3.18. From Figs. 3.13 and 3.14, the pressure distribution over the model is kept nearly constant in the region close to the model center. One can see from Fig. 3.15 that a quasi-stationary vortex ring in the shock layer appears at

these frequencies and that the shape of the shock wave is deformed obliquely. Therefore, by increasing the pulse repetition frequency, the flow velocity behind the shock wave is increased, thereby decreasing the residence time of the vortex rings. As a result, the number of vortex rings in the shock layer is saturated.

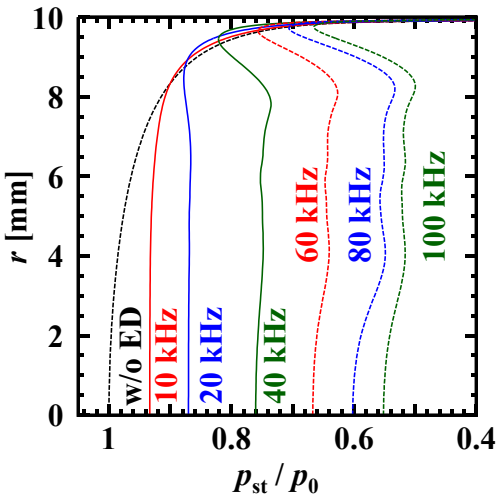

Figure 3.13 Time-averaged pressure profile of model surface obtained from simulation of E = 5.0 mJ/pulse.

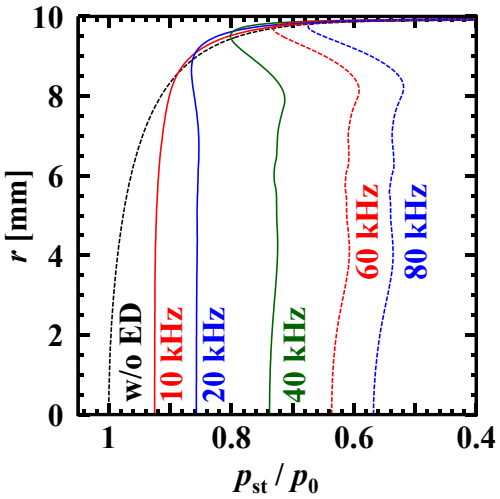

Figure 3.14 Time-averaged pressure profile of model surface obtained from simulation of E = 6.2 mJ/pulse.

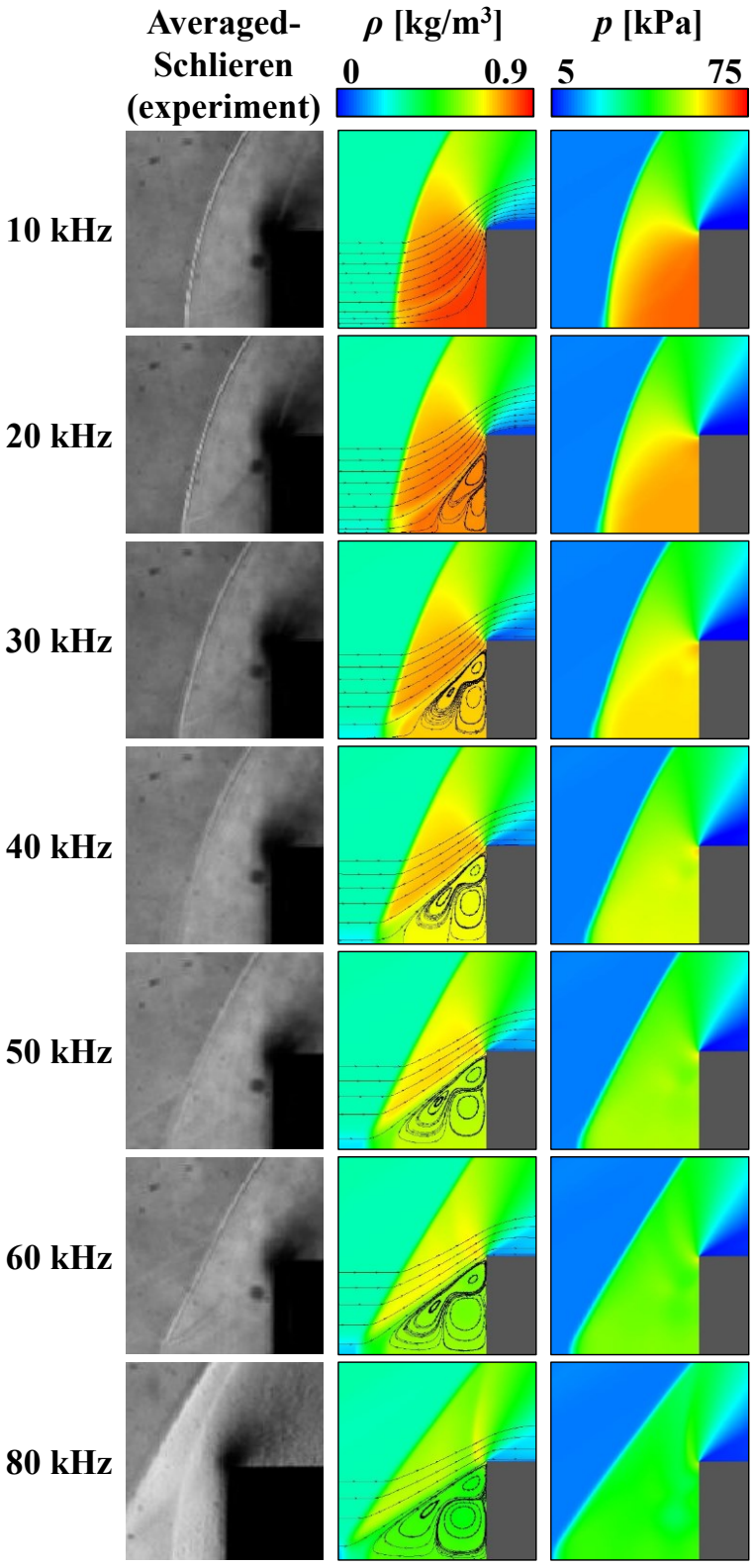

Figure 3.15 Time averaged Schlieren images, calculated density contours and streamlines and pressure contours of E = 5.0 mJ.

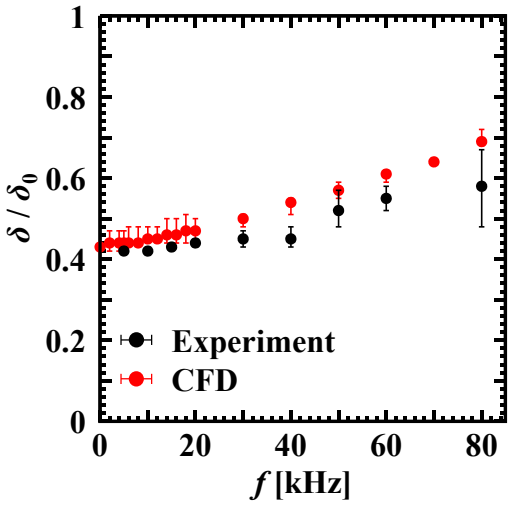

Figure 3.16 Frequency dependence of shock stand-off distance.

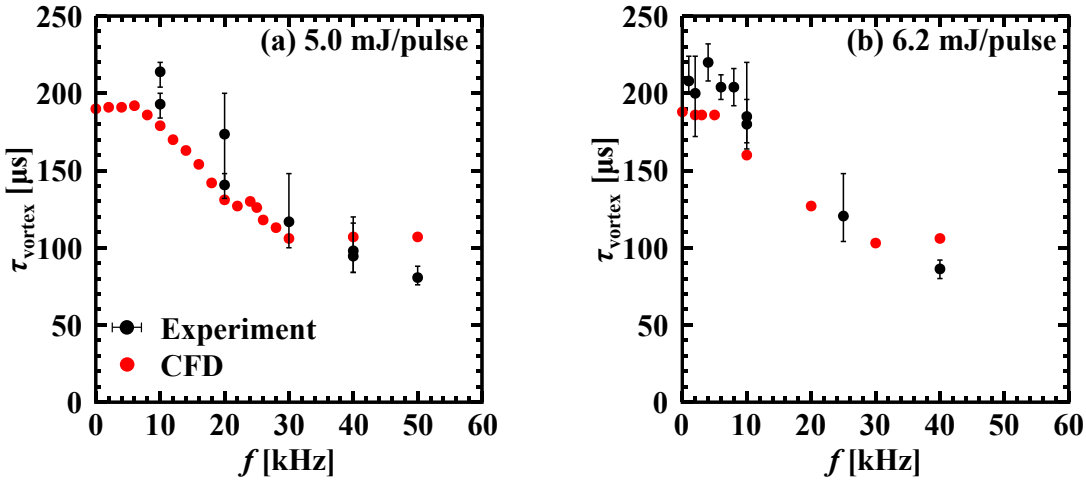

Figure 3.17 Frequency dependence of vortex ring residence time in shock layer. In this figure, 0 kHz means the result of single pulse.

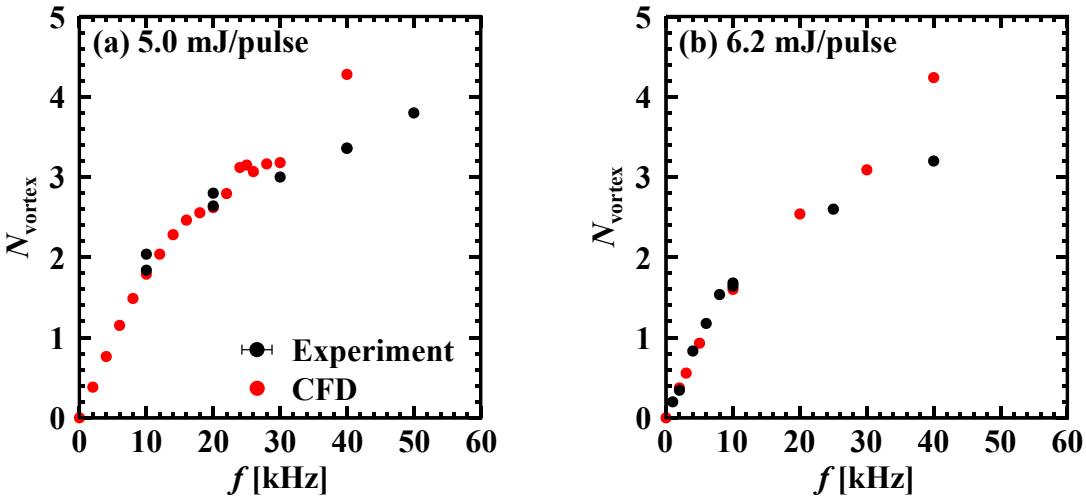

Figure 3.18 Frequency dependence of the number of vortex rings in the shock layer. The number is a time-averaged value over 0.5 ms.

3.4.2 Drag Reduction Performance

The calculated temporal history of the pressure at the centerline of the model is compared with measurement for the cases of f = 10 to 60 kHz. The results are presented in Fig. 3.19. The averaged pressure at the centerline is shown in Fig. 3.20. In this figure, the error-bar means the time variation of the pressure. The amount of the calculated drag reduction with energy deposition is compared similarly in Fig. 3.21. The drag reduction is normalized by the drag value without energy deposition. It should be noted that the drag value given in Fig. 3.21 is a time-averaged value over 0.5 ms at the interval in a quasi-steady state condition.

From Fig. 3.21, the drag reduction performance of the experiment has an increasing tendency with the repetition frequency increasing and the calculation result has similar tendency to the experiment. These results are consistent with the past investigations[20,21,32,33] of the drag reduction performance: drag reduction magnitude is increased as the repetition frequency increases. In addition, the calculated temporal history of the pressure also agrees with the measured one both qualitatively and quantitatively below 10 kHz, as seen in Fig. 3.19. On the other hand, for the higher frequency conditions, there are discrepancies between the measured and calculated drag reduction and time averaged pressure; the difference of the drag reduction increases with the repetitive frequency. A possible reason for the discrepancy may be due to a three-dimensional effect over an energy deposited flow-field neglected in the present calculation. A non-axisymmetric motion of the vortex ring is experimentally observed at the frequency conditions from 10 to 60 kHz.[37] Such a non-axisymmetric motion of the vortex ring might modify the effective shock stand-off distance and the pressure distribution over the model surface. In order to examine such an effect, a three-dimensional calculation is required, but is out of the scope of this study.

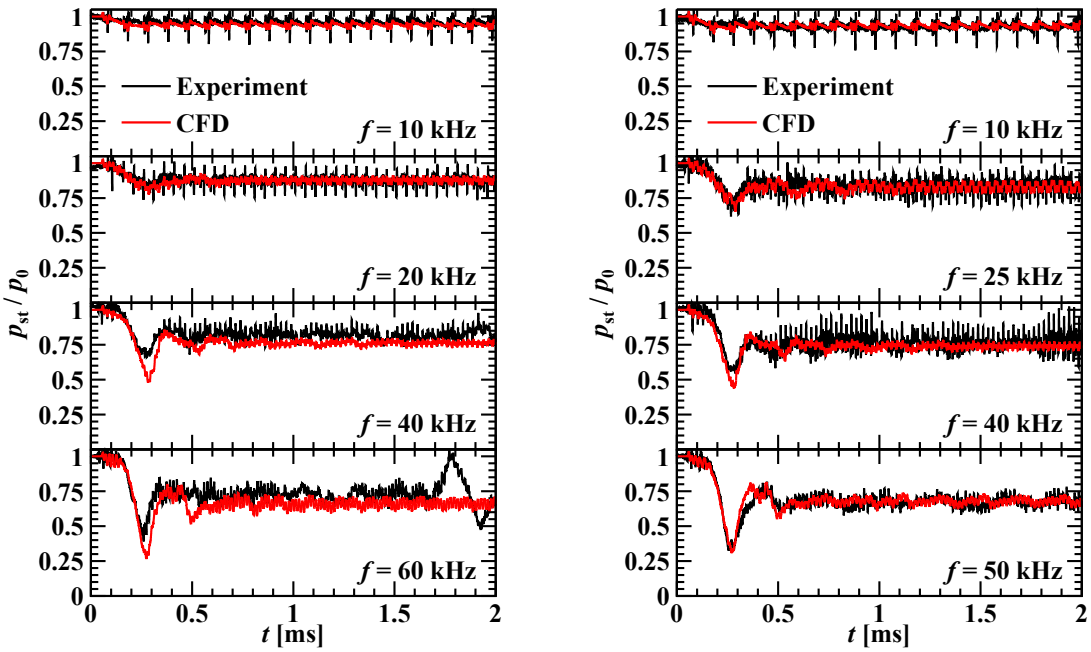

(a) E = 5.0 mJ/pulse (b) E = 6.2 mJ/pulse

Figure 3.19 Time history of centerline pressure obtained from experiment and simulation.

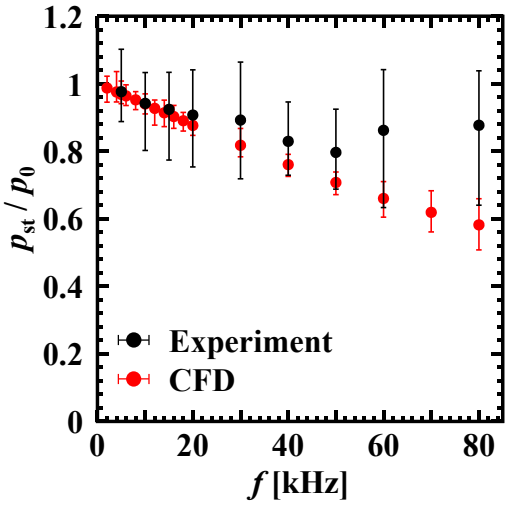

Figure 3.20 Frequency dependence of the stagnation point pressure. Error-bars correspond to the time variation of the pressure.

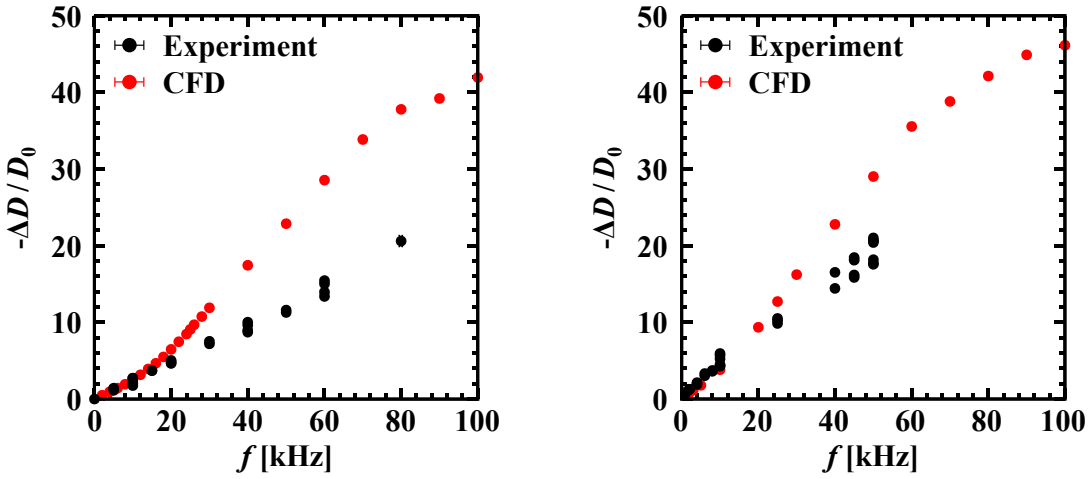

(a) E = 5.0 mJ/pulse (b) E = 6.2 mJ/pulse

Figure 3.21 Frequency dependence of drag reduction. (a) E = 4.7 - 5.0 mJ/pulse of experiment; E = 5.0 mJ/pulse of calculation; (b) E = 6.2 - 6.6 mJ/pulse of experiment; E = 6.2 mJ/pulse of calculation.

3.5 Summary of This Chapter

In this chapter, the drag reduction over a blunt body using energy depositions is simulated and the vortex ring behavior is related to the drag reduction mechanisms.

- The results of steady state flow obtained by calculations agree well with the experimental results, for the flow field, drag stagnation point pressure and shock stand-off distance.
- For the unsteady energy deposition calculation, the effectively deposited energy ratio and radius of the deposited energy source were determined by fitting the centerline pressure history to the measured one. From the fitting results, $\eta_a = 0.4$, $r_0 = 1.0$ mm were adopted.
- From the single pulse energy deposition calculation using the determined parameters, the time history of the stagnation point pressure corresponds to the blast wave and the baroclinic vortex ring behavior that were generated by energy deposition. The drag was reduced when the vortex ring resided in the shock layer.
- Drag reduction by repetitive energy deposition can be classified by the number of the vortex rings in the shock layer.
    - Below 5 kHz, less than one vortex ring: Successive energy depositions were independent and the effect of the energy deposition can be described by the superposition of the successive energy depositions.
    - From 5 to 15 kHz, one or two vortex rings: The pulse-to-pulse interaction appeared and vortex rings always mitigate the pressure distribution in the shock layer, which shortened the residence time of vortex rings
    - Above 15 kHz, more than two vortex rings: Two successive vortex ring interactions appeared. The drag reduction performance obtained by the calculation and the experiment showed discrepancies. Especially, above 30 kHz, strong interaction among the successive vortex rings appeared because there were more than three

resident rings. A three-dimensional vortex motion should be considered because the multiple vortex rings always resided in the shock layer.

Chapter

4

Energy Deposition over Blunt Body with Conical Spike

4.1 Model Configuration

The model configuration is shown in Fig. 4.1 and the range of l_c and θ_c and the flow field state investigated experimentally and numerically are shown in Fig. 4.2. The dashed curve line in Fig. 4.2 indicates the condition at $d_c = d_0$ and $\theta_c = 90°$ which corresponds to the flat head cylinder model, and the dot-and-dashed line corresponds to the shock stand-off distance of the flat head model. In this figure, the black circles indicate the steady mode, in which the position of the shock wave is almost constant, and the flow is steady. On the other hand, white circles indicate an unsteady mode, where the shock wave oscillates and the flow is unsteady. Such shock wave oscillations were also reported in Ref. 53.

In this study, the drag reduction effect of energy deposition on the steady mode is mainly discussed because the impact of energy deposition on the unsteady mode is small: drag is not effectively reduced, and shock wave oscillation cannot be suppressed.

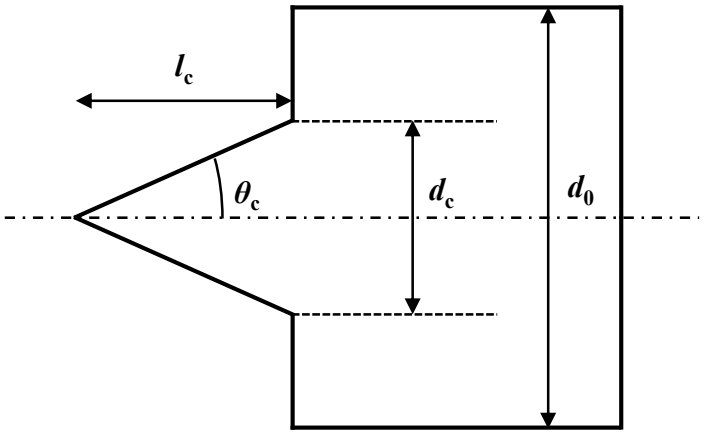

Figure 4.1 Model configuration of blunt body with a conical spike.

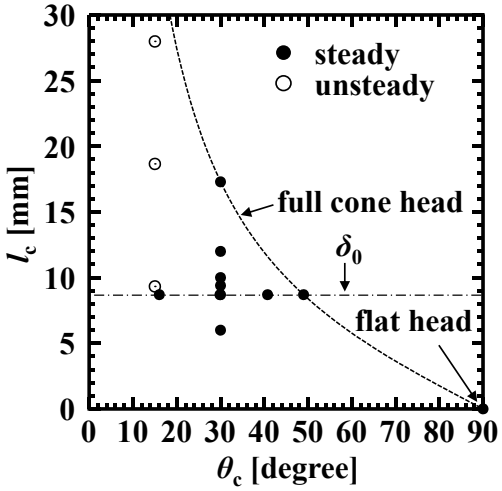

Figure 4.2 Parameter ranges of l_c and θ_c. Black circles indicate steady mode, and white circles indicate unsteady mode.

4.2 Effect of Energy Deposition on Steady Mode

4.2.1 Effect of Apex Angle of Conical Spike

The temporal history of Schlieren images, and the density and pressure distributions with the model configuration of l_c = 8.7 mm, θ_c = 30° and the energy deposition condition of E = 5.0 mJ/pulse, f = 30 kHz are shown in Fig. 4.3. From this figure, the typical flow structure of this condition can be recognized: the low density bubble generated by energy deposition passes through a shock wave (t = 0 - 12 μs); a vortex ring is generated by the baroclinic effect in the shock layer owing to the interaction between the density gradient of the low density bubble and the pressure gradient of the shock wave (t = 12 - 24 μs); the vortex ring in the shock layer moves for approximately 100 μs and flows downstream (t = 24 - 120 μs arrows in Fig. 4.3 show the same vortex ring). During this period, three or four vortex rings stay in the shock layer and these vortices mitigate the pressure field.

Time averaged Schlieren images, and time averaged density and pressure distributions with l_c = 8.7 mm, different θ_c values and without and with energy deposition of f = 30, 60 kHz are shown in Figs. 4.4, 4.5 and 4.6, respectively. From Fig. 4.4, for any θ_c value, the shape of the shock waves obtained by experiments do not have large difference; bow shocks are formed, and calculation results are qualitatively consistent with the experimental ones. From Figs. 4.5 and 4.6, the bow shock wave is deformed to the conical shock by the energy depositions. This deformation become larger with higher frequency.

The pressure value on the surface of the model is averaged in time over a period of 500 μs. The radial distributions of the pressure value are plotted in Fig. 4.7 for the case without and with energy deposition of f up to 100 kHz. The results are presented for different θ_c values. In the case of $f \leq$ 10 kHz, the distributions with the conical spike model and the blunt-

cylinder-head are different. The pressure around the central axis of the conical spike model is lower than that of the blunt body. This tendency is observed in particular for the lower frequency conditions. This decrement will be attributed to the combination of energy deposition with the conical part of the model. However, under higher-frequency conditions, the surface pressure distribution become similar to that of the blunt body. This is because the shock wave is deformed and the pressure in the shock layer is reduced as shown in Figs. 4.5 and 4.6.

The comparison of the drag performance obtained by experiment and calculation with different θ_c values as a function of f is shown in Fig. 4.8. When there is no conical spike and $\theta_c = 16.0°$, the calculation results well agree with the experimental results. In the case of $\theta_c = 30.0°$, the calculation results qualitatively agree with the experimental results, but the measured drag is lower than the calculated drag. In the experimental results, drag performances of $\theta_c = 40.9, 49.0°$ do not depend on f and are nearly constant. On the other hand, calculation results show that the drag of $\theta_c = 40.9°$ decreases with increasing f, and that the drag of $\theta_c = 49.0°$ is nearly constant when $f \leq 40$ kHz, and then decreases as f increases.

The cause of the difference of the drag value between the experiment and the calculation of $\theta_c = 30.0°, 40.9°, 49.0°$ is not known. However, in the cases of $\theta_c = 40.9°, 49.0°$, from Figs. 4.5 and 4.6, experiment shows that the center region of the shock wave is largely deformed but calculation shows that the shock wave is deformed over the entire region. This difference of the shock wave deformation is reflected in the pressure distribution in the shock layer. The pressure drag of the calculation is smaller than the experiment because the shock wave deformation of the calculation is larger than that of the experiment. Hence, the drag obtained by experiment and calculation might be different. On the other hand, the shape of

the shock wave and the shock stand-off distance of $\theta_c = 30.0°$ do not show a large difference between experiment and calculation, and the cause of this difference is still unknown.

From these results, the combination of the conical spike and the energy deposition method is effective in reducing the drag under lower-frequency conditions, but under higher-frequency conditions the effect of the conical spike become small because the effect of the energy deposition become stronger.

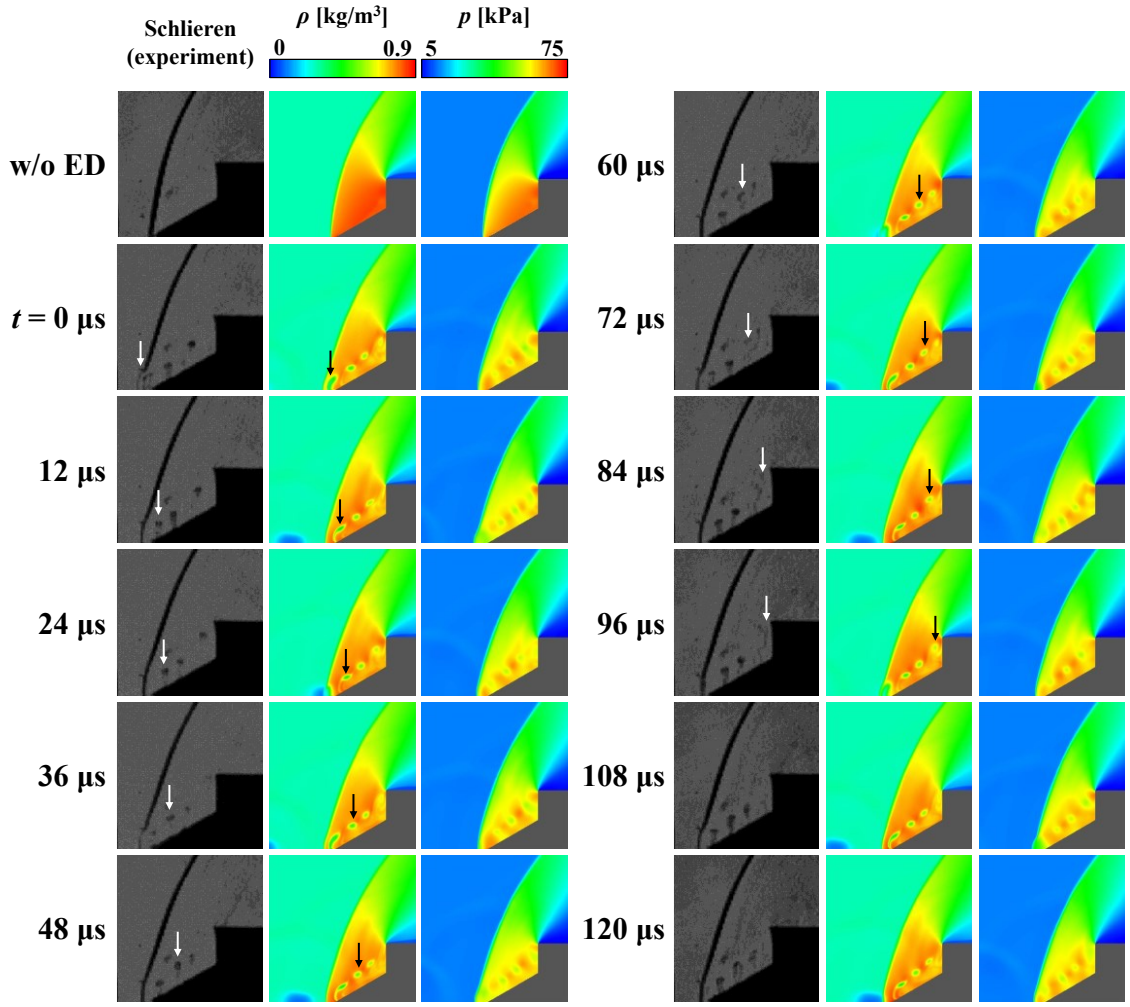

Figure 4.3 Instant Schlieren images obtained by experiment, and density and pressure distributions obtained by calculation. Model configuration of l_c = 8.7 mm, θ_c = 30° and energy supplying condition of E = 5.0 mJ/pulse and f = 30 kHz. Arrows indicate the same baroclinic vortex.

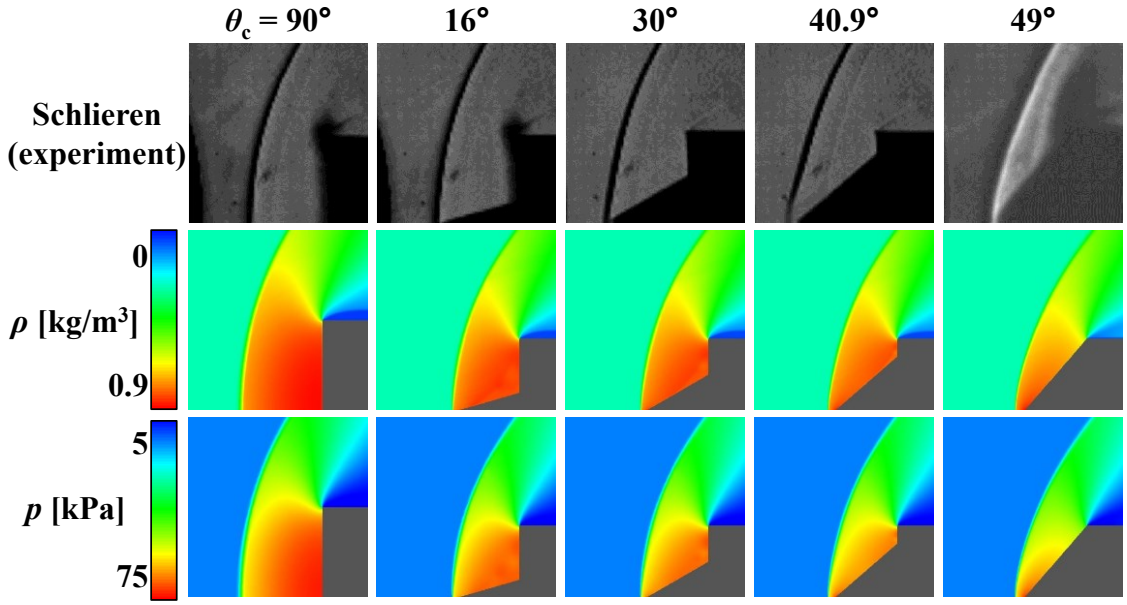

Figure 4.4 Flow field structure difference without energy deposition of l_c = 8.7 mm, and θ_c is used as a parameter.

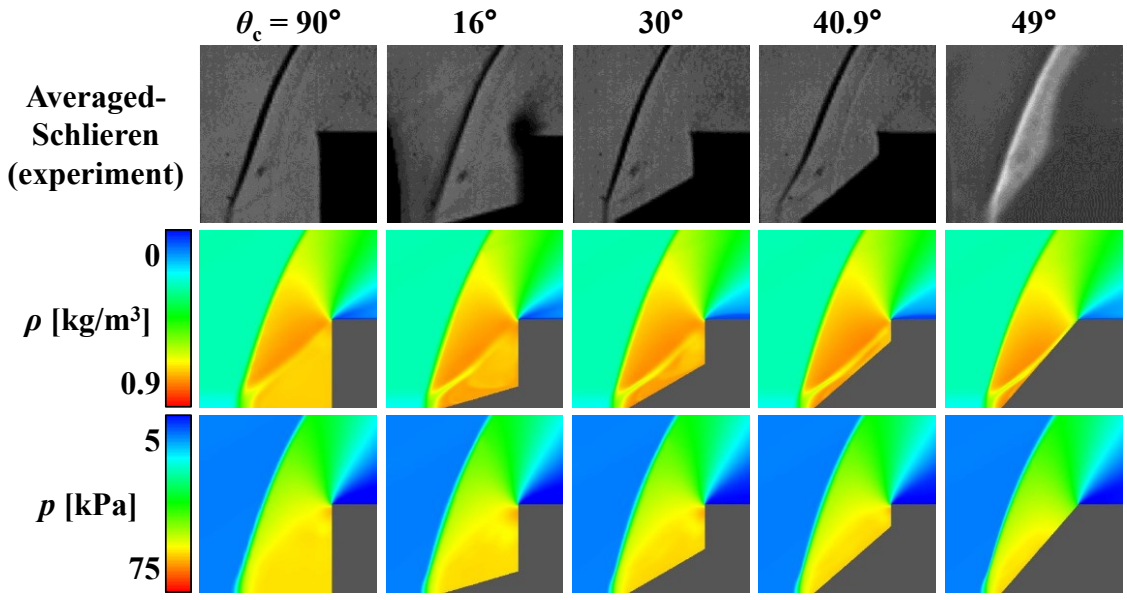

Figure 4.5 Flow field structure difference with f = 30 kHz energy deposition of l_c = 8.7 mm, and θ_c is used as a parameter. Flow fields are obtained by time-averaging of 500 μs.

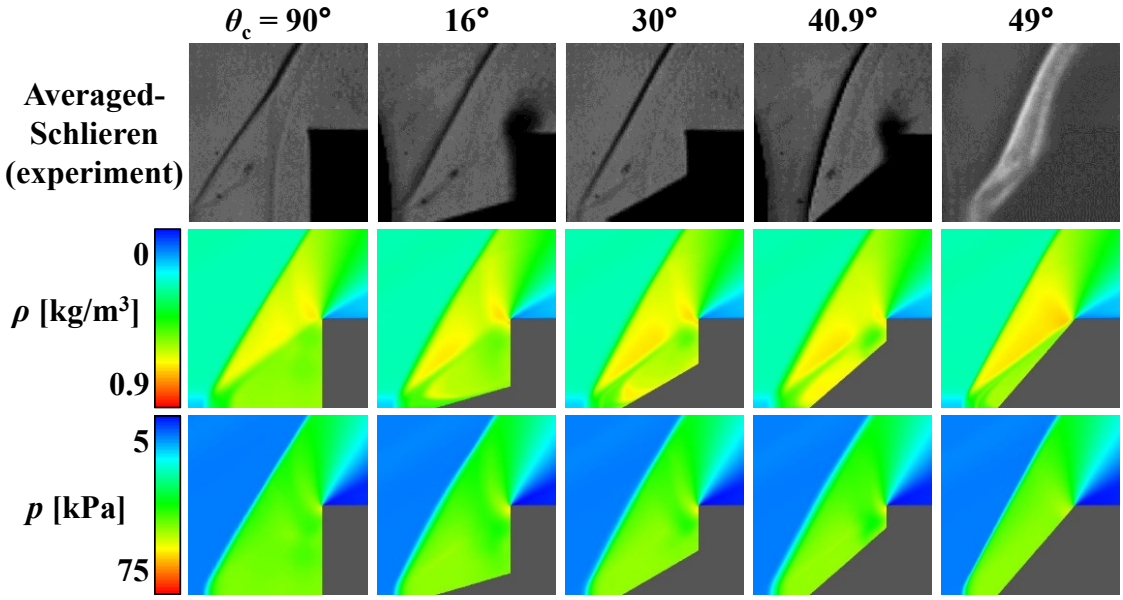

Figure 4.6 Flow field structure difference with f = 60 kHz energy deposition of l_c = 8.7 mm, and θ_c is used as a parameter. Flow fields are obtained by time-averaging of 500 μs.

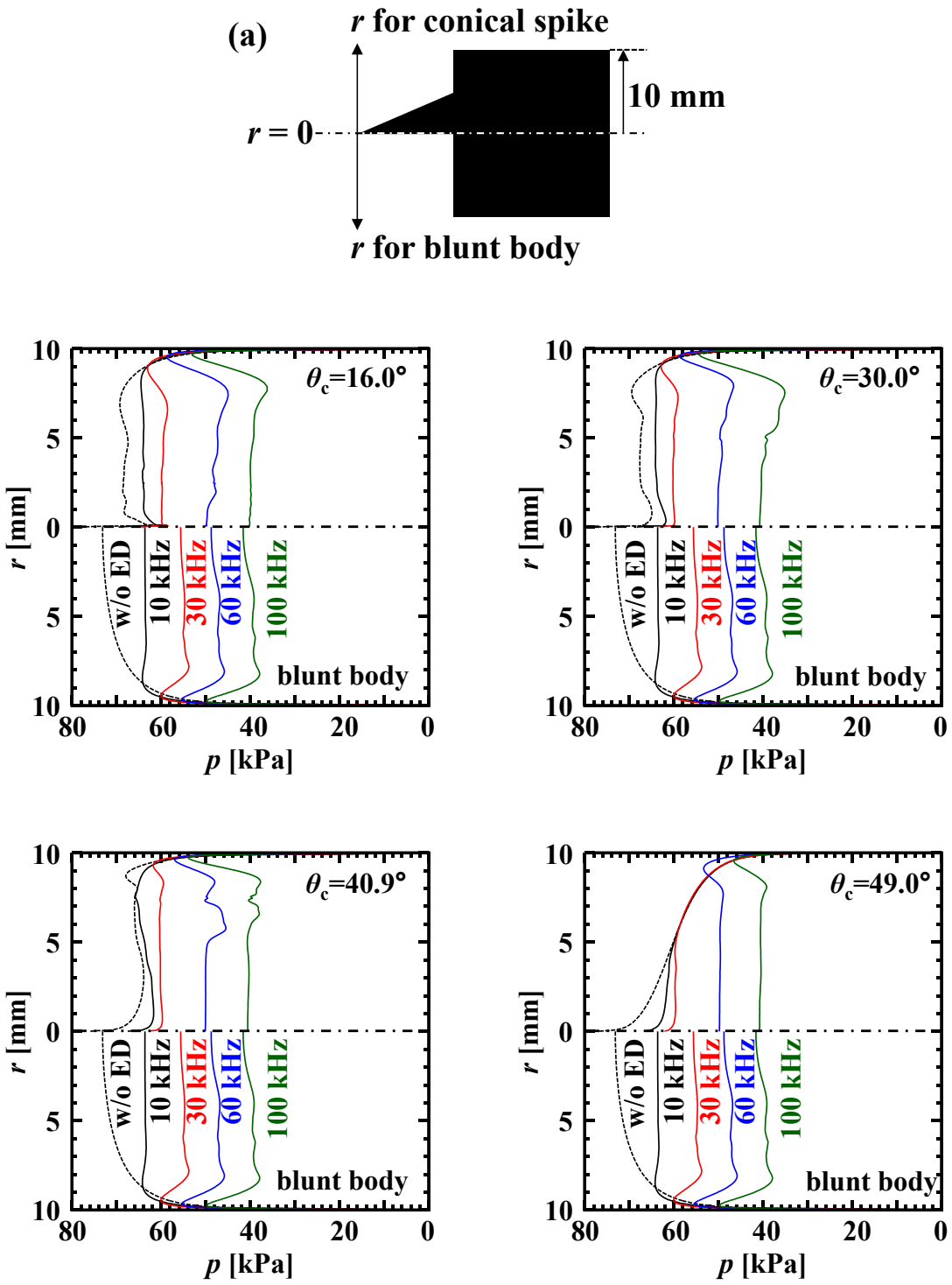

Figure 4.7 Model surface pressure distributions of l_c = 8.7 mm with different θ_c values. (a) shows the axis direction.

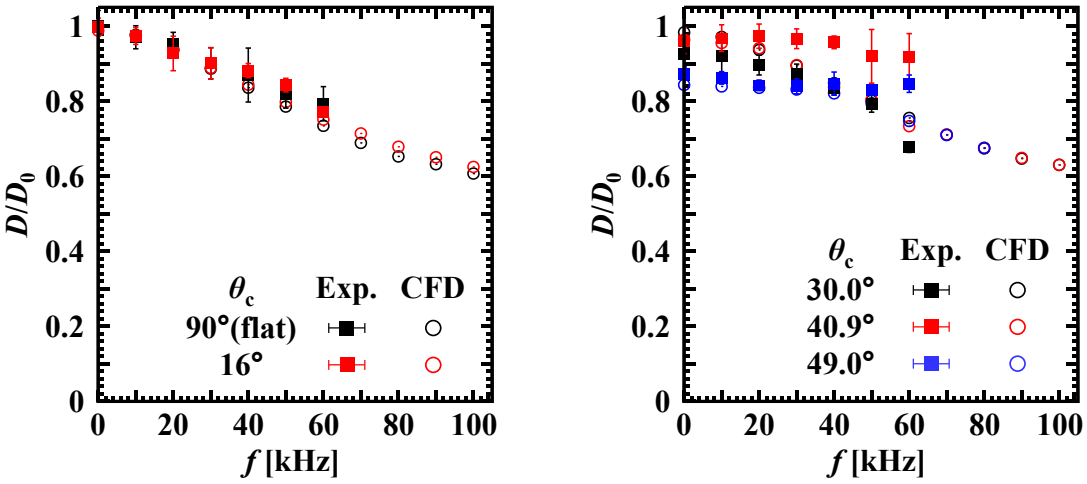

Figure 4.8 Drag value of l_c = 8.7 mm with different θ_c values as a function of f. Error bars represent the measurement error of experiments.

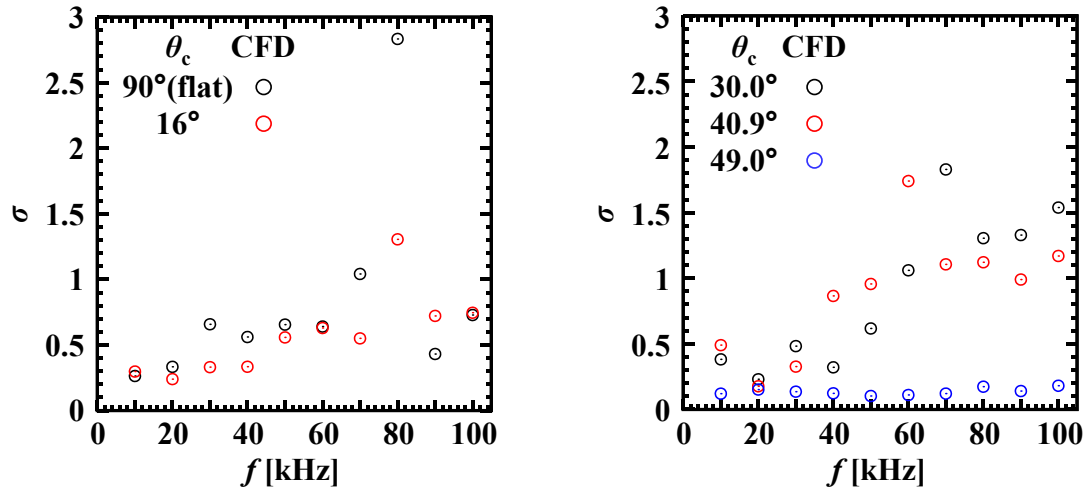

Figure 4.9 Standard deviation of the drag in averaged time of Figure 4.8.

4.2.2 Effect of Length of Conical Spike

Time averaged Schlieren images, and time averaged density and pressure distributions with θ_c = 30.0°, different l_c values and the case without and with energy deposition of f = 30, 60 kHz are shown in Figs. 4.10, 4.11 and 4.12, where the shock stand-off distance, δ, of the blunt-cylinder-head model is 8.7 mm.

In the absence of the energy deposition condition, the experimental results show that the shock wave shape depends on l_c value: a bow shock over the entire front of the model is formed for $l_c \leq 8.7$ mm; a conical shock is formed at the central region for l_c = 10.0 mm; a conical shock over the entire front of the model is formed for l_c = 17.3. These tendencies are also seen in calculations. In the case of $l_c \leq 8.7$ with energy deposition, experiment shows that the shock wave is deformed over the entire surface. This deformation is also observed in calculation. Additionally, this deformation is similar to the above mentioned deformation. In the case of l_c = 10.0 mm with energy deposition, experiment shows that the central region of the frontal shock experiences conical shock because the l_c is longer than the shock stand-off distance of blunt body, and this conical shock is maintained under lower-frequency energy depositions. But in the case of f = 60 kHz, the shock wave is deformed and is detached by the energy deposition. On the other hand, calculation shows that the conical spike is taken into the shock layer even when the frequency is lower, and the shock wave deformation by the energy deposition is similar to $l_c \leq 8.7$. In the case of l_c = 17.3 with energy deposition, both experiment and calculation show that the shock wave deformation is not observed under these frequency conditions.

Model surface spatial pressure distributions obtained by averaging 500 μs for without and with energy deposition of f =10, 30, 60, 100 kHz are shown in Fig. 4.13. The effect of the energy deposition on the pressure distribution is similar to that in the apex angle varied case

in Section 4.2.1. However, the effect of the energy deposition for l_c = 17.3 is small because the pressure is smaller than in the other models.

The drag performance obtained by experiment and calculation with different l_c values as a function of f is shown in Fig. 4.14. When there is no conical spike and l_c = 6.0 mm, the calculation result well agrees with the experimental result. When l_c = 8.7 mm, the calculation result qualitatively agrees with the experimental result, but the drag obtained by experiment is smaller than that obtained by calculation. When l_c = 10.0 mm, the experiment and the calculation show qualitatively different results: in the experiment, the drag is nearly constant when $f \leq 40$ kHz, after which the drag decreases as f increases; in the calculation, the drag decreases as f increases. When l_c = 17.3 mm, in both the experiment and the calculation, the drag is nearly constant regardless of whether energy deposition occurs.

The drag performance obtained by the calculation of l_c = 10.0 mm has different tendency to experimental result. This discrepancy is likely to be caused by the shock wave profile difference without energy deposition as shown in Fig. 4.10. The calculation result of l_c = 10.0 mm shows that the tip of the spike is within the shock layer even under the lower-frequency condition, and this tendency is similar to l_c = 6.0, 8.7 mm. On the other hand, for the experimental result of l_c = 10.0 mm, the tip of the spike is projecting into the shock layer and a conical shock is formed in the central region under the lower frequency condition. Therefore, the baroclinic effect and the vorticity are small at a low frequency. Under a higher frequency, the spike is taken in the shock layer and the shock wave is deformed to a bow shock over the entire front of the surface. Therefore, the baroclinic effect becomes larger. From these observations, the frequency dependence of the measured drag can be interpreted as follows: the conical shock at the central region is kept at $f \leq 40$ kHz; the central conical shock is deformed to a bow shock at $f \geq 40$ kHz. The quantitative difference between

experiment and calculation of l_c = 8.7 mm is still unknown.

To summarize the foregoing, it is found that the drag is effectively reduced by energy deposition at lower frequencies only if the length of the spike over the model is shorter than the shock stand-off distance of the blunt body.

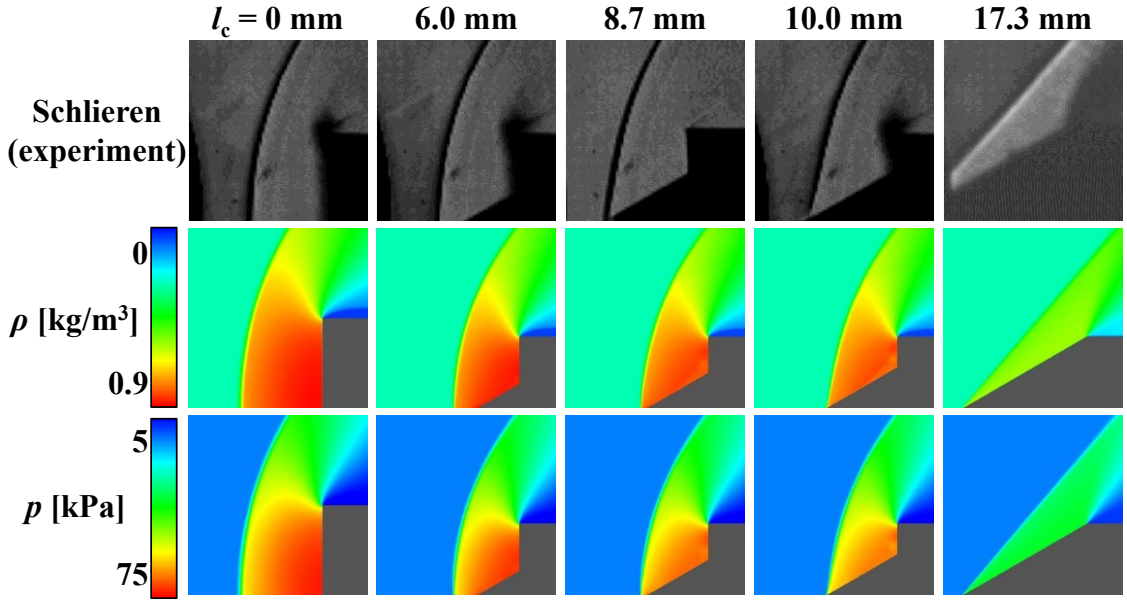

Figure 4.10 Flow field structure difference without energy deposition of θ_c = 30.0° and l_c is used as a parameter.

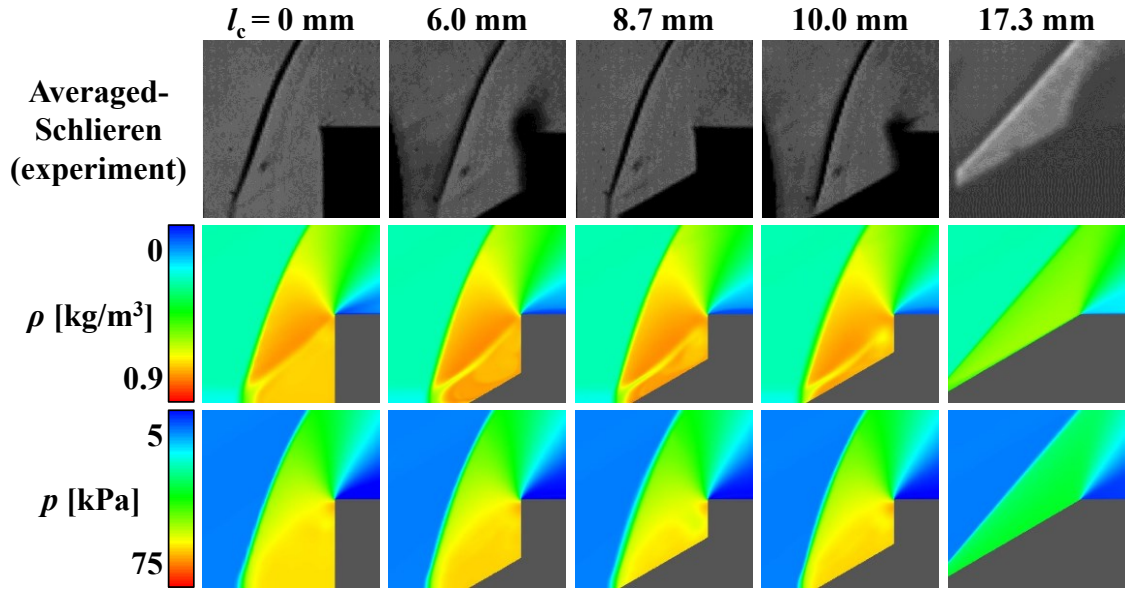

Figure 4.11 Flow field structure difference with f = 30 kHz of θ_c = 30.0° and l_c is used as a parameter. Flow fields are obtained by time-averaging of 500 μs.

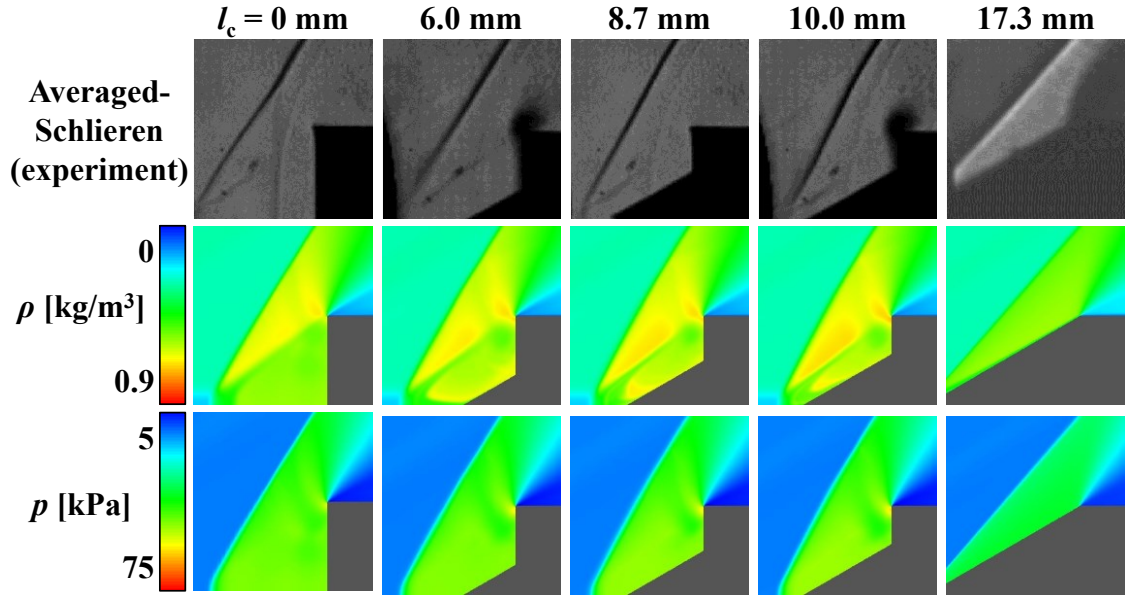

Figure 4.12 Flow field structure difference with f = 60 kHz of θ_c = 30.0° and l_c is used as a parameter. Flow fields are obtained by time-averaging of 500 μs.

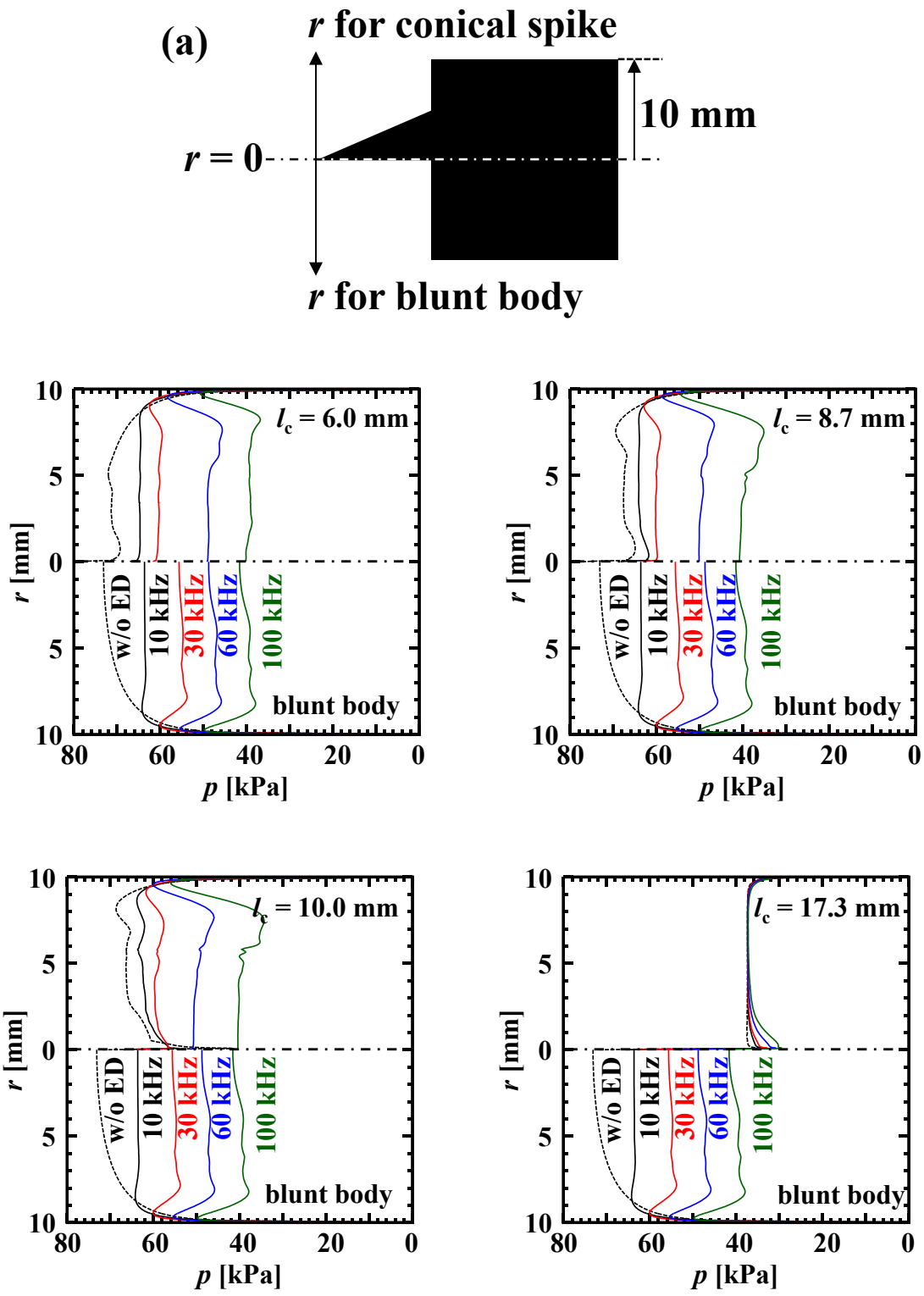

Figure 4.13 Model surface pressure distributions of θ_c = 30.0° with different l_c values. (a) shows the axis direction.

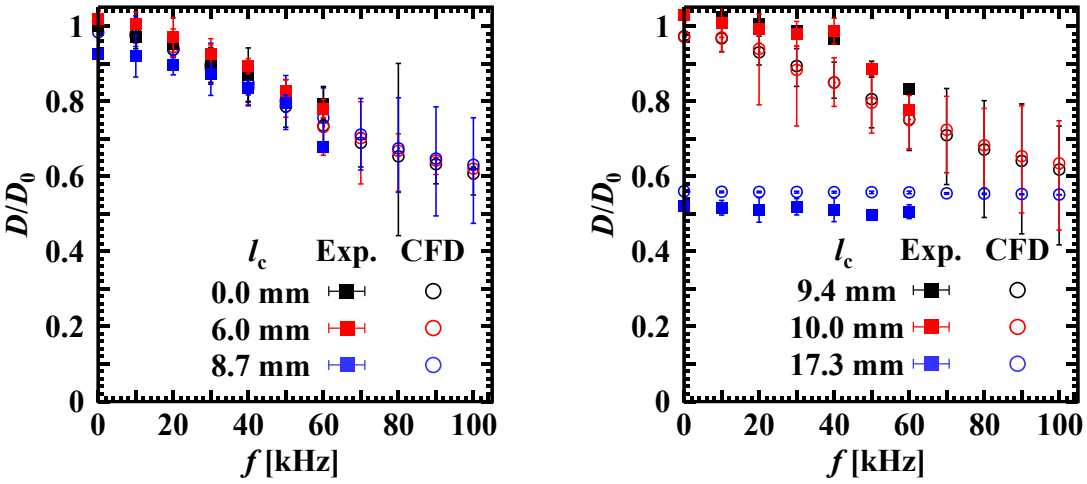

Figure 4.14 Drag value of $\theta_c = 30.0°$ with different l_c values as a function of f. Error bars represent the measurement error of experiments.

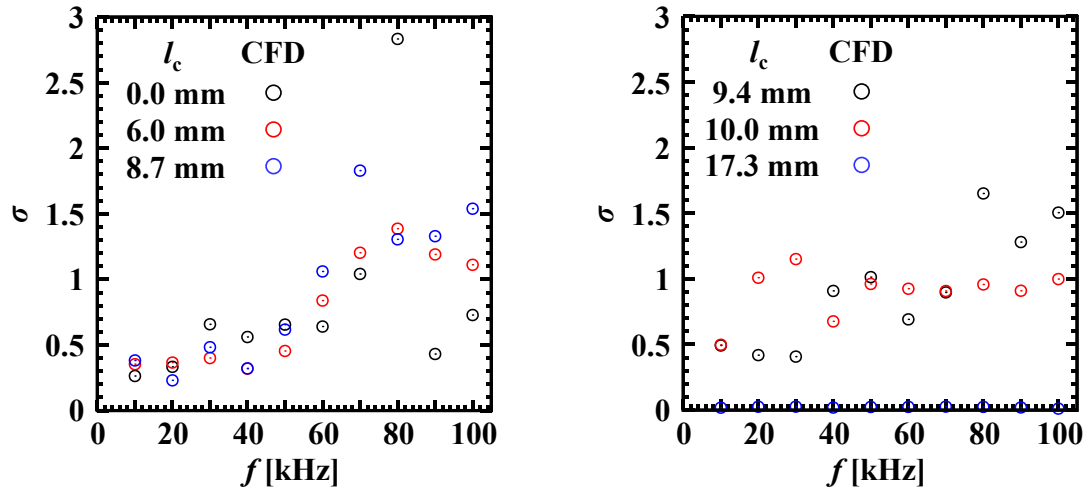

Figure 4.15 Standard deviation of the drag in averaged time of Figure 4.14.

4.2.3 Effect of Highly Repetitive Energy Deposition

From the above, the effect of energy deposition at higher frequencies up to 200 kHz on the blunt body both without a conical spike and with a spike of l_c = 6.0 mm, θ_c = 30° was calculated because the frequency of 200 kHz cannot be investigated owing to the limitation of the energy source in the experiment. The frequency dependences of the drag performance and of the energy deposition efficiency are shown in Figs. 4.16 and 4.17, respectively. The time-averaged spatial distributions of pressure and density for f = 200 kHz are shown in Fig. 4.18. From Fig. 4.16, the drag reduction by energy deposition has a tendency to be asymptotic to a constant value with increasing repetition frequency, with or without a spike. From Fig. 4.17, the energy deposition efficiency has a maximum peak around f = 50 kHz. This maximum efficiency is caused by the trade-off of the input power, which is linear increasing with f, and reduced drag, which is asymptotic constant. From Fig. 4.18, it is clear that the effect of energy deposition with a higher repetition frequency exceeds the effect of the conical spike because the shock wave is deformed over the entire front of the tip, and the difference between with spike and without spike is not observed.

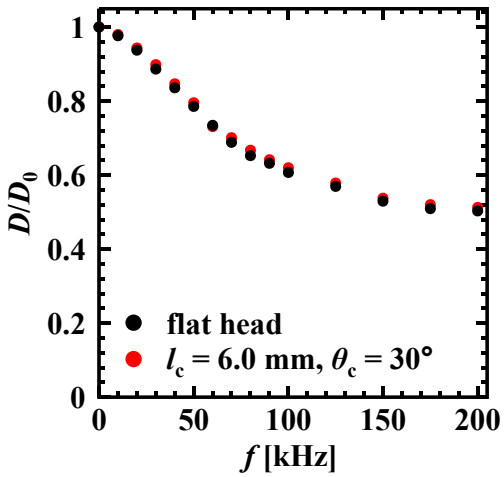

Figure 4.16 Drag as a function of f; l_c = 0.0 mm, θ_c = 90° and l_c = 6.0 mm, θ_c = 30°.

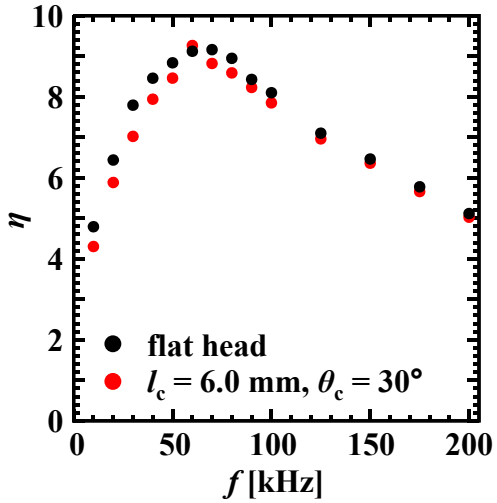

Figure 4.17 Efficiency of energy deposition as a function of f; l_c = 0.0 mm, θ_c = 90° and l_c = 6.0 mm, θ_c = 30°.

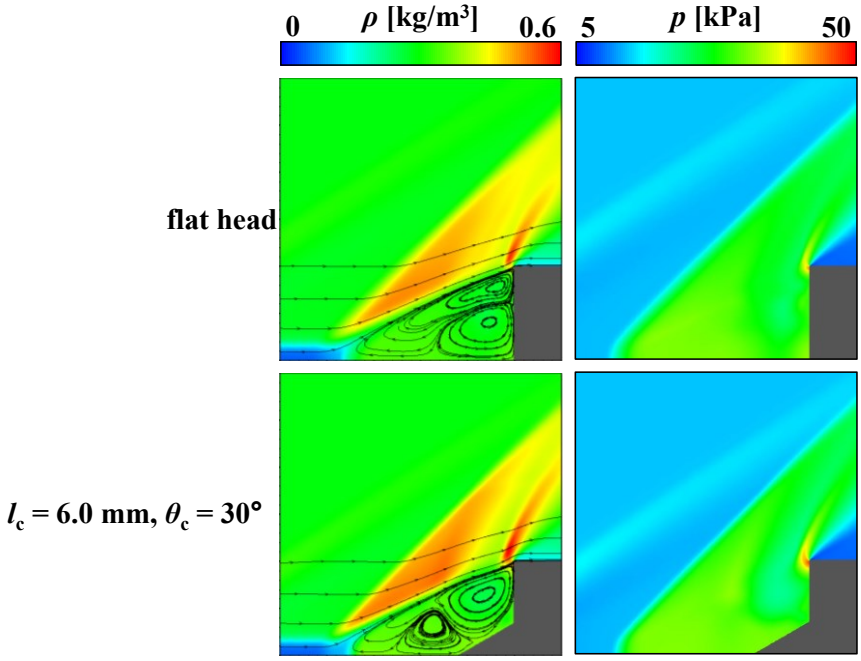

Figure 4.18 Time-averaged flow field structure for f = 200 kHz; l_c = 0.0 mm, θ_c = 90° and l_c = 6.0 mm, θ_c = 30°.

4.3 Effect of Energy Deposition on Unsteady Mode

The effect of the energy deposition on unsteady flow, which is caused by the shock wave and boundary layer interactions, is also studied. The conditions of $\theta_c = 15°$ and $l_c = 9.3$, 18.7, 28.0 mm are unsteady mode with shock wave oscillated flow. The shock wave oscillation, which is shown in Ref. 53, occurs under these conditions. In the following, $\theta_c = 15°$ and $l_c = 18.7$ mm is used as a typical case, and the effect of energy deposition is compared. The time varied Schlieren images and density contours are shown in Figs. 4.19 and 4.20, respectively. From these figures, it is evident that the oscillation frequency shock wave is not changed by energy deposition under both experiment and calculation. The temporal drag history obtained by calculation is shown in Fig. 4.21. Frequency analyzed results of the temporal drag history with and without energy deposition are shown in Fig. 4.22. From these figures, the temporal drag oscillation frequency and amplitude are not affected by energy deposition. Hence, the drag reduction effect of energy deposition on the oscillation mode is small.

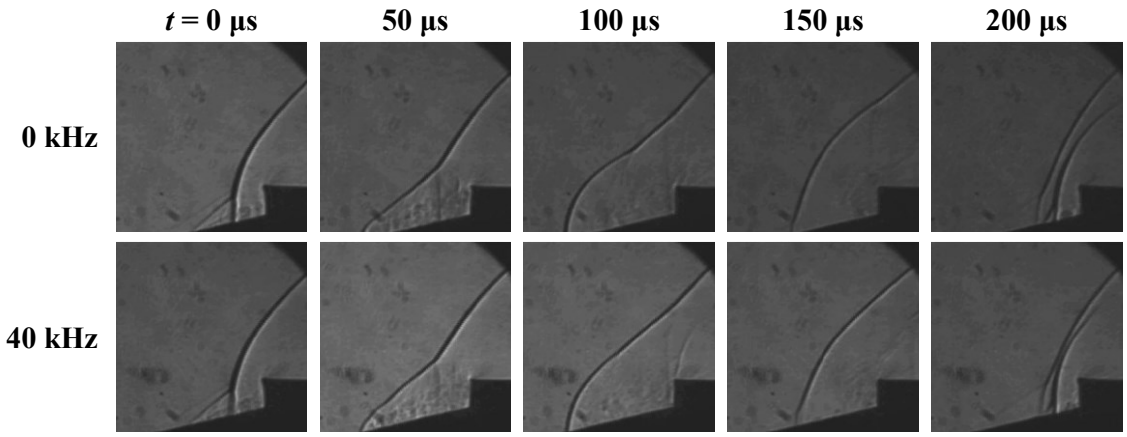

Figure 4.19 Experimental Schlieren images for l_c = 18.7 mm, θ_c = 15° without energy deposition and with E = 5.4 mJ/pulse, f = 40 kHz.

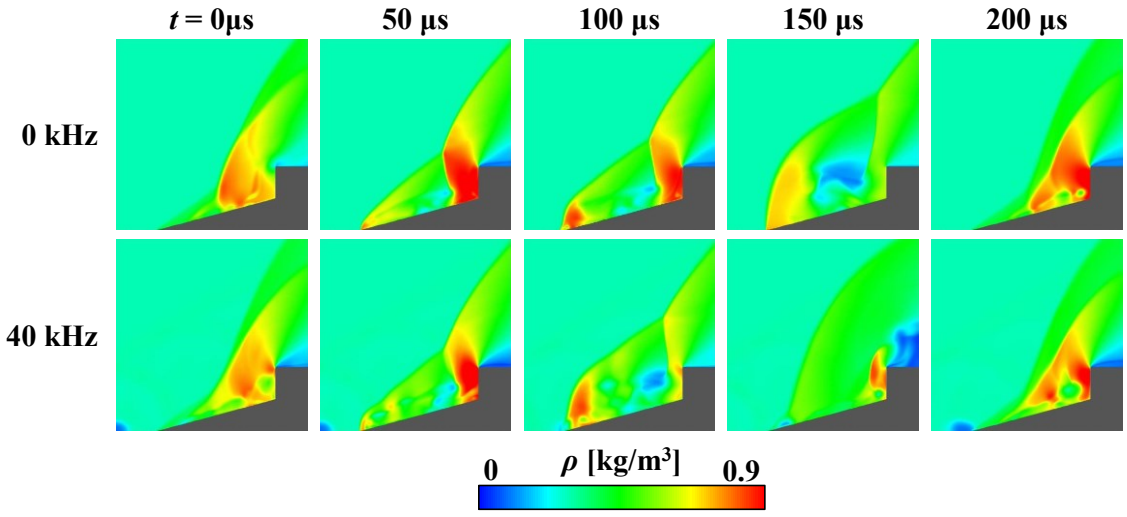

Figure 4.20 Density distributions of l_c = 18.7 mm, θ_c = 15° with and without energy deposition and with $\eta_a E$ = 2.0 mJ/pulse, f = 40 kHz.

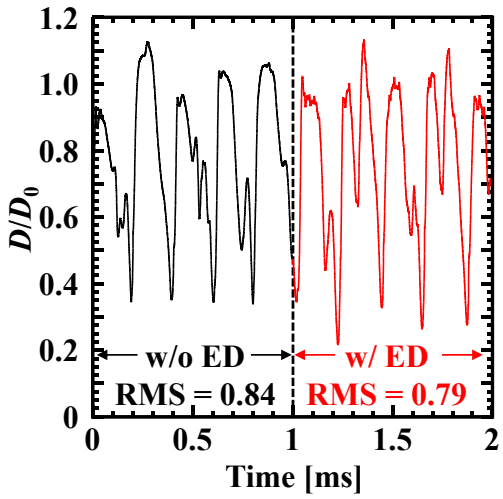

Figure 4.21 Temporal history of drag without energy deposition and with energy deposition.

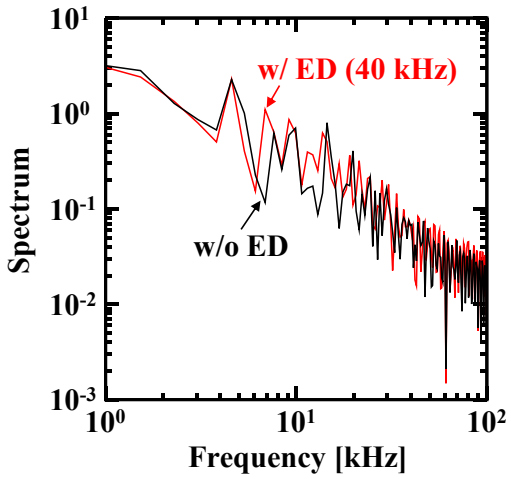

Figure 4.22 Frequency analysis results of the temporal drag history.

4.4 Summary of This Chapter

In this chapter, the drag reduction performances over a blunt body with conical spike model using energy depositions are studied by both experiment and simulation. The presence of the conical spike appeared only lower repetition frequency conditions, and the drags of the blunt body and the blunt body with conical spike became almost same at higher frequency conditions.

- The combined effect of the conical spike and energy deposition appeared under lower repetition frequency conditions, but at higher frequencies, the combined effect became smaller because the energy deposition effect is stronger.
- The combined effect becomes stronger when the length of the conical spike is shorter than the shock stand-off distance of the blunt cylinder model.
- Under a higher-frequency condition of 200 kHz energy deposition, a significant drag reduction is obtained from the calculation, and the reduced drag with conical spike model is similar to that without conical spike model. Hence, the presence of the conical spike does not affect to the drag reduction performance at higher-frequency conditions, the drag reduction by energy deposition exceeds that due to the conical spike.
- The energy deposition cannot suppress the strong shock wave oscillation that was observed in the longer length of the spike model.

Chapter

5

Conclusions

In the present thesis, a supersonic drag reduction mechanism using energy deposition was analyzed in detail by both a numerical and an experimental approach. Force measurement system was newly developed for quantitative comparison between experimental and numerical results. The theoretical analyses of ring force balance for practical use were conducted and a ring force balance system was fabricated on the basis of these analyses. The fabricated ring force balance successfully measured the force component independently without causing unstart in a wind tunnel with small test section.

From past studies, the drag reduction using single pulse energy deposition can be related to the baroclinic vortex ring behavior. When the vortex ring resides in the front of the model, the pressure of frontal surface of the model is mitigated. This mitigation leads to a reduction in the drag. However, the drag reduction using repetitive pulse energy deposition has not been related to the vortex ring behavior. In this thesis, this vortex behavior is also observed for single pulse energy deposition, additionally, this vortex ring behavior has also important role for repetitive pulse energy depositions. The frequency dependence of the drag reduction can be related to the vortex ring residence time in the shock layer, that is the average number

of the vortex rings.

If the repetition interval is longer than the vortex residence time, the effect of the energy deposition can be described by the superposition of successive energy depositions. Under studied conditions, the successive energy depositions can be treated as the superposition of single pulse energy deposition for frequencies below 5 kHz because the vortex ring residence time in the shock layer is about 200 μs. In addition, under these repetition frequencies, the combined effect of the conical spike and energy deposition appeared.

The pulse-to-pulse interaction appeared when the repetition interval is shorter than the vortex residence time. When one or two vortex rings remained in the shock layer, which is from 5 to 15 kHz in these studies, these vortex rings always mitigate the pressure distribution of the model frontal surface. Under these conditions, the vortex residence time decreases with repetition frequency, but the energy deposition effect on the drag reduction becomes larger because the pressure mitigation effect becomes larger.

Interactions among successive vortex rings appeared when more than two vortex rings stayed in the shock layer, for frequencies above 15 kHz. Because the pressure distribution in front of the conical spike model surface is similar to that of the blunt body under these conditions, the drag reduction of the conical spike become smaller.

A three-dimensional motion of the vortex ring is observed in the experiment with highly repetitive energy deposition over the flat-head cylinder model. There is a discrepancy between the drag reduction in the experiment and the calculated drag reduction because the calculations neglect the three-dimensional effect. Hence, this non-axisymmetric motion affects the drag reduction owing to modifications of the effective shock stand-off distance and pressure distribution. On the other hand, this difference for the conical spike model is smaller than the difference for the flat-head cylinder model. A possible reason for the

reduced difference is that the flow is limited to axisymmetric flow by the effect of the conical spike. Finally, from the calculation results of 200 kHz energy deposition, the drag is significantly reduced by energy deposition and its drag reduction is independent of the presence of the conical spike.

In this study, the energy deposition effect to the drag reduction over the axisymmetric model with a diameter of 20 mm using input power in range of 0 to 1 kW was investigated. The results show that the efficiency of energy deposition has a peak value at around input power of 250 W with η = 10 and - ΔD = 20%. The scale of this study is one hundredth of actual aircrafts and rockets. If the drag reduction performances is increased along the object size, input power for effective energy deposition is also increased along the object size. Thereby, for effective drag reduction using the energy deposition a power higher than 200 MW would be necessary if a cubic power law is applied in practical application. However, when the object size increased, the vortex ring residence time will be longer and the pressure modulation time will be also extended. The further investigation about the relation between the object scale and the drag reduction performance is necessary because the drag reduction performance cannot be evaluated by the simple estimation.

Bibliography

1 Cheung, S., *Supersonic Airplane Study and Design*, MCAT Institute, 1993.

2 Morgenstern, J., Norstrud, N., Stelmack, M., and Skoch, C., "Final Report for the Advanced Concept Studies for Supersonic Commercial Transports Entering Service in the 2030 to 2035 Period, N+3 Supersonic Program," *NASA CR*, vol. 35, 2010, pp. 1–55.

3 Lotfin, L. K. J., "The Evolution of Modern Aircraft," *NASA SP-468*, 1985.

4 Ocheltree, C. L., and Choi, S., "Design of Optimum Equivalent-Area Target for High-Fidelity Low-Boom Aircraft Design," *33rd AIAA Applied Aerodynamics Conference*, 2015, pp. 1–12.

5 Wintzer, M., Ordaz, I., and Fenbert, J. W., "Under-Track CFD-Based Shape Optimization for a Low-Boom Demonstrator Concept," *33rd AIAA Applied Aerodynamics Conference*, 2015, pp. 1–24.

6 Li, W., "Feasibility of Supersonic Aircraft Concepts for Low-Boom and Flight Trim Constraints," *33rd AIAA Applied Aerodynamics Conference*, 2015, pp. 11–17.

7 Yoshida, K., "Supersonic Drag Reduction Technology in the Scaled Supersonic Experimental Airplane Project by JAXA," *Progress in Aerospace Sciences*, vol. 45, 2009, pp. 124–146.

8 Bushnell, D. M., "Shock Wave Drag Reduction," *Annual Review of Fluid Mechanics*, vol. 36, Jan. 2004, pp. 81–96.

9 Maull, D. J., "Hypersonic Flow over Axially Symmetric Spiked Bodies," *Journal of Fluid Mechanics*, vol. 8, 1960, pp. 584–592.

10 Feszty, D., Badcock, K. J., and Richards, B. E., "Driving Mechanisms of High-Speed Unsteady Spiked Body Flows, Part 1: Pulsation Mode," *AIAA Journal*, vol. 42, 2004, pp. 95–106.

11 Feszty, D., Badcock, K. J., and Richards, B. E., "Driving Mechanisms of High-Speed Unsteady Spiked Body Flows, Part 2: Oscillation Mode," *AIAA Journal*, vol. 42, 2004.

12 Shang, J. S., Hayes, J., Wurtzler, K., and Strang, W., "Jet-Spike Bifurcation in High-Speed Flows," *AIAA Journal*, vol. 39, 2001, pp. 1159–1165.

13 Shang, J. S., "Plasma Injection for Hypersonic Blunt-Body Drag Reduction," *AIAA*

Journal, vol. 40, 2002, pp. 1178–1186.

14 Erdem, E., Kontis, K., and Yang, L., "Steady Energy Deposition at Mach 5 for Drag Reduction," *Shock Waves*, vol. 22, Aug. 2012, pp. 285–298.

15 Shneider, M. N., Macheret, S. O., Zaidi, S. H., Girgis, I., and Miles, R. B., "Virtual Shapes in Supersonic Flow Control with Energy Addition," *Journal of Propulsion and Power*, vol. 24, Sep. 2008, pp. 900–915.

16 Schulein, E., and Zheltovodov, A., "Effects of Steady Flow Heating by arc Discharge Upstream of Non-Slender Bodies," *Shock Waves*, vol. 21, Feb. 2011, pp. 383–396.

17 Myrabo, L. N., Raizer, Y. P., Shneider, M. N., and Bracken, R., "Reduction of Drag and Energy Consumption during Energy Release Preceding a Blunt Body in Supersonic Flow," *High Temperature*, vol. 42, Nov. 2004, pp. 901–910.

18 Exton, R. J., Balla, R. J., Shirinzadeh, B., Brauckmann, G. J., Herring, G. C., Kelliher, W. C., Fugitt, J., Lazard, C. J., and Khodataev, K. V., "On-Board Projection of a Microwave Plasma Upstream of a Mach 6 Bow Shock," *Physics of Plasmas*, vol. 8, 2001, p. 5013.

19 Adelgren, R. G., Yan, H., Elliott, G. S., Knight, D. D., Beutner, T. J., and Zheltovodov, A. A., "Control of Edney IV Interaction by Pulsed Laser Energy Deposition," *AIAA Journal*, vol. 43, Feb. 2005, pp. 256–269.

20 Tret'yakov, P. K., and Garanin, A. F., "Control of Supersonic Flow around Bodies by Means of High-Power Recurrent Optical Breakdown," *Physics-Doklay*, vol. 41, 1996, pp. 566–597.

21 Kim, J.-H., Matsuda, A., Sakai, T., and Sasoh, A., "Wave Drag Reduction Performance with Acting Spike Induced by Laser-Pulse Energy Depositions," *AIAA Journal*, vol. 49, Sep. 2011, pp. 2076–2078.

22 Zudov, V. N., Tret'yakov, P. K., Tupikin, A. V., and Yakovlev, V. I., "Supersonic Flow Past a Thermal Source," *Fluid Dynamics*, vol. 38, Sep. 2003, pp. 782–793.

23 Riggins, D., Nelson, H. F., and Johnson, E., "Blunt-Body Wave Drag Reduction using Focused Energy Deposition," *AIAA Journal*, vol. 37, Jan. 1999, pp. 460–467.

24 Riggins, D. W., and Nelson, H. F., "Hypersonic Flow Control using Upstream Focused Energy Deposition," *AIAA Journal*, vol. 38, 2000, pp. 4–6.

25 Borzov, V. Y., Rybka, I. V., and Yur'ev, A., "Effect of Local Energy Supply to a

Hypersonic Flow on the Drag of Bodies with Different Nose Bluntness," *Journal of Engineering Physics and Thermophysics*, vol. 67, 1995, pp. 997–1002.

26 Kremeyer, K., Ebastian, K., and Shu, C.-W., "Computational Study of Shock Mitigation and Drag Reduction by Pulsed Energy Lines," *AIAA Journal*, vol. 44, Aug. 2006, pp. 1720–1731.

27 Plooster, M. N., "Shock Waves from Line Sources. Numerical Solutions and Experimental Measurements," *Physics of Fluids*, vol. 13, 1970, pp. 2665–2675.

28 Georgievskii, P. Y., and Levin, V. a., "Control of the Flow Past Bodies Using Localized Energy Addition to the Supersonic Oncoming Flow," *Fluid Dynamics*, vol. 38, Sep. 2003, pp. 794–805.

29 Kandala, R., and Candler, G. V., "Numerical Studies of Laser-Induced Energy Deposition for Supersonic Flow Control," *AIAA Journal*, vol. 42, 2004, pp. 2266–2275.

30 Zaidi, S. H., Shneider, M. N., and Miles, R. B., "Shock-Wave Mitigation Through Off-Body Pulsed Energy Deposition," *AIAA Journal*, vol. 42, 2004, pp. 326–331.

31 Georgievskii, P. Y., and Levin, V. A., "Unsteady Interaction of a Sphere with Atmospheric Temperature Inhomogeneity at Supersonic Speed," *Fluid Dynamics*, vol. 28, 1993, pp. 568–574.

32 Zudov, V. N., Tretyakov, P. K., and Tupikin, A. V., "Unsteadiness Effects at a Pulsed-periodic Energy Supply to Supersonic Flow," *AIAA Plasmadynamics and Lasers Conference*, 2009, pp. 1–13.

33 Sakai, T., "Supersonic Drag Performance of Truncated Cones with Repetitive Energy Depositions," *International Journal of Aerospace Innovations*, vol. 1, Mar. 2009, pp. 31–44.

34 Ogino, Y., Ohnishi, N., Taguchi, S., and Sawada, K., "Baroclinic Vortex Influence on Wave Drag Reduction Induced by Pulse Energy Deposition," *Physics of Fluids*, vol. 21, 2009, p. 066102.

35 Knight, D. D., "Survey of Aerodynamic Drag Reduction at High Speed by Energy Deposition," *Journal of Propulsion and Power*, vol. 24, Nov. 2008, pp. 1153–1167.

36 Sasoh, A., and Kim, J., "Fly By Light Power: Improvement of Aerodynamic Performance with Energy Deposition," *Aeronautical and space sciences Japan* (*in Japanese*), vol. 59, 2011, pp. 233–237.

37 Kim, J.-H., Matsuda, A., and Sasoh, A., "Interactions among Baroclinically-Generated Vortex Rings in Building Up an Acting Spike to a Bow Shock Layer," *Physics of Fluids*, vol. 23, 2011, p. 021703.

38 Richtmyer, R. D., "Taylor Instability in Shock Acceleration of Compressible Fluids," *Communications on Pure and Applied Mathematics*, vol. XIII, 1960, pp. 297–319.

39 Charney, J. G., "The Dynamics of Long Waves in a Baroclinic Westerly Current," *Journal of Meteorology*, vol. 4, 1947, pp. 136–162.

40 Sasoh, A., Sekiya, Y., Sakai, T., Kim, J.-H., and Matsuda, A., "Supersonic Drag Reduction with Repetitive Laser Pulses Through a Blunt Body," *AIAA Journal*, vol. 48, Dec. 2010, pp. 2811–2817.

41 Kawazoe, H., and Morita, S., "Dynamic Characteristics of Rolling Delta Wing with High Angle of Attack under the Ground Effect," *Journal of the Japan Society for Aeronautical and Space Sciences* (*in Japanese*), vol. 52, 2004, pp. 272–279.

42 Iwakawa, A., Osuka, T., Shoda, T., Sasoh, A., and Kawazoe, H., "Ring-Force Balance System for Small Wind Tunnels," *Transactions of Japan Society for Aeronautical and Space Sciences*, vol. 13, 2015, pp. 51–60.

43 Iwakawa, A., Sakai, T., and Sasoh, A., "Repetition Frequency Dependence of Wave Drag Reduction Induced by Laser-Pulse-Energy Depositions," *Transactions of the Japan Society for Aeronautical and Space Sciences*, vol. 11, 2013, pp. 53–60.

44 Iwakawa, A., Hasegawa, N., Osuka, T., Majima, R., Sakai, T., and Sasoh, A., "Supersonic Drag Reduction over a Blunt-Body by Combination of Conical Spike and Energy Deposition," *Journal of the Japan Society for Aeronautical and Space Sciences* (*in Japanese*), vol. 62, 2014, pp. 99–106.

45 Sasoh, A., Kim, J.-H., Yamashita, K., and Sakai, T., "Supersonic Aerodynamic Performance of Truncated Cones with Repetitive Laser Pulse Energy Depositions," *Shock Waves*, vol. 24, Jul. 2013, pp. 59–67.

46 Wada, Y., and Liou, M.-S., "A Flux Splitting Scheme with High-Resolution and Robustness for Discontinuities," *AIAA Paper*, 1994, pp. 94–0083.

47 Wada, Y., and Liou, M.-S., "An Accurate and Robust Flux Splitting Scheme for Shock and Contact Discontinuities," *SIAM Journal on Scientific Computing*, vol. 18, 1997, pp. 633–657.

48 Van Leer, B., "Towards the Ultimate Conservative Difference Scheme. IV. A New

Approach to Numerical Convection," *Journal of Computational Physics*, vol. 23, 1977, pp. 276–299.

49 van Leer, B., "Towards the ultimate conservative difference scheme. V. A second-order sequel to Godunov's method," *Journal of Computational Physics*, vol. 32, 1979, pp. 101–136.

50 Yoon, S., and Jameson, A., "Lower-Upper Symmetric-Gauss-Seidel Method for the Euler and Navier-Stokes Equations," *AIAA Journal*, vol. 26, 1988, pp. 1025–1026.

51 Sakai, T., Sekiya, Y., Mori, K., and Sasoh, A., "Interaction between Laser-Induced Plasma and Shock Wave over a Blunt Body in a Supersonic Flow," *Proceedings of the Institution of Mechanical Engineers, Part G: Journal of Aerospace Engineering*, vol. 222, Aug. 2008, pp. 605–617.

52 Zheltovodov, A. A., and Pimonov, E. A., "Energy Deposition Influence on Supersonic Flow Over Axisymmetric Bodies," *AIAA Aerospace Sciences Meeting and Exhibit*, 2007.

53 Wang, Y., Ozawa, H., and Nakamura, Y., "Numerical Investigation of Supersonic Oscillatory Flow with Strong Interference over a Capsule-shaped Abort System," *Transactions of the Japan Society for Aeronautical and Space Sciences*, vol. 55, 2012, pp. 286–294.

Appendix

A

Theory of an Infinitesimally Thin Ring Force Balance

The schematic illustration of the ring force balance is shown in Fig. A.1.Here we assume the thickness of the ring is zero as the simplest case. The ring is held to the wall at point A while L and D are applied at point B, as shown in Fig. A.2 (a). Considering only the upper half of the ring because of its symmetry, the forces acting at point B are $\frac{1}{2}D$ and $\frac{1}{2}L$, as shown in Fig. A.2 (b). First, we calculate the strain at the position with an azimuthal angle of θ, when D or L is loaded at point B.

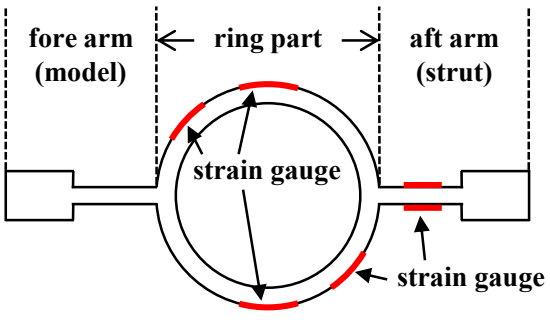

Figure A.1 Schematic image of the ring force balance.

(a) real configuration (b) equivalent configuration

Figure A.2 Schematic illustration of an infinitesimally thin ring force balance and force components.

A.1 Strain Due to the Drag Force

When D is applied to the ring, N_{D0} and M_{D0} occur at point B, as shown in Fig. A.3. From the assumption of an infinitesimally thin ring, the strain caused by the tangential force $N_{D\theta}$ can be ignored. $P_{D\theta}$ is ignored because the direction is perpendicular to the strain of interest. $M_{D\theta}$ at position θ is written as follows.

$$M_{D\theta} = M_{D0} - N_{D0}R(1-\cos\theta) + \frac{1}{2}DR\sin\theta \tag{A.1}$$

The strain energy dU stored in ds is written as follows.

$$dU = \frac{M_{D\theta}^2}{2EI}ds = \frac{1}{2EI}\left(M_{D0} - N_{D0}R(1-\cos\theta) + \frac{1}{2}DR\sin\theta\right)^2 ds \tag{A.2}$$

Using the relation $ds = Rd\theta$, U is written as follows.

$$U = \int_0^{\pi}\frac{1}{2EI}\left(M_{D0} - N_{D0}R(1-\cos\theta) + \frac{1}{2}DR\sin\theta\right)^2 Rd\theta \tag{A.3}$$

Here, U, N_{D0}, and M_{D0} must satisfy the theorem of least work; therefore, $\partial U/\partial M_{D0} = 0$ and $\partial U/\partial N_{D0} = 0$.

$$\frac{\partial U}{\partial M_{D0}} = \frac{2R}{2EI}\left\{M_{D0}\pi - N_{D0}R\pi + DR\right\} \tag{A.4}$$

$$\frac{\partial U}{\partial N_{D0}} = \frac{2R^2}{2EI}\left\{-M_{D0}\pi + \frac{3}{2}N_{D0}R\pi - DR\right\} \tag{A.5}$$

From Eqs. (A.4) and (A.5), the followings are obtained.

$$M_{D0}\pi - N_{D0}R\pi + DR = 0 \tag{A.6}$$

$$-M_{D0}\pi + \frac{3}{2}N_{D0}R\pi - DR = 0 \tag{A.7}$$

From Eqs. (A.6) and (A.7), $N_{D0} = 0$ and $M_{D0} = -DR/\pi$ are obtained. Hence,

$$M_{D\theta} = -\frac{DR}{\pi} + \frac{1}{2}DR\sin\theta = \frac{1}{2}DR\left(\sin\theta - \frac{2}{\pi}\right) \tag{A.8}$$

Therefore, ε_{D0} is obtained as

$$\varepsilon_{D0} = \frac{M_{D\theta}}{EI}\eta = \frac{\eta DR}{2EI}\left(\sin\theta - \frac{2}{\pi}\right) \tag{A.9}$$

Here, η is the distance between the center and the outside surface of the ring portion. From Eq. (A.9), the azimuthal location where $\varepsilon_{D0} = 0$ is always satisfied is $\theta_{D0} = \sin^{-1}(2/\pi) = 39.5$, 140.5°.

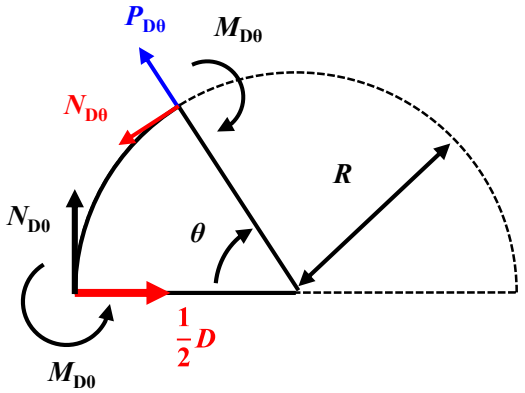

Figure A.3 Exerted force when D is applied.

A.2 Strain Due to the Lift Force

When L is applied to the ring, P_{L0} and M_{L0} occur at point B, as shown in Fig. A.4. From the assumption of an infinitesimally thin ring, the tangential force $N_{L\theta}$ can be ignored. $P_{L\theta}$ is ignored because the direction is perpendicular to the strain of interest. $M_{L\theta}$ at position θ is written as follows.

$$M_{L\theta} = M_{L0} - \frac{1}{2}LR(1-\cos\theta) + P_{L0}R\sin\theta \tag{A.10}$$

dU stored in ds is written as follows.

$$dU = \frac{M_{L\theta}^2}{2EI}ds = \frac{1}{2EI}\left(M_{L0} - \frac{1}{2}LR(1-\cos\theta) + P_{L0}R\sin\theta\right)^2 ds \tag{A.11}$$

Using the relation $ds = Rd\theta$, U is written as follows.

$$U = \int_0^{\pi} \frac{1}{2EI}\left(M_{L0} - \frac{1}{2}LR(1-\cos\theta) + P_{L0}R\sin\theta\right)^2 Rd\theta \tag{A.12}$$

Here, U, P_{L0}, and M_{L0} must satisfy the theorem of least work; therefore, $\partial U/\partial M_{L0} = 0$ and $\partial U/\partial P_{L0} = 0$.

$$\frac{\partial U}{\partial M_{L0}} = \frac{2R}{2EI}\left\{M_{L0}\pi - \frac{1}{2}LR\pi + 2P_{L0}R\right\} \tag{A.13}$$

$$\frac{\partial U}{\partial P_{L0}} = \frac{2R^2}{2EI}\left\{2M_{L0} - LR + \frac{1}{2}P_{L0}R\pi\right\} \tag{A.14}$$

From Eqs. (A.13) and (A.14), the following are obtained.

$$M_{L0}\pi - \frac{1}{2}LR\pi + 2P_{L0}R = 0 \tag{A.15}$$

$$2M_{L0} - LR + \frac{1}{2}P_{L0}R\pi = 0 \tag{A.16}$$

From Eqs. (A.15) and (A.16), $P_{L0} = 0$ and $M_{L0} = ½LR$ are obtained. Hence,

$$M_{L\theta} = \frac{1}{2}LR - \frac{1}{2}LR(1-\cos\theta) = \frac{1}{2}LR\cos\theta \tag{A.17}$$

Therefore, ε_{L0} is obtained as

$$\varepsilon_{L0} = \frac{M_{L\theta}}{EI}\eta = \frac{\eta LR}{2EI}\cos\theta \tag{A.18}$$

From Eq. (A.18), the azimuthal location where $\varepsilon_{L0} = 0$ is always satisfied is $\theta_{L0} = \pi/2 = 90°$.

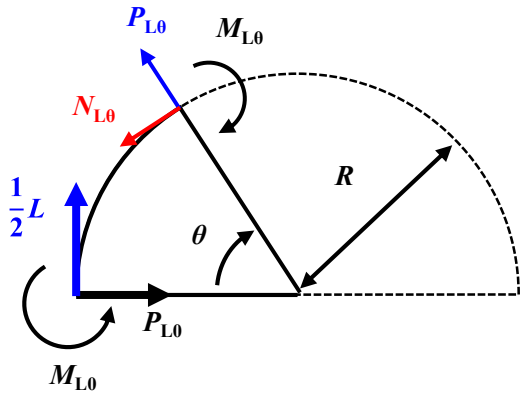

Figure A.4 Exerted force when L is applied.

A.3 Strain Due to the Pitching Moment

When M_P is applied to the ring, P_{M0} and N_{M0} occur at point B, as shown in Fig. A.5. From the assumption of an infinitesimally thin ring, the strain caused by the tangential force $N_{M\theta}$ can be ignored. $P_{M\theta}$ is ignored because the direction is perpendicular to the strain of interest. $M_{M\theta}$ at position θ is written as follows.

$$M_{M\theta} = M_{M0} - N_{M0}R(1-\cos\theta) + P_{M0}R\sin\theta \tag{A.19}$$

dU stored in ds is written as follows.

$$dU = \frac{M_{M\theta}^2}{2EI}ds = \frac{1}{2EI}\left(M_{M0} - N_{M0}R(1-\cos\theta) + P_{M0}R\sin\theta\right)^2 ds \tag{A.20}$$

Using the relation $ds = Rd\theta$, U is written as follows.

$$U = \int_0^{\pi}\frac{1}{2EI}\left(M_{M0} - N_{M0}R(1-\cos\theta) + P_{M0}R\sin\theta\right)^2 Rd\theta \tag{A.21}$$

Here, U, P_{M0}, and N_{M0} must satisfy the theorem of least work; therefore, $\partial U/\partial N_{M0} = 0$ and $\partial M/\partial P_{M0} = 0$.

$$\frac{\partial U}{\partial N_{M0}} = \frac{2R^2}{2EI}\left\{-M_{M0}\pi + \frac{3}{2}N_{M0}R\pi - 2P_{M0}R\right\} \tag{A.22}$$

$$\frac{\partial U}{\partial P_{M0}} = \frac{2R^2}{2EI}\left\{2M_{M0} - 2N_{M0}R + \frac{1}{2}P_{M0}R\pi\right\} \tag{A.23}$$

From Eqs. (A.22) and (A.23), the following are obtained.

$$-M_{M0}\pi + \frac{3}{2}N_{M0}R\pi - 2P_{M0}R = 0 \tag{A.24}$$

$$2M_{M0} - 2N_{M0}R + \frac{1}{2}P_{M0}R\pi = 0 \tag{A.25}$$

From Eqs. (A.24) and (A.25), P_{M0} and N_{M0} are obtained as follows.

$$N_{M0} = (2\pi^2 - 16)M_{M0}/(3\pi^2 - 16)R \tag{A.26}$$

$$P_{M0} = -4\pi M_{M0}/(3\pi^2 - 16)R \tag{A.27}$$

Hence,

$$\begin{aligned} M_{\mathrm{M}\theta} &= M_{\mathrm{M0}} - N_{\mathrm{M0}} R(1-\cos\theta) + P_{\mathrm{M0}} R\sin\theta \\ &= \frac{M_{\mathrm{M0}}}{3\pi^2 - 16}(\pi^2 + (2\pi^2 - 16)\cos\theta - 4\pi\sin\theta) \end{aligned} \tag{A.28}$$

Therefore, $\varepsilon_{\mathrm{M0}}$ is obtained as

$$\varepsilon_{\mathrm{M0}} = \frac{M_{\mathrm{M}\theta}}{EI}\eta = \frac{\eta M_{\mathrm{M0}}}{2EI}\frac{\pi^2 + (2\pi^2 - 16)\cos\theta - 4\pi\sin\theta}{3\pi^2 - 16} \tag{A.29}$$

From Eq. (A.29), the azimuthal location θ where $\varepsilon_{\mathrm{M0}} = 0$ is always satisfied does not exist.

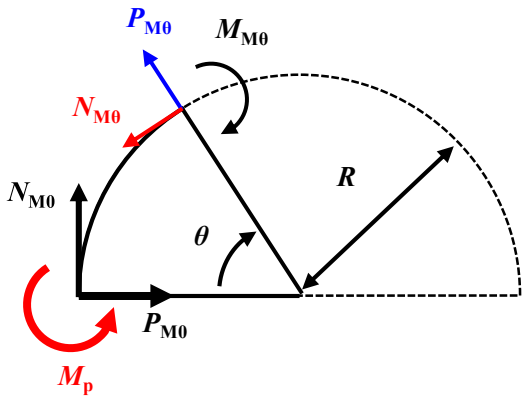

Figure A.5 Exerted force when M_{p} is applied.

A.4 Strain Distribution Due to Lift and Drag

The distribution of the strain due to L and D along the ring is written by the summation of Eqs. (A.9) and (A.18). Using $C = \eta R/2EI$,

$$\begin{aligned}\varepsilon_0 &= \varepsilon_{D0} + \varepsilon_{L0} \\ &= \frac{\eta DR}{2EI}\left(\sin\theta - \frac{2}{\pi}\right) + \frac{\eta LR}{2EI}\cos\theta \\ &= C\left\{D\left(\sin\theta - \frac{2}{\pi}\right) + L\cos\theta\right\}\end{aligned} \tag{A.30}$$

and C, E, I, R, and η depend on the characteristics of the balance. The dependence of ε_0 on θ is shown in Fig. A.6.

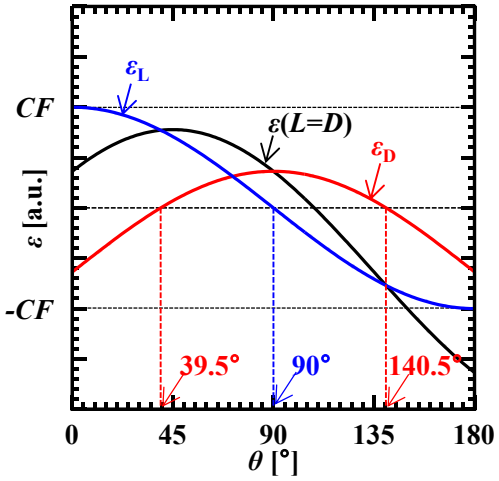

Figure A.6 Angular strain distribution along an infinitesimally thin ring.